DEEP ULTRAVIOLET PHOTOLUMINESCENCE STUDIES OF Al-RICH AlGaN AND AlN
EPILAYERS AND NANOSTRUCTURES

by

NEERAJ NEPAL

B.Sc., Tribhuvan University, Kathmandu, Nepal, 1994

M.Sc., Tribhuvan University, Kathmandu, Nepal, 1997

AN ABSTRACT OF A DISSERTATION

submitted in partial fulfillment of the requirements for the degree

DOCTOR OF PHILOSOPHY

Department of Physics
College of Arts and Sciences

KANSAS STATE UNIVERSITY
Manhattan, Kansas

2006

Abstract

Deep ultraviolet (UV) photoluminescence (PL) spectroscopy has been employed to study optical properties of AlGaN alloys, undoped and doped AlN epilayers and nanostructure AlN photonics crystals (PCs). Using a deep UV laser system with an excitation wave length at 197 nm, continuous wave PL, temperature dependent, and time-resolved PL have been carried out on these AlGaN and AlN epilayers and nanostructures.

We have measured the compositional and temperature dependence of the energy bandgap of $Al_xGa_{1-x}N$ alloys covering the entire alloy range of x, $0 \leq x \leq 1$ and fitted with the Varshni equation. Varshni coefficients, α and β, in AlGaN alloys have a parabolic dependence with alloy concentration x. Based on the experimental data, an empirical relation was thus obtained for the energy gap of AlGaN alloys for the entire alloy concentration and at any temperature below 800 K.

The exciton localization energy in $Al_xGa_{1-x}N$ alloys the entire composition range ($0 \leq x \leq 1$) has been measured by fitting the band edge emission peak energy with the Varshni equation. Deviations of the excitonic emission peak energy from the Varshni equation at low temperatures provide directly the exciton localization energies, E_{Loc} in AlGaN alloys. It was found that E_{Loc} increases with x for $x \leq 0.7$, and decreases with x for $x \geq 0.8$. The relations between the exciton localization energy, the activation energy, and the emission linewidth have been established. It thus provides three different and independent methods to determine the exciton localization energies in AlGaN alloys.

Impurity transitions in AlGaN alloys have also been investigated. Continuous wave (CW) PL spectra of Si and undoped AlGaN alloys reveals groups of impurity transitions that

have been assigned to the recombination between shallow donors and an isolated triply charged cation-vacancy $(V_{III})^{3-}$, a doubly charged cation-vacancy-complex $(V_{III}\text{-complex})^{2-}$, and a singly charged cation-vacancy-complex $(V_{III}\text{-complex})^{-1}$. The energy levels of these deep acceptors in $Al_xGa_{1-x}N$ ($0 \leq x \leq 1$) alloys are pinned to a common energy level in the vacuum. AlGaN alloys predominantly exhibiting the bandedge and $(V_{III}\text{-complex})^{1-}$ transitions possess improved conductivities over those emitting predominantly $(V_{III})^{3-}$ and $(V_{III}\text{-complex})^{2-}$ related transitions. These results thus answer the very basic question of high resistivity in Al-rich AlGaN alloys.

Acceptor doped AlGaN alloys have been studied by deep UV PL. A PL emission line at 6.02 eV has been observed at 10 K in Mg-doped AlN. It is due to the recombination of an exciton bound to the neutral Mg acceptor (I_1) with a binding energy, E_{bx} of 40 meV, which indicates large activation energy of the Mg acceptor. The observed large binding energy of the acceptor-bound exciton is consistent with relatively large binding energy of the Mg acceptor in AlN.

With the energy level of 0.51 eV for Mg dopants in AlN, it is interesting and important to study other suitable acceptor dopants for AlN. Growth and optical studies of Zn-doped AlN epilayers has been carried out. The PL spectra of Zn-doped AlN epilayers exhibited two impurity emission lines at 5.40 and 4.50 eV, which were absent in undoped epilayers. They are assigned respectively, to the transitions of free electrons and electrons bound to triply positively charged nitrogen vacancies (0.90 eV deep) to the Zn^0 acceptors. It was deduced that the Zn energy level is about 0.74 eV above the valence band edge, which is about 0.23 eV deeper than the Mg energy level in AlN.

Nitrogen vacancies are the compensating defects in acceptor doped AlGaN alloys. A nitrogen vacancy (V_N) related emission line was also observed in ion-implanted AlN at 5.87 eV

and the energy level of singly charged V_N^{1+} is found at 260 meV below the conduction band. As a consequence of large binding energy of V_N^{1+} as well as high formation energy, V_N^{1+} in AlN cannot contribute significant n-type conductivity, which is consistent with experimental observation.

The temperature dependent PL study of the bandedge emissions in GaN and AlN epilayers up to 800 K has been carried out, which reveals two distinctive activation processes. The first process occurring below $T_t = 325$ K ($T_t = 500$ K) for GaN (AlN) is due to the activation of free excitons to free carriers, whereas the second occurring above T_t with an activation energy of 0.29 eV (0.3 eV) for GaN (AlN) is believed to be associated with a higher lying conduction band (Γ_3) at about 0.3 eV above the conduction band minimum (Γ_1). These higher lying bands could affect device performance of GaN and AlN at elevated temperatures.

Two-dimensional nanostructured AlN photonic crystals (PCs) with a varying periodicity/diameter down to 150 nm/75 nm have also been studied by deep UV PL. With PCs formation, a 20-fold enhancement in the band edge emission intensity at 208 nm over unpatterned AlN epilayer has been observed. The emission intensity increases with the decrease in the lattice constant of the AlN PCs. AlN PCs represent photonic crystals with highest (shortest) bandgap (wavelength) semiconductors, which open up new opportunities for exploring novel physical phenomena in the artificially structured photonic band gap material systems and their applications, particularly in the area of deep UV as well as nano-photonics.

DEEP ULTRAVIOLET PHOTOLUMINESCENCE STUDIES OF Al-RICH AlGaN AND AlN EPILAYERS AND NANOSTRUCTURES

by

NEERAJ NEPAL

B.Sc., Tribhuvan University, Kathmandu, Nepal, 1994

M.Sc., Tribhuvan University, Kathmandu, Nepal, 1997

A DISSERTATION

submitted in partial fulfillment of the requirements for the degree

DOCTOR OF PHILOSOPHY

Department of Physics
College of Arts and Sciences

KANSAS STATE UNIVERSITY
Manhattan, Kansas

2006

Approved by:

Major Professor
Hongxing Jiang

Abstract

Deep ultraviolet (UV) photoluminescence (PL) spectroscopy has been employed to study optical properties of AlGaN alloys, undoped and doped AlN epilayers and nanostructure AlN photonics crystals (PCs). Using a deep UV laser system with an excitation wave length at 197 nm, continuous wave PL, temperature dependent, and time-resolved PL have been carried out on these AlGaN and AlN epilayers and nanostructures.

We have measured the compositional and temperature dependence of the energy bandgap of $Al_xGa_{1-x}N$ alloys covering the entire alloy range of x, $0 \leq x \leq 1$ and fitted with the Varshni equation. Varshni coefficients, α and β, in AlGaN alloys have a parabolic dependence with alloy concentration x. Based on the experimental data, an empirical relation was thus obtained for the energy gap of AlGaN alloys for the entire alloy concentration and at any temperature below 800 K.

The exciton localization energy in $Al_xGa_{1-x}N$ alloys the entire composition range ($0 \leq x \leq 1$) has been measured by fitting the band edge emission peak energy with the Varshni equation. Deviations of the excitonic emission peak energy from the Varshni equation at low temperatures provide directly the exciton localization energies, E_{Loc} in AlGaN alloys. It was found that E_{Loc} increases with x for $x \leq 0.7$, and decreases with x for $x \geq 0.8$. The relations between the exciton localization energy, the activation energy, and the emission linewidth have been established. It thus provides three different and independent methods to determine the exciton localization energies in AlGaN alloys.

Impurity transitions in AlGaN alloys have also been investigated. Continuous wave (CW) PL spectra of Si and undoped AlGaN alloys reveals groups of impurity transitions that

have been assigned to the recombination between shallow donors and an isolated triply charged cation-vacancy $(V_{III})^{3-}$, a doubly charged cation-vacancy-complex $(V_{III}\text{-complex})^{2-}$, and a singly charged cation-vacancy-complex $(V_{III}\text{-complex})^{-1}$. The energy levels of these deep acceptors in $Al_xGa_{1-x}N$ ($0 \leq x \leq 1$) alloys are pinned to a common energy level in the vacuum. AlGaN alloys predominantly exhibiting the bandedge and $(V_{III}\text{-complex})^{1-}$ transitions possess improved conductivities over those emitting predominantly $(V_{III})^{3-}$ and $(V_{III}\text{-complex})^{2-}$ related transitions. These results thus answer the very basic question of high resistivity in Al-rich AlGaN alloys.

Acceptor doped AlGaN alloys have been studied by deep UV PL. A PL emission line at 6.02 eV has been observed at 10 K in Mg-doped AlN. It is due to the recombination of an exciton bound to the neutral Mg acceptor (I_1) with a binding energy, E_{bx} of 40 meV, which indicates large activation energy of the Mg acceptor. The observed large binding energy of the acceptor-bound exciton is consistent with relatively large binding energy of the Mg acceptor in AlN.

With the energy level of 0.51 eV for Mg dopants in AlN, it is interesting and important to study other suitable acceptor dopants for AlN. Growth and optical studies of Zn-doped AlN epilayers has been carried out. The PL spectra of Zn-doped AlN epilayers exhibited two impurity emission lines at 5.40 and 4.50 eV, which were absent in undoped epilayers. They are assigned respectively, to the transitions of free electrons and electrons bound to triply positively charged nitrogen vacancies (0.90 eV deep) to the Zn^0 acceptors. It was deduced that the Zn energy level is about 0.74 eV above the valence band edge, which is about 0.23 eV deeper than the Mg energy level in AlN.

Nitrogen vacancies are the compensating defects in acceptor doped AlGaN alloys. A nitrogen vacancy (V_N) related emission line was also observed in ion-implanted AlN at 5.87 eV

and the energy level of singly charged V_N^{1+} is found at 260 meV below the conduction band. As a consequence of large binding energy of V_N^{1+} as well as high formation energy, V_N^{1+} in AlN cannot contribute significant n-type conductivity, which is consistent with experimental observation.

The temperature dependent PL study of the bandedge emissions in GaN and AlN epilayers up to 800 K has been carried out, which reveals two distinctive activation processes. The first process occurring below $T_t = 325$ K ($T_t = 500$ K) for GaN (AlN) is due to the activation of free excitons to free carriers, whereas the second occurring above T_t with an activation energy of 0.29 eV (0.3 eV) for GaN (AlN) is believed to be associated with a higher lying conduction band (Γ_3) at about 0.3 eV above the conduction band minimum (Γ_1). These higher lying bands could affect device performance of GaN and AlN at elevated temperatures.

Two-dimensional nanostructured AlN photonic crystals (PCs) with a varying periodicity/diameter down to 150 nm/75 nm have also been studied by deep UV PL. With PCs formation, a 20-fold enhancement in the band edge emission intensity at 208 nm over unpatterned AlN epilayer has been observed. The emission intensity increases with the decrease in the lattice constant of the AlN PCs. AlN PCs represent photonic crystals with highest (shortest) bandgap (wavelength) semiconductors, which open up new opportunities for exploring novel physical phenomena in the artificially structured photonic band gap material systems and their applications, particularly in the area of deep UV as well as nano-photonics.

Table of Contents

List of Figures

AlN epilayers measured at 10 K.

List of Table

Acknowledgments

Dedication

To

Ama and Kabi

CHAPTER 1 Introduction

Wurtzite structured, III-nitrides (InN, GaN and AlN) have direct bandgaps of 0.7 eV for InN, 3.4 eV for GaN and 6.1 eV for AlN. They have been recognized as important semiconductors for optoelectronic device applications in the wide spectral range from infrared (IR) (1800 nm) down to deep ultraviolet (UV) (200 nm). They have strong chemical bonds which make them very stable and resistant to degradation under conditions of harsh environments like high electric currents, high temperature, and intense light illumination. The strong chemical bonds also account for the difficulty in introducing dislocations once the material is grown, which removes one of the main mechanisms of degradation in other III-V semiconductors. GaN and AlN have wide direct bandgap, which makes them suitable for visible, UV and deep UV light sources/sensors and for high-power/high-temperature electronic devices [1-4]. They have high mechanical hardness, high thermal conductivity, and large dielectric constants.

Synthesis of AlN was reported in 1907 [5], and is believed to be one of the first III-nitride semiconductors ever synthesized. The growth of GaN crystalline film was started since 1969 [6]. Pankove et al. fabricated metal-insulator-semiconductor (MIS) light emitting diode (LED) on GaN in 1971 [7]. In the same year, Manasevit et al. grew GaN by metalorganic chemical vapor deposition (MOCVD) for the first time, which is the most common method used in these days for the growth of III-nitrides [8]. A high quality GaN epilayer was grown on sapphire by using a low temperature AlN buffer layer [9]. Due to strong chemical bonding, high growth temperature is necessary for III-nitrides, which limits the choice of substrates to those that are stable at elevated temperatures. Most of the film growth was carried out on sapphire or silicon carbide (SiC) due to the lack of the native substrates. Although a large difference in lattice parameters

and in linear thermal expansion can result in poor-quality epitaxial films, there have been advances on the growth of III-nitrides on these substrates.

As grown GaN is n-type, and the free electron concentration can be controlled by Si doping. However, attaining p-type GaN was difficult for a long time. Hydrogen passivation, nitrogen vacancies, or other unknown defects made it difficult to obtain high-quality *p*-type material. The first p-type conduction in GaN with Mg doping was achieved by Amano et al. [10]. Nakamura et al. reported p-type GaN with superior hole concentration by post growth thermal annealing [11]. Since then, numbers of reviews and books concerning recent advances in growth, characterization and device application of III-nitrides have been published [12-15].

There has been much progress on blue, green [4] and UV LEDs down to 280 nm [15], even though the technology of the III-nitride materials system in the deep UV and green to red region is still relatively immature. Recent demonstration of an AlN based LED with a PIN (p-type intrinsic/n-type) and MIS (metal-insulator-semiconductor) structure at an emission wavelength of 210 nm has shown promising potential for the application in the UV C-band spectral range [16]. AlN also has applications in stable x-ray production, surface acoustic wave (SAW) devices, and cold cathode applications due to its high thermal conductivity, large piezoelectric field, and low electron affinity [17-19].

For application of AlN as an active material, highly conductive n-type and p-type AlN materials are desirable. However, it is very difficult to improve the conductivity of AlN due to the large activation energy of dopants, and the simultaneous generation of compensating centers and defects during the crystal growth. While n-type AlN epilayers with reasonable conductivities have been achieved with Si-doping [20-23], p-type conductivity is extremely difficult to obtain due to the large activation energy of Mg acceptors. The activation energy of

Mg is about 160 meV in GaN, which increases with Al content up to 0.51 eV in AlN [24-27]. Enhancing the p-type conductivity of Al-rich AlGaN alloys is challenging due to the large activation energy of acceptor dopant.

1.1 Overview of Al-rich AlGaN alloys

AlGaN alloys have the capability of tuning the direct band gap over a large energy range, from around 3.4 to 6.1 eV, which makes them very useful for ultraviolet (UV) and deep UV optoelectronic device applications. Due to absorption by the ozone layer in the atmosphere, UV C-band (< 280 nm) spectrum from the solar system is absent on the earth. AlGaN alloy has the adjustable cutoff wavelength by varying Al content so the visible-blind and solar-blind UV detectors can be formed without the use of extra filters. Biological agents have not developed an immunity to overcome the UV C-band irradiation effect. Thus, a compact light source in this range will have application in biological agent sterilization. Because of its large direct bandgap, Al-rich AlGaN alloys can be used in the development of optoelectronic devices operating down to 200 nm. The recent rapid progress in the field of Al-rich AlGaN alloys has allowed the fundamental optical properties and parameters of these materials to be measured and their optical process to be studied.

One of the important properties, which affects the optical and electrical properties of AlGaN alloy, is the carrier and exciton localization. Exciton localization energy and PL emission linewidth yield the information about compositional and potential fluctuations occurring in semiconductor alloys. Fundamental optical properties such as optical transitions, carrier dynamic processes, and carrier-phonon interactions predominantly determine the device performance. Therefore, understanding fundamental optical properties is crucial for the development of suitable material qualities and device structures. However, in the past, the growth of Al-rich

AlGaN alloys suffered from poor crystalline quality and it was therefore difficult to dope with an n- (Si) or p-type (Mg) dopant. Device quality p-type Al-rich AlGaN alloys with high quantum efficiencies remains one of the foremost challenges for the nitride community.

Due to the resistive nature of Al-rich AlGaN alloys, PL is one of the most important probes to characterize them. Experimental setup for optical studies is complicated compared to other III-V semiconductors due to large bandgap of Al-rich AlGaN alloys. Time-resolved PL system with excitation wavelengths below 200 nm is required to study optical properties of $Al_xGa_{1-x}N$ alloys in the whole range of x. We have developed a deep UV time-resolved PL system, which consists of a frequency quadrupled 100 femtosecond Ti:sapphire laser with an average power of 3 mW, and with an excitation photon energy set at 6.28 eV (repetition rate of 76 MHz), and a streak camera with time resolution of about 2 ps [28].

It was found that the material quality of AlGaN alloys strongly correlates with the intensity of the impurity transition due to native defects. Therefore, the understanding of native defects in AlGaN alloys is very important for improving the material quality and device performance. Calculations have indicated that the cation vacancies and its complexes in undoped and Si-doped AlGaN alloys (particularly in Al-rich alloys), and anion vacancies in p-type doped AlGaN alloys have small formation energies, and thus are easily formed during the crystal growth [29-32]. These (V_{III}^{3-}) and $(V_{III}\text{-complex})^{2-}$ are the deep impurities in AlGaN alloys separated by 0.5 eV and are pined to a common energy level in the vacuum [33].

1.2 Band structure of AlGaN alloys

Although the band structure of III-nitrides in the wurtzite structure is quite similar to that of direct band gap zincblende semiconductors such as GaAs, nitrides have no inversion symmetry along and perpendicular to the direction of the c-axis. The valance band degeneracy is

lifted by the crystal field interaction, and the strain has a less dramatic effect on the valance band dispersion than that in GaAs. Also, the valance band is highly non parabolic. This anisotropy results in various phenomena like the presence of a spontaneous electric polarization, the splitting of the valence bands, and polarized spontaneous emission. Among the III-nitride family, GaN has been well studied theoretically and experimentally. Its key parameters which describe the band structure near the Γ point, including the value of the valance band splitting and the effective hole masses are known. But there is a difference in the valance band dispersion between GaN and AlN [34]. The band structure of GaN near the Γ point is shown in Fig. 1.1 [35]. The order of the A-, B-, and C- valance bands are Γ_9, Γ_7, and Γ_7, respectively. For the splitting between the A and C valance band maxima (E_{AC}), values of 28 meV, [36] 24 meV [37], 43 meV [35] have been published, while the value of E_{AB} is about 6 meV. The crystal field splitting in wurtize (WZ) GaN is positive (+38 meV) and the dominant emission is $\mathbf{E}\_\mathbf{|}\_\mathbf{c}$, while in WZ AlN it is negative (-219 meV) [38]. Due to the negative crystal-field splitting, the order of the valance band in AlN is Γ_7, Γ_9, and Γ_7, respectively, and the dominant emission is $\mathbf{E}//\mathbf{c}$. Band structure of WZ AlN near the Γ point is shown in Fig. 1.2 [38]. When Al content is increased from 0 to 1 in $Al_xGa_{1-x}N$ alloys, crystal-field splitting decreases from +38 to -238 meV as shown in Fig.1.3 [39] and the split-off band moves up to be the top most valance band. Therefore, in Al-rich AlGaN alloys grown on c-plane sapphire, light emission is polarized in $\mathbf{E}//c$ (TM mode).

The structure of AlGaN alloys is based on sp3 hybridization and the lowest conduction band at the Γ (k = 0) point is due to antibonding s-orbitals. Therefore, the conduction band edge at the surface is in principle, expected to lie above the vacuum level causing negative electron affinity, which makes these materials useful for photodetectors and as electron sources in a

variety of applications including displays [40-44]. AlGaN based photo-detectors can operate down to the x-ray region [43].
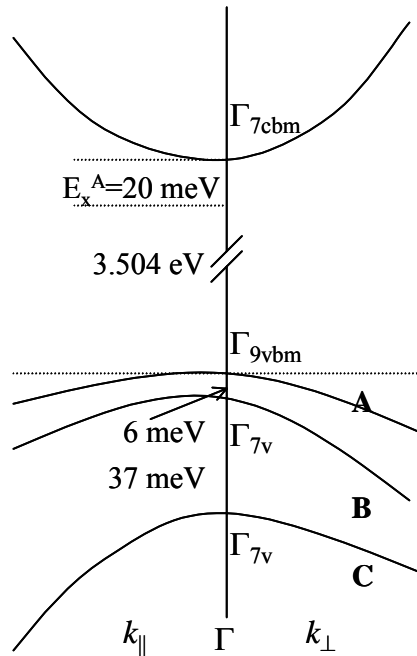
Fig. 1.1 Band structure of WZ GaN near the Γ point (Figure from Ref. 35).
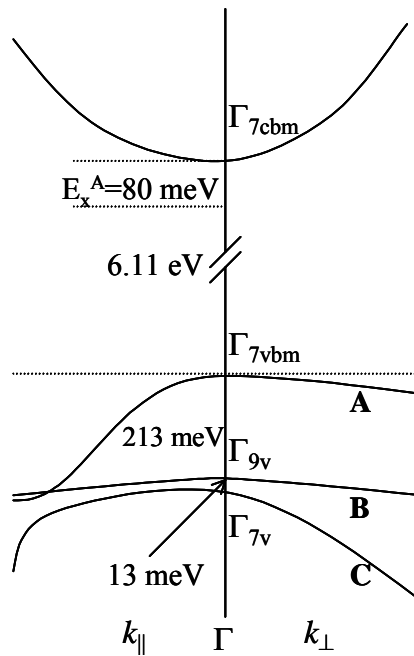
Fig. 1.2 Band structure of WZ AlN near the Γ point (Figure from Ref. 38).
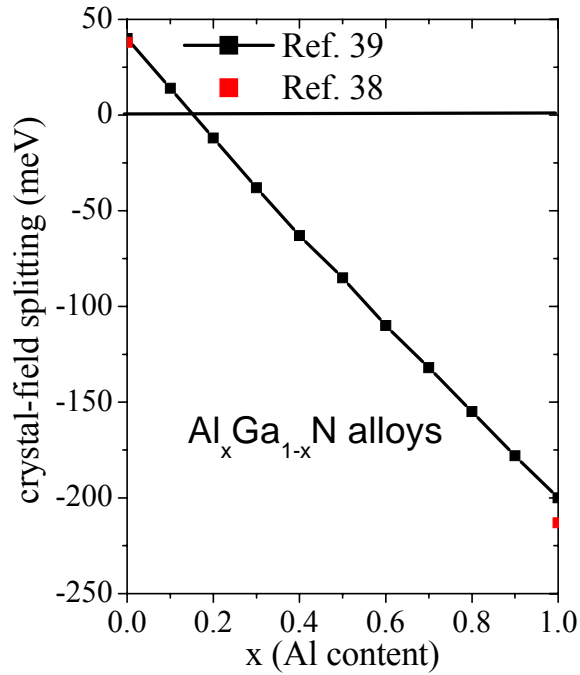
Fig. 1.3 Crystal-field splitting as a function of x for AlGaN alloys (Figures from Refs. 38 and 39).

1.3 Laser-semiconductor interaction

In semiconductors, electrons are delocalized. Atoms are bound together by covalent bonds in which atoms share an electron pair, resulting in the splitting of atomic levels into bonding and anti-bonding states. The delocalized interaction of atoms through a periodic potential broadens the bonding and anti-bonding states to form bonding (valence) and anti-bonding (conduction) energy bands. Electrons occupy different states in the bands; the one in the bonding states, or valence bands, are the bound electrons. On the other hand, electrons in the anti-bonding state or conduction band behave like free charges. The dielectric function of a semiconductor is therefore determined by the band structure, which describes the relationship of energy vs. wave vector of the states.
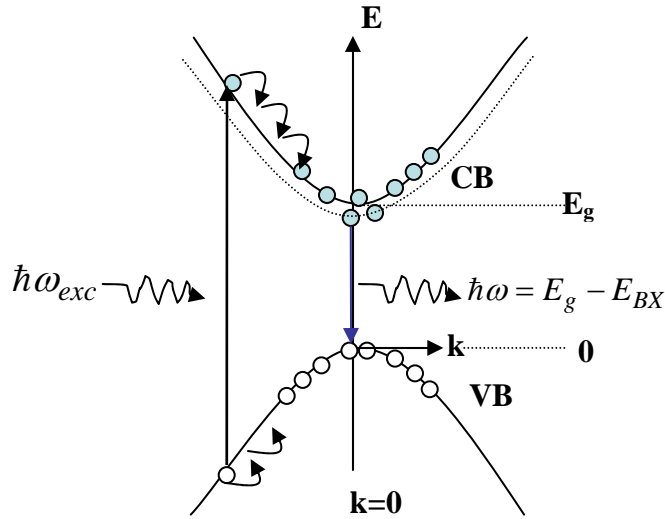
Fig. 1.4 Exciton formation and recombination in simple band structure.

When photons interact with carriers they transfer energy to the electrons and holes as shown in Fig. 1.4. During the optical excitation process energy and momentum are conserved. Since the wavelength of light is much larger than the lattice constant, that is the momentum of the photon is much smaller than that of a typical electron:

$$q = 2\pi/\lambda << k = 2\pi/a \qquad (1.1)$$

Electrons absorb photons resulting vertical transition from the valence band to the conduction band leaveing holes behind in the valence. For the conservation of energy we have,

$$E_c - E_v = \hbar\omega \qquad (1.2)$$

where E_c and E_v are the energies of the free electron and hole, respectively. For indirect bandgap semiconductors the conduction band minimum and valence band maximum does not occur at the same point in k-space and bandedge transition requires absorption or emission of a phonon or an

8

impurity scattering. The required momentum change for indirect transition is provided by phonon or impurity and the radiative transition probability amplitudes are much smaller due to three-particle interaction.

The photon absorption and excitation process take place in the Γ-valley. Due to limited number of density of states, the phase space cannot hold all the excited carriers. The total number of density of states available at the Γ-valley can be estimated assuming spherical conduction bands. The molecular density of the bulk semiconductor at room temperature is given by

$$N_{mol} = \frac{\rho}{m_{mol}} N_A \qquad (1.3)$$

$$N_{mol}(\text{GaN}) = 4.4 \times 10^{22} \text{ cm}^{-3}, N_{mol}(\text{AlN}) = 4.8 \times 10^{22} \text{ cm}^{-3}$$

where ρ is the density of semiconductor at room temperature, m_{mol} is the molecular weight, and N_A is Avogadro's number. The bonding states form the valence bands Γ_{7a}, Γ_{7b}, and Γ_9 each with 2-fold degeneracy, in GaN. Similarly, the anti-bonding states give rise to the conduction bands. Therefore, valence bands in the first Brillouin Zone (BZ) contain 6 x 4.4x 10^{22} cm^{-3} and 6 x 4.8x10^{22} cm^{-3} number of states in GaN and AlN, respectively.

The generation of electron-hole pairs due to single photon absorption is the most common interaction process in semiconductors. The other interaction processes in semiconductors are (a) single photon absorption, (b) two-photon absorption, (c) free carrier absorption, and (d) impact ionization. As soon as the free carriers are created relaxation starts. The relaxation processes in semiconductors are (a) carrier-carrier scattering, (b) carrier phonon scattering, (c) radiative recombination, (d) Auger recombination, and (d) carrier diffusion.

Generally, carrier-carrier scattering, carrier phonon scattering, intravalley, and inter-valley scattering take place on the order of femtosecond time scale.

Free electrons and holes can recombine radiatively or non-radiatively. In a radiative recombination process, an electron and a hole of identical wave vector recombine emitting the energy difference in the form of a photon. Thus, the radiative recombination rate is proportional to the product of the electron and hole density (n^2). These processes which lower both the free carrier energy and the free carrier density, takes place on the nano- and pico-second time scale. In our PL study, we utilize radiative recombination process in direct bandgap semiconductors.

1.4 Recombination dynamics in semiconductors

1.4.1 Free exciton recombination

In pure semiconductor materials, the photoexcited electrons and holes pair off into free excitons (FX) by Coulomb interaction, which can recombine by emitting photons. In direct bandgap semiconductors, momentum is conserved by a simple radiative transition and the energy of the emitted photon by free exciton recombination is given by,

$$\hbar\omega = E_g - E_{FX} \qquad (1.4)$$

where E_{FX} is the binding energy of free exciton. Figure 1.5 shows free and bound excitons insemiconductors.
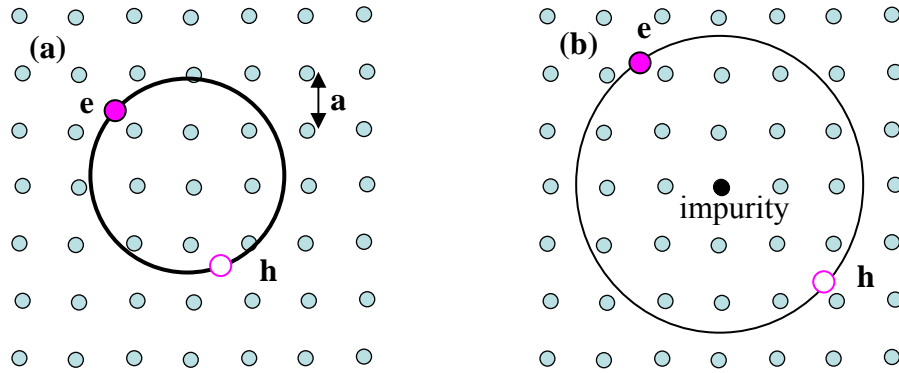
Fig. 1.5 (a) Free exciton (b) bound exciton in semiconductors.

1.4.2 Bound exciton recombination

In the presence of impurities, bound excitons may be obtained. These bound excitons have smaller kinetic energy and when they recombine; their emission is characterized by a spectral line at lower energy than that of free excitons. Emitted photon by bound exciton recombination is given by,

$$\hbar\omega = E_g - E_{FX} - E_{BX} \qquad (1.5)$$

where E_{BX} is the binding energy of the bound exciton. Exciton can be bound to neutral (ionized) donor and the corresponding PL emission line is called D^0X (D^+X) or I_2 (I_3) transition. If it is bound to neutral acceptor, the PL emission line is called A^0X or I_1 transition. As temperature increases, bound excitons dissociate into neutral impurities and free excitons.

1.4.3 Band-to-impurity transition

Band-to-impurity transition could be shallow transitions or deep transitions. The shallow transitions of neutral/ionized donors or acceptors could be radiative in the far infrared region. By deep transition, we shall mean either the transition of an electron from the conduction band to an acceptor level or a transition from the donor level to the valance band. Such a transition emits a photon, $\hbar\omega = E_g - E_i$ where E_i is the energy of donor or acceptor, for the direct transition, and $\hbar\omega = E_g - E_i - E_p$, if the transition is indirect and involves a phonon of energy E_p.

1.4.4 Band-to-band recombination

Free electrons in the conduction band can recombine directly with free holes in the valance band. Such a transition is called a band-to-band transition, and gives the fundamental band gap of the material. Band-to-band recombination emission lines redshift with increasing excitation intensity due to the effect of band gap renormalization.

1.4.5 Donor-acceptor pair recombination

Recombination of electrons in the donor level to holes in the acceptor level is called a donor-to-acceptor pair (DAP) transition. After DAP recombination, we have D^+ and A^- and the Coulomb interaction between donor and acceptor modifies the binding energies such that the energy separating the paired donor and acceptor states is

$$\hbar\omega = E_g - E_A - E_D + \frac{q^2}{\varepsilon r} \qquad (1.6)$$

where E_A and E_D are donor and acceptor level energies, ε is the dielectric constant, q is the charge, and r is the distance between donor and acceptor.

1.5 Growth of AlGaN alloys

There are different growth techniques used for synthesis of III-nitride epilayers. Among them, the metalorganics chemical vapor deposition (MOCVD) technique had become the mature process for the growth of III–nitrides by the mid 1990s. The development of molecular beam epitaxy (MBE) growth technique for the nitrides has been slow because of the low growth temperatures. Ammonia (NH_3), a common source of nitrogen (N), is stable at low temperatures. We have used MOCVD growth technique to grow AlGaN alloys. The source materials generally used are trimethylgallium (TMGa) for Ga, trimethylaluminum (TMAl) for Al, and trimethylindium (TMIn) for In. NH_3 is used as source material for N. Mg is widely used as a *p*-type dopant, and Si as an *n*-type dopant. Biscyclopentadienyl (Cp_2Mg) is used as a source of Mg, and silane (SiH_4) as a source of Si.

Several attempts were made to synthesize GaN crystals during the period 1930–1960 but good quality crystals of reasonable size could not be grown. Growth of GaN epitaxial layers using hydride vapor phase epitaxy (HVPE) were reported in the late 1960s [6,9]. AlN, on the other hand was grown by a sublimation method [5]. Many attempts to grow thick layers using these methods were made during the 1970s. Recently, rapid progress of AlN growth has been achieved. Single crystal bulk AlN is not available commercially. AlGaN alloys with different band gaps can be achieved by alloying with GaN. We can tune the band gap of AlGaN alloys from 3.4 to 6.1 eV. Figure 1.6 shows the variation of the band gap energy of InN, GaN and AlN with the "a" lattice constant. The lattice mismatch of GaN and AlN with the commonly used sapphire substrate is 16 and 13 % respectively.
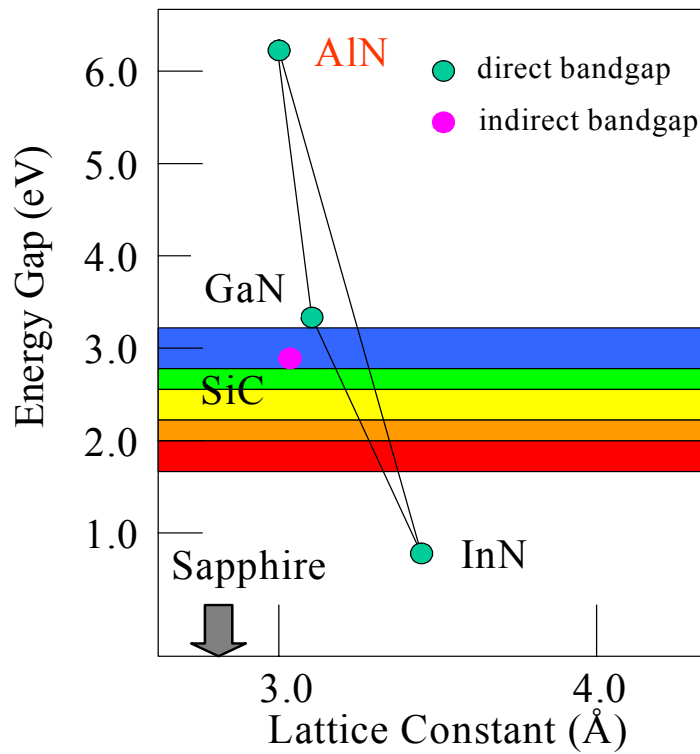
Fig. 1.6. Variation of band gap with lattice constant in wurtize III-nitrides.

1.6 Overview of the thesis

This dissertation has been divided into 4 chapters. After a brief introduction in chapter 1, experimental setups, particularly deep UV time-resolved PL setups (down to 197 nm), are discussed in chapter 2. Experimental results are presented and discussed in chapter 3. The dissertation ends with a general conclusion in chapter 4.

CHAPTER 2 Experimental Setup

2.1 Deep UV time-resolved photoluminescence setup

One of the lasers in our laboratory is a frequency doubled cavity dumped dye laser pumped with frequency doubled Nd:YAG laser (Coherent Antares 76). It has an output power of 20 mW at 290 nm. It has been used as a fundamental laser source in our laboratory. This laser system was used to study the optical properties of $Al_xGa_{1-x}N$ alloys for $x < 0.4$. However, it cannot be used for Al rich $Al_xGa_{1-x}N$ alloys ($x > 0.4$). Therefore a deep UV time-resolved PL setup is very important to characterize and study the fundamental properties of Al-rich AlGaN alloys. In this thesis, a specially designed deep UV laser spectroscopy system was utilized for PL measurements. This system basically consists of a frequency quadrupled Ti:sapphire laser and a streak camera, providing an excitation power of about 3 mW at 197 nm with a time-resolution of 2 ps and a detection wavelength range spanning from the IR (1.7 μm) to the deep UV (down to 200 nm). Samples were mounted on a high temperature stage with a cold finger in a closed-cycle helium refrigerator (Janis), and the temperature was controlled between 10 and 800 K.

Figure 2.1 shows the schematic diagram of the pico-second time-resolved PL setup used in this thesis [28].To achieve a mode locked pulse laser at 197 nm, an excitation source for the Ti:sapphire laser and a frequency quadrupler are used. Since the Ti:sapphire crystal has a maximum absorption at around 500 nm as shown in Fig 2.2, our pumping laser is a frequency doubled Nd:YAG laser from Coherent Inc., (Verdi-10) with a green output of 10 W at 532 nm. The Nd: YAG laser is designed for a continuous wave (CW) light source at a wavelength of 1064 nm with high power in transverse (TEM_{00}) mode. After frequency doubling, the output power of 10 W at 532 nm is a very suitable pumping source for the Ti:sapphire crystal.
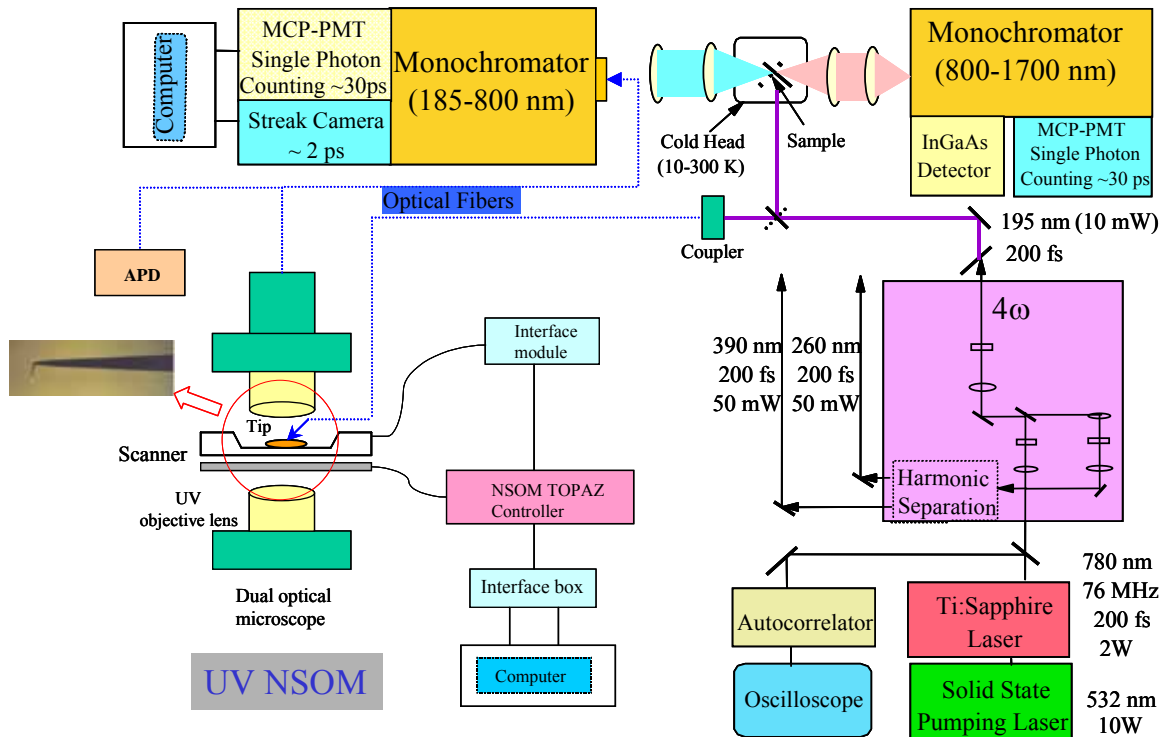
Fig. 2.1 Deep UV time-resolved PL setup integrated with NSOM.
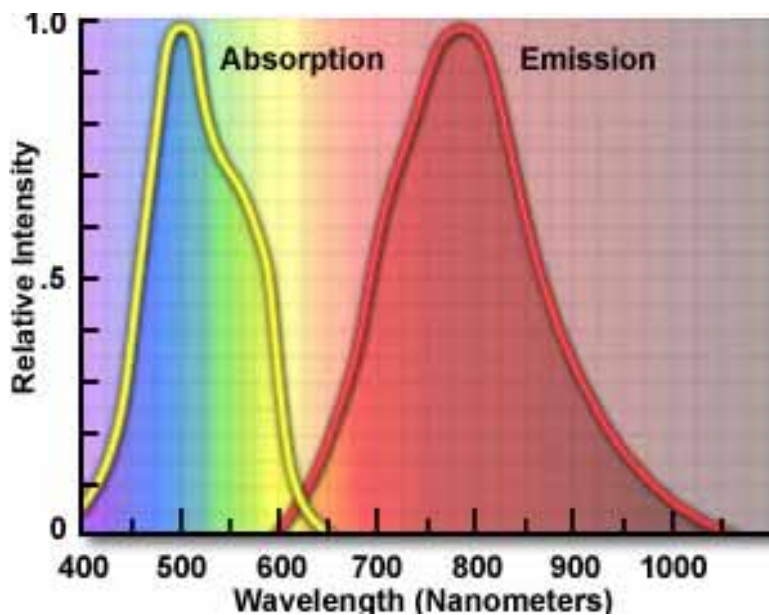
Fig. 2.2 Ti:sapphire absorption/emission spectra.
(Ref: http://www.micro.magnet.fsu.edu/primer/java/lasers/tsunami/).

2.1.1 Deep UV laser system

A picture of the Coherent Inc., (Verdi-10) is shown in Fig 2.3. It consists of a power source, two pump diode lasers (~808 nm) called FAP-I^{TM} (fiber array package integrated), which convert low-voltage high-current electrical power into tunable laser, and a laser head. The laser head has a laser resonator, gain medium, second harmonic generator, temperature servos and output optics. The Verdi-10 laser resonator is a robust unidirectional single-frequency ring cavity design employing intracavity second harmonic generator (SHG) to produce multi-watt-level CW green light (532 nm) output. The gain medium employed in Verdi -10 is Nd:YVO$_4$ (neodymium-doped yttrium orthovandate, commonly known as vandate, which has a lasing wavelength of 1064 nm. The nonlinear optical medium used for SHG in Verdi-10 is a birefringent crystal lithium triborate (LBO), which is housed within an oven that is designed to maintain a constant temperature of 150°C. Temperature is actively monitored and stabilized by servo systems.

For the Ti:sapphire laser source, we have a Coherent Mira-900F. Its picture is shown in Fig. 2.4. It is a mode-locked ultrafast laser that uses titanium doped sapphire crystal as the gain medium and is tunable from 710 to 1100 nm. It consists of a laser head and a controller. The technique used to modelock the Mira-900F laser is the Kerr lens modelocking (KLM). The optical cavity is specially designed to utilize changes in the spatial profile of the beam produced by self-focusing due to the optical Kerr effect in the Ti:sapphire crystal. This self-focusing results in a higher round trip gain in the modelocked high power versus low peak power operation, due to an increased overlap between the pumped gain profile and the circulating cavity mode. Group velocity dispersion compensation is used to produce near transformed limited pulses of less than 200 fs. Finally the output of Mira-900F is fed into a frequency quadrupler, where 2 W at 790 nm laser is converted to 3 mW at 197 nm.

Fig. 2.3 Pumping laser with 10 W green (532 nm) output power from laser head (Coherent Verdi-10).

Fig. 2.4 Ti:sapphire laser with 2W oputput (Coherent Mira 900-F).

The Quadrupler basically consists of three crystals for the SHG, third harmonic generation (THG), and fourth harmonic generation (FHG). The incident pulse of 790 nm with a 2 W power is converted to a 395 nm pulse with about 0.5 W power by LBO SHG crystal. The fundamental and second harmonic beams from different optical paths meet at the THG crystal (BBO) to produce the third harmonic laser of 263 nm with an average power of 150 mW. Finally, we mix the fundamental and THG (ω_3) beams traveling through different optical paths by using the FHG crystal. By mixing the fundamental (ω_1) and ω_3, we can achieve a frequency quadrupled 100 femtosecond pulse with an output wavelength of 197 nm (6.28 eV), repetition rate of 76 MHz and an average power of 3 mW. The efficiency of the FHG depends on the interaction length in the crystal and the phase-matching conditions.

Besides the Ti-sapphire laser, we also have a dye laser. The cavity-dumped dye laser is pumped by the Antares Nd:YAG laser at a wavelength of 532 nm with an average power of 4 W by using a mode-locker and an internal potassium titanyl phosphate (KTP) doubling crystal. The output from the dye laser is set around 580 nm, an average power of 500 mW, a frequency of about 9.5 MHz, and a pulse width of 8 ps. The output of the dye laser is frequency doubled using a doubler (Super Optronics) to provide a light output of 290 nm with an average power of 20 mW.

2.1.2 Detection system

Our detection system consist of Monochromators (Acton Research Corporation Model AM-511 and SpectraPro 300i) and microchannel plate photomultiplier tubes (MCP-PMT) with a time-resolution of a few ps, and a wavelength range spanning from IR (1.7 μm) to deep UV (down to 200 nm). For time-resolved PL measurement we have a single photon counting system from Ortec, and a streak camera from Hamamatsu (model C-5680) with a time resolution of 2 ps.

We also have an InGaAs detector which has a high sensitivity from 800 – 1700 nm. Its sensitivity increases with increasing of wavelength.

Monochromator: Our monochromators are of Czerny-Turner type with the resolution of 0.01 nm using a 10 μm slit. Diffraction grating disperses the incoming light, resulting in a particular wavelength coming out of the slit to the MCP-PMT.
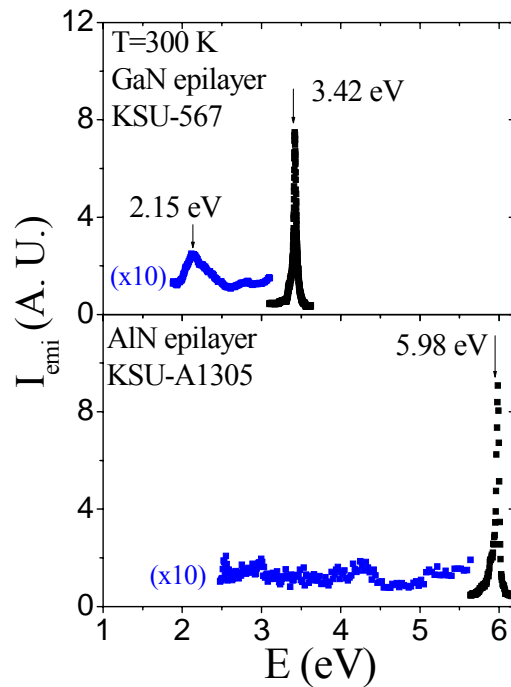
Fig. 2.5 Room temperature PL spectra of AlN compared with GaN.

MCP-PMT: The microchannel plate photomultiplier tube (MCP PMT) consists of a two-dimensional array of a great number of glass capillaries (channels) bundled in parallel and formed into the shape of a thin disk. Each channel acts as an independent electron multiplier. The MCP PMT has a high gain with fast time resolution. Our MCP-PMT has the time resolution of 20 ps. Figure 2.5 shows the continuous wave (CW) PL spectra of AlN and GaN epilayers measured at room temperature.

Time-correlated single photon counting (TCSPC): The TCSPC electronics can be compared to a fast stopwatch with two inputs. The clock is started by the START signal pulse and stopped by the STOP signal pulse. The time measured for one START – STOP sequence will be represented by an increase in a memory value of a histogram, in which the channels on the x-axis represent the time. With a high repetitive light source millions of START – STOP sequences can be measured in a short time. The resulting histogram counts versus channels will represent the fluorescence intensity versus time. A schematic diagram of a conventional single photo counting system is shown in Fig. 2.6.

An electrical pulse is generated by the trigger, i.e. a photodiode. The constant fraction timing discriminators (CFTD) on both the START and the STOP input analyses the pulse shape of the individual pulses. Only pulses higher than a given threshold will be accepted for further signal processing and small amplitude noise pulses are eliminated. An Ortec Model VT120C (voltage gain=20) preamplifier is used before sending the signal to the CFTD. The trigger pulse is sent through the discriminator to the START input of the TAC, which initiates charging of a capacitor. The TAC is a fast clock, started by the START and stopped by the STOP pulse. The START pulse initiates the growth of a ramp signal. Depending on the arrival time of the STOP pulse the ramp will have a lower or higher height. Once the growth of the ramp has been stopped, the level will remain constant for a defined period.
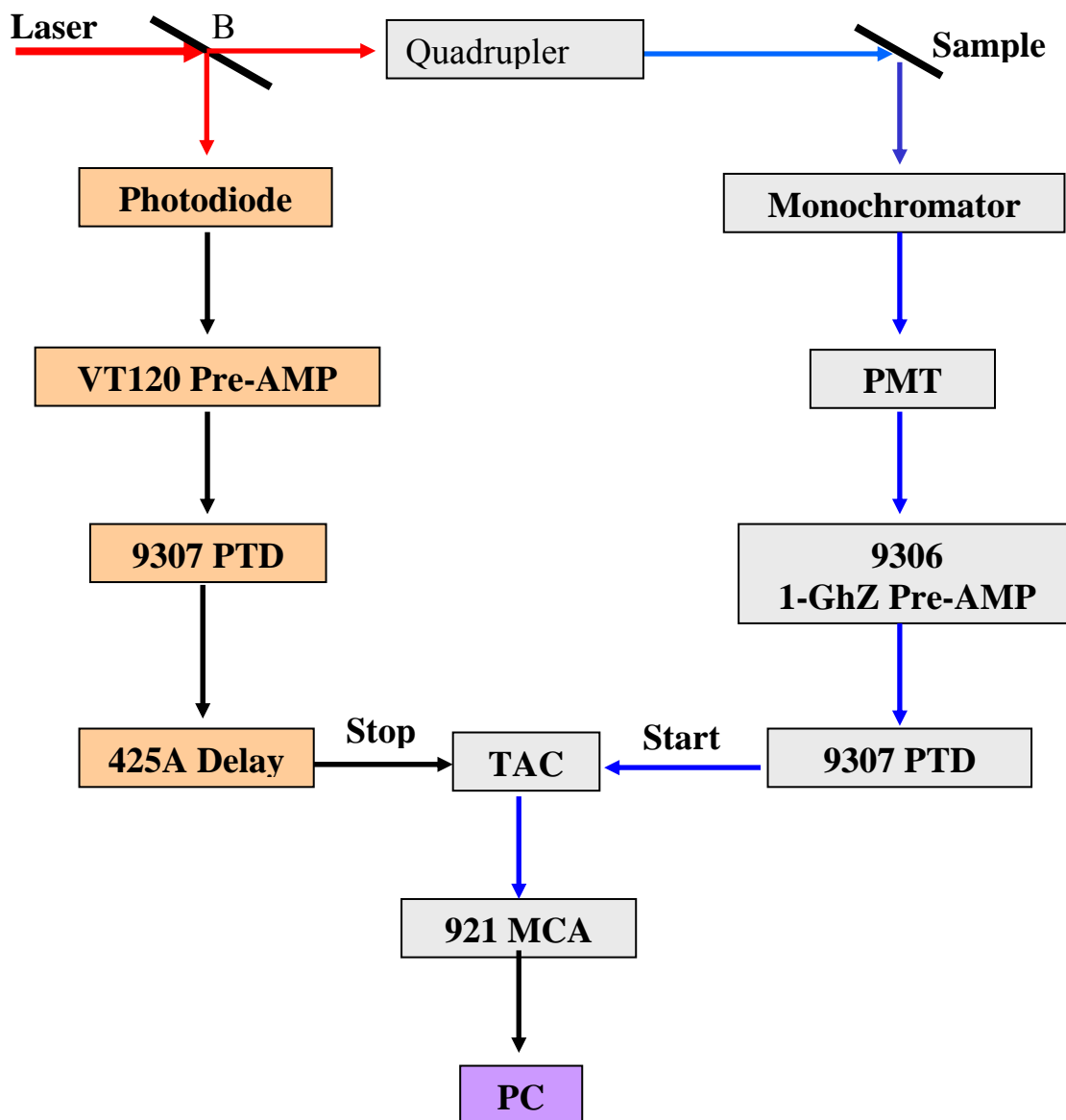
Fig. 2.6 Schematic diagram of a single photon counting system. CFTD is a constant fraction timing discriminator, PTD is pico-timing discriminator, TAC is time-to-amplitude converter, and MCA is multi-channel analyzer.

The signal from the PMT is also amplified by the Ortec Model 9306 1-GHz preamplifier before being used as a timing signal. The arrival time of the signal can be determined by Ortec pico-timing discriminators (PTD) to picosecond precision. The signal after PTD stops the charging ramp in the TAC. The amplitude of TAC is proportional to the charge in the capacitor and hence to the time difference between START and STOP pulses. The output pulse from TAC is converted to digital signal, which is analyzed by micro-channel analyzer (MCA) and a count is stored in numerical value in the corresponding address. Excitation and data storage are repeated until the histogram of number of counts against address number in MCA represents required precision, and thus the decay curve of the sample is obtained. If deconvolution is necessary, the time profile of the excitation pulse is collected in the same way by replacing the sample by a mirror.

If the repetition rate of the laser is too high, the TAC has no time to reset between the occurrence of successive excitation pulses and the distortion is present in the decay curve. The operation of TAC in reverse mode can be used to avoid this problem instead of the standard mode of data collection for ultrafast (MHz) lasers. The signals from PMT are sent to the START input of TAC and the trigger signals to the STOP input. It is preferable to arrange the delays so that TAC sweep is stopped by a trigger signal corresponding to the excitation cycle in which the START signal occurred. The advantage of this technique is that, for high repetition rate lasers, many more of the fluorescence signals are processed by TAC. The data is collected in the MCA with time increasing from higher to lower channel numbers in this reverse mode. An example of a decay lifetime measurement in AlN collected with the TAC in reverse mode is shown in Fig. 2.7.
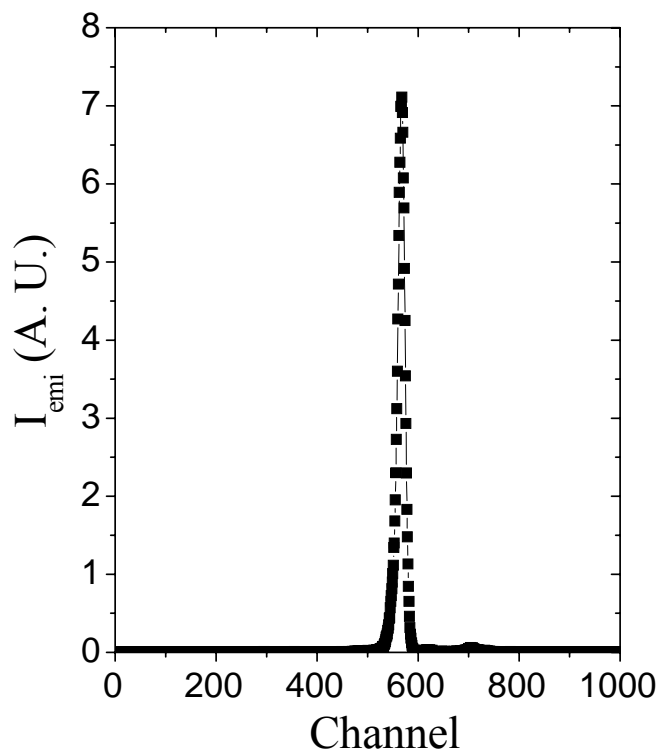
Fig. 2.7 Bandedge transition of AlN measured by TCSPC.

Streak camera: The streak camera is an ultra high-speed detector which captures light emission phenomena occuring in extremely short time periods. It was first developed in 1970 [45]. In streak camera the light pulse to be measured is projected by the lens into an optical image on the photocathode of the streak tube. Pulses with different light intensities are converted into a number of electrons proportional to the intensity of light in photocathode. The emitted electrons are then accelerated. As the group of electrons created from light pulses passes between a pair of sweep electrodes, a high voltage is applied resulting in a high speed sweep. The electrons are deflected at different times and at slightly different angles in the perpendicular direction, and are then conducted to MCP. As the electrons pass the MCP, they

24

are multiplied several thousand times and are then bombarded against the phosphorscreen, where they are converted back into light. The fluorescence image corresponding to the first incident light pulse is positioned at the top of the phosphor screen followed by the others, with images proceeding in the descending order. In other words, the vertical direction on the phosphor screen serves as the time axis. The brightness of the various phosphor images is proportional to the intensity of the respective incident optical pulses. The position in the horizontal direction of the phosphor image corresponds to the horizontal location of the incident light. We can thus find the optical intensity from the phosphor image, and the time and incident light position from the location of the phosphor image. The time-resolution of our streak camera system (Hamamatsu C-5680) is about 2 ps.

2.2 MOCVD growth system

Although there are many techniques to grow III-nitrides, metalorganics chemical vapor deposition (MOCVD) is one of the most efficient techniques among them. In this thesis work, the materials were grown by a custom MOCVD system in a horizontal reactor. The system was built with metal-organic (MO) sources and gas lines. AlGaN alloys were grown on sapphire (0001) substrates with a low temperature AlN buffer layer. Trimethylgallium (TMGa), Trimethylaluminum (TMAl) and NH_3 were used as Ga, Al, and N sources respectively. For Si and Mg doping, SiH_4 and Cp_2Mg were used. The temperature and pressure of MO sources were controlled to ensure constant vapor pressure. All gas flow rates were controlled with mass flow controllers. The reactor is a horizontal quartz reactor with a rectangular shape to control the flow pattern. A 10 kW RF generator (TIG-10/100) is used to heat the susceptor, which is a BN coated graphite susceptor. The growth temperature is measured using a type R thermal coupler and is controlled by a Eurotherm temperature controller (Model-904). Sample growth occurs in a

reactor chamber, where group III MO sources, such as TMG, TMA, and TMI react with group V sources, and deposit on a substrate which can be heated up to 1350^oC to produce III-V semiconductors. A picture of the custom MOCVD system is shown in Fig. 2.8.

Fig. 2.8 A picture of MOCVD system.

2.3 Near-field scanning optical microscope (NSOM)

The resolution of common optical microscope is limited by the Abbe criteria $d > \lambda/(2 \sin \theta)$, where d is distance between two objects, λ is wavelength of light used for illumination, and 2θ is the angle through which light is collected for imaging. The basic principle of near-field optics is that the light passes through a sub-wavelength diameter aperture and illuminates a sample that is placed within its near field, at a distance much less than the wavelength of the

light. The resolution achieved is far better than that of conventional optical microscopes [46]. In NSOM, the resolution is limited by the probe aperture. Picture of the NSOM system used for this work is shown in Fig. 2.9.

Fig. 2.9 A picture of NSOM system.

Our NSOM system has been specifically designed for deep UV experiments down to a wavelength of 190 nm. This is a modified version of the NSOM/SPM-2000™ system from Nanonics Inc [47]. The core of the system consists of a dual (sample and tip) scanner with maximum of 40 μm x-y movement each. Together, it is able to scan a maximum of 80 x 80 μm^2 area of a sample. It has less than 1 nm (5 nm) vertical (horizontal) step size. In the scientific aspect, the applications of NSOM are the imaging of living specimens, the characterization of

advanced materials, and the spectroscopic analysis of semiconductors [48]. Figure 2.10 shows a typical NSOM image of photonic crystal fabricated from InGaN/GaN LED.

NSOM intensity
0.8

X : 1.2 μm   Y : 1.2 μm
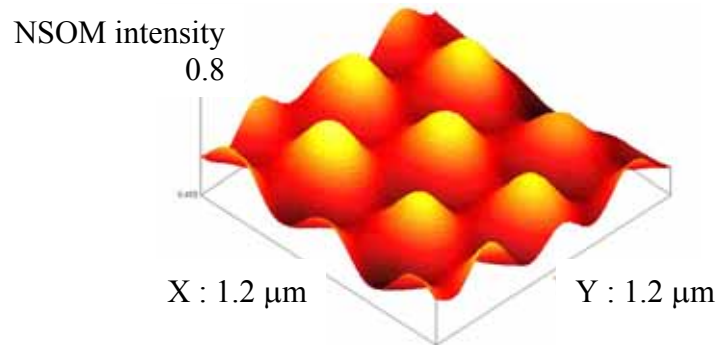
Fig. 2.10 NSOM image of photonic crystals (PCs) fabricated on InGaN/GaN LED.

2.4 Atomic force microscope (AFM)

The atomic force microscope (AFM) is one of the scanning probe microscopes (SPM). All SPMs are based on probing local properties, such as height, optical absorption, magnetism, or electric field. Unlike the optical microscope where resolution is limited by diffraction, resolution in SPM is limited by the size of the probe. AFM measures attractive or repulsive forces between a tip and the sample surface with high resolution (vertical resolution < 1 Å and lateral resolution ~ 10 Å). Our system is the Quesant 250 model [49].
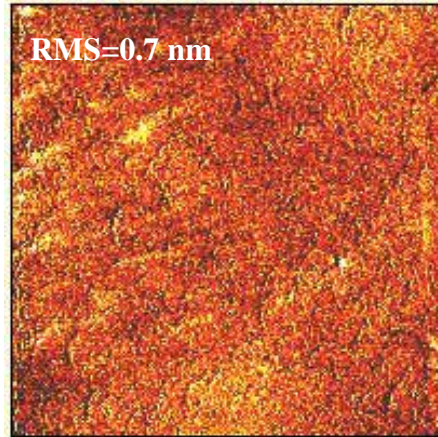
Fig.2.11 AFM image of AlN epilayer (2 μm x 2 μm).

The AFM probe is placed on a cantilever, which is very flexible. As the probe reaches to the proximity of the surface, the cantilever bends due to intermolecular forces. It uses laser beam deflection to measure the cantilever deflection and offers a convenient and sensitive method of measuring surface profile of the sample. A quad photodiode is used as the detector for deflected laser beam. The shift in position of the laser beam will change the quad photodiode voltage and this information is fed back to the Z-piezo to correct the position. The sample remains stationary and the probe scans the surface to form the digital image of surface height profile. It scans a maximum area of 50 x 50 μm^2 and up to 6 μm height. The resolution of AFM is limited by tip radius of the probe. Figure 2.11 shows the AFM image of an AlN epilayer grown at 1325°C.

2.5 Scanning electron microscope (SEM)

Our scanning electron microscope (SEM) is a LEO 440 model with accelerating voltage up to 40 kV. It is used for surfaces characterization and e-beam lithography. It is also coupled with Oxford INCA Energy Dispersive X-ray Spectrometer (EDX). The control of the SEM by these

two systems can be changed by a switch box. Figure 2.12 shows the SEM image of AlN epilayer and photonic crystals (PCs) fabricated on AlN epilayer.
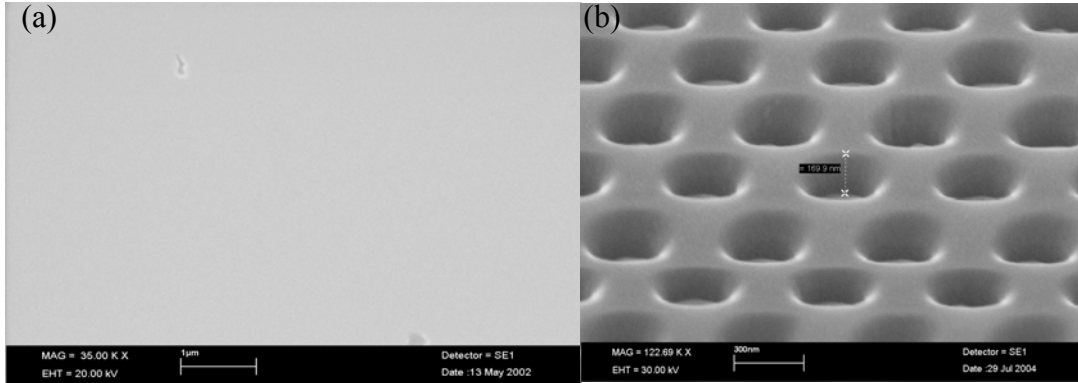
Fig. 2.12 SEM images of (a) AlN epilayer and (b) AlN photonic crystal with periodicity/diameter of 600/300 nm.

2.6 X-ray diffraction (XRD)

XRD is a very useful technique to characterize the materials structure and to study the crystalline quality and defects. It was used to measure the lattice constants and alloy compositions of $Al_xGa_{1-x}N$ alloys. Our XRD (Rigaku RINT 2000V/PC series) can make $2\theta/\theta$ coupled scan and θ or 2θ individual scans. With new designed stage it can measure the rocking curve linewidth in (002), (103) and (102) direction with the resolution of 100 arc sec. Figure 2.13 shows the XRD rocking curve of (002) and (102) peaks of AlN. The diffraction of an x-ray beam by a crystal is given by the Bragg's reflection law of $2d\sin\theta = n\lambda$, where d is the spacing between the reflecting planes, θ is the diffraction angle, and n is the order of the corresponding reflection. The measured 2θ angle varies from -10° to 158°. The source of x-ray is Cu and the wavelengths are 0.154056 nm and 0.154439 nm for Cu $K_{\alpha1}$ and Cu $K_{\alpha2}$, respectively.
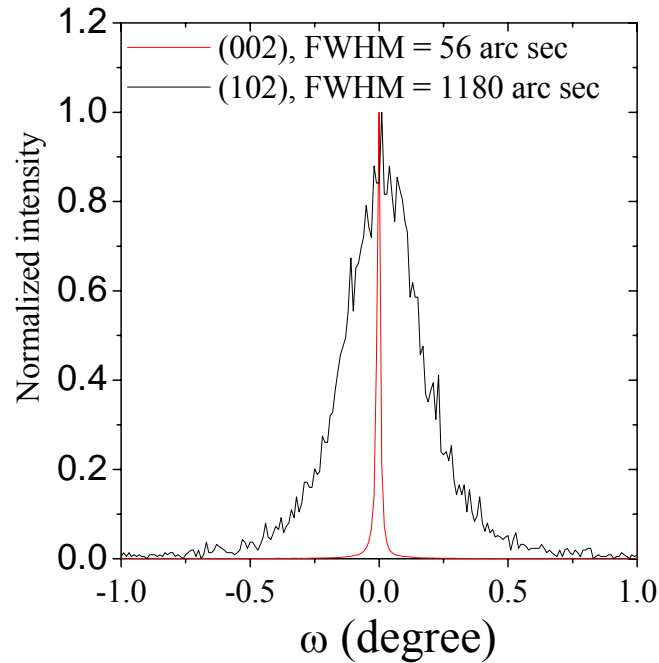
Fig. 2.13 XRD rocking curve of (002) and (102) peaks of AlN epilayer. Full width at half maximum (FWHM) of XRD rocking curve of (002) and (102) peaks are 56 and 1180 arc sec, respectively.

2.7 Other characterization facilities

Variable temperature Hall-effect (Standard Van der Pauw) measurements were employed to measure the electron (or hole) concentration, mobility, and resistivity of AlGaN alloys. Hall measurement system has several unique features such as a large variable temperature range from 10 to 900 K and high measurable sample impedance ($>1G\Omega$). Secondary ion mass spectroscopy (SIMS) is performed by Charles and Evans Associates to determine element or impurity profiles.

CHAPTER 3 Experimental results and discussions

3. 1 Temperature and compositional dependence of the energy bandgap of AlGaN alloys

AlGaN alloys are very attractive for the fabrication of ultraviolet (UV) and deep UV emitters, detectors, and other optoelectronic devices due to the capability of tuning the direct bandgap in large energy range (3.4 to 6.1 eV). They have high mechanical hardness, high thermal conductivity, large dielectric constant, and high resistance to harsh environment. For device applications based on AlGaN alloys, improving the material quality and understanding of the fundamental properties are essential. Many properties of $Al_xGa_{1-x}N$ alloys are unknown due to the increased difficulties to grow high quality materials and decreased emission efficiency with increasing x [50]. Among the basic properties and parameters of $Al_xGa_{1-x}N$ alloys, the determination of the bandgap and its variation with temperature and composition are fundamentally important to the design of practical devices based on these materials.

Compositional dependence of the Varshni coefficients α and β in ZnCdSe alloys between the temperature range 10 - 250 K has been investigated by M. C. Kuo et al. [51]. Y. T. Shih et al. studied the temperature dependence of the bandgap in $Cd_xZn_{1-x}Te$ alloys (x < 0.58) [52]. They found a trend of compositional dependence of α and β. Temperature dependence of the bandgap and Varshni coefficients have been previously measured for binary compounds, GaN and AlN [53]. Temperature dependence of the bandgap of $Al_xGa_{1-x}N$ alloys has been previously measured in the composition range of x < 0.5 and the temperature range between 10 and 300 K, but there was no report on Varshni coefficients (α and β) [54,55]. Absorption spectra of molecular beam epitaxy (MBE) grown $Al_xGa_{1-x}N$ with $0 \leq x \leq 1$ have been measured up to room temperature, from which a negligible composition dependence of α and β was observed [56].

Due to the large bandgap and localization energy of excitons, a broader range and higher measurement temperatures are needed for the accurate determination of the temperature dependence of the bandgap of AlGaN alloys. So far, the compositional and temperature dependence of the bandgap of $Al_xGa_{1-x}N$ alloys in broad ranges have not yet been studied.

In this work, the compositional and temperature dependence of the bandgap of $Al_xGa_{1-x}N$ alloys covering the entire alloy range of x, $0 \leq x \leq 1$ have been measured. Compositional dependence of the Varshni coefficients, α and β, in AlGaN alloys has been empirically determined and a parabolic dependence was observed.

The 1 μm thick $Al_xGa_{1-x}N$ alloys were grown by MOCVD on sapphire (0001) substrates with AlN nucleation layers. Trimethylgallium (TMGa) and trimethylaluminium (TMAl) were used as Ga and Al sources, respectively. Electron dispersive x-ray (EDX) and x-ray diffraction (XRD) spectroscopies were employed to determine the Al contents. Atomic force microscope (AFM) and scanning electron microscope (SEM) were used to characterize the surface morphology of these alloys. The root mean square of the surface morphology measured by AFM was about 1 nm. The samples were mounted stress free on a high temperature stage with a cold finger in a closed-cycle helium refrigerator and temperature was controlled between 10 and 800 K. Deep UV photoluminescence (PL) spectroscopy was employed to investigate the optical emission properties of these samples. The PL system consists of a frequency quadrupled 100 femtosecond Ti:sapphire laser with an average power of 3 mW with excitation photon energy set at 6.28 eV (repetition rate of 76 MHz), a monochromator (1.3 m) [28].

The temperature evolutions of the PL spectra of $Al_xGa_{1-x}N$ were measured from 10 to 800 K covering the entire range of alloys. Figs. 3.1 and 3.2 show representative temperature evolutions of PL spectra of $Al_xGa_{1-x}N$ alloys for x = 0.38 and 0.9.
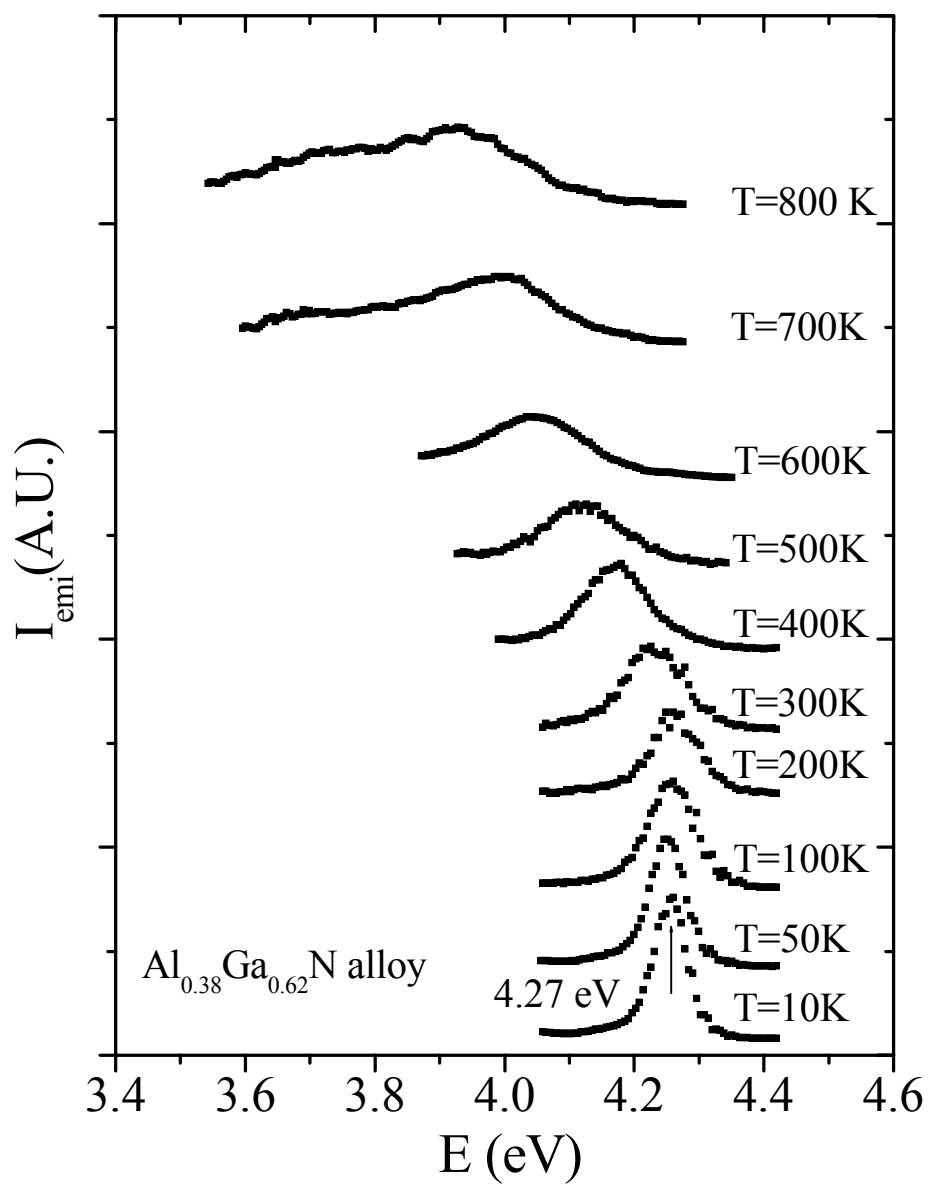
Fig. 3.1 PL spectra of $Al_{0.38}Ga_{0.62}N$ alloy measured from 10 to 800 K.
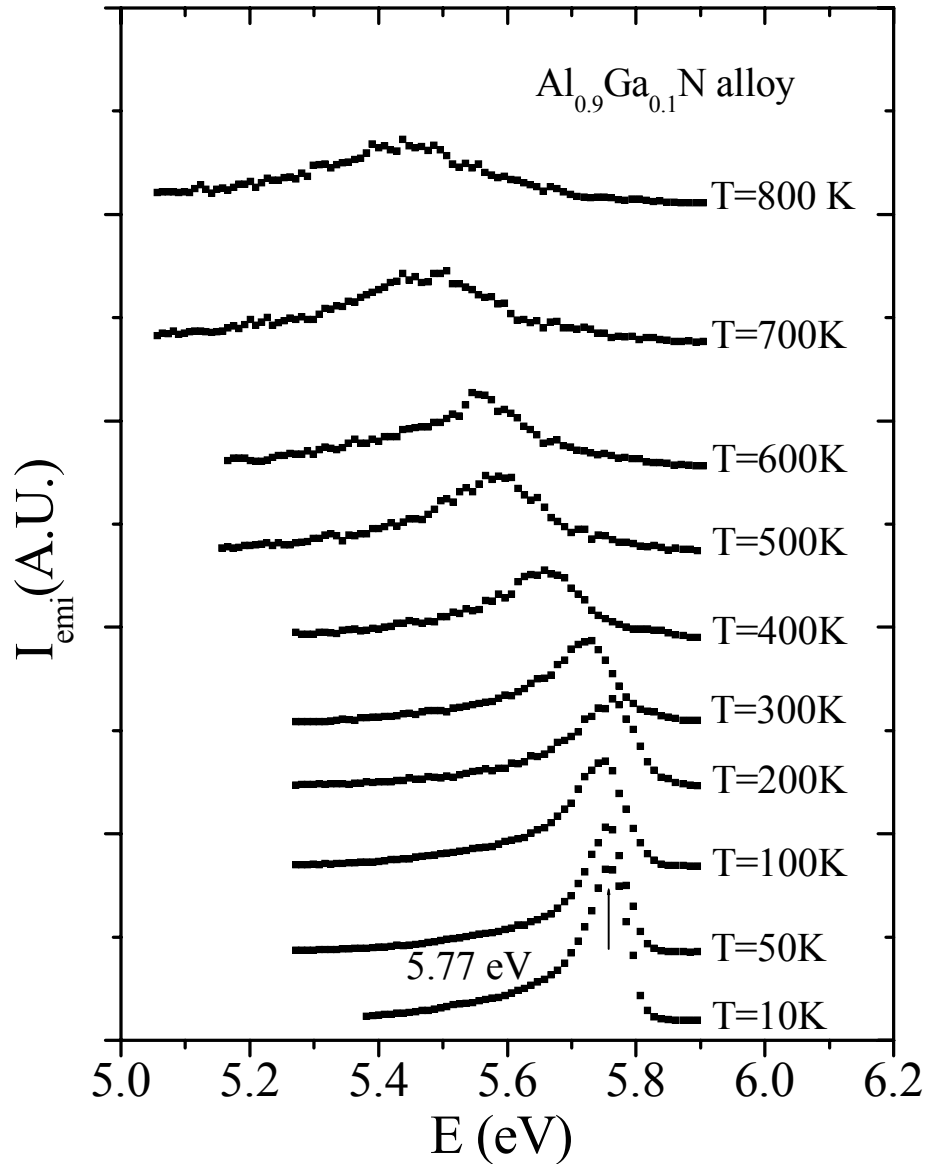
Fig. 3.2 PL spectra of $Al_{0.9}Ga_{0.1}N$ alloy measured from 10 to 800 K.

In general, PL emission intensity, I_{emi}, decreases with increasing temperature. We attribute the dominant band-edge emission lines at low temperatures to the localized exciton recombination [55,57,58]. The spectral peak positions red-shifted from 4.27 eV at 10 K to 3.92 eV at 800 K in $Al_{0.38}Ga_{0.62}N$ alloy. In $Al_{0.9}Ga_{0.1}N$, the dominant emission peak is red-shifted

from 5.77 eV at 10 K to 5.40 eV at 800 K. This red-shift is due to the decreasing of the bandgap with increasing temperature.
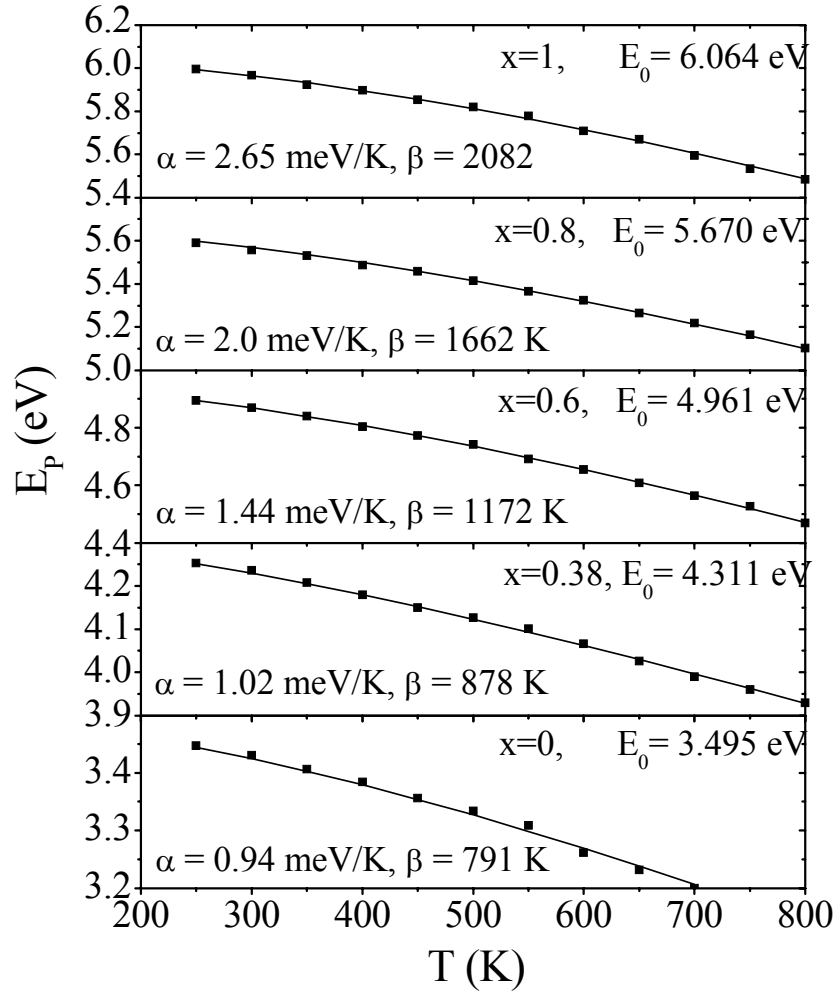
Fig. 3.3 Temperature dependence of the band-edge emission peak between 250 and 800 K for $Al_xGa_{1-x}N$ alloys with different x $(0 \le x \le 1)$. The solid curves are the least squares fit of the data with Eq. (3.1). The fitted vales of α and β are also indicated.

The temperature dependence of bandgap of different semiconductors has been described by different equations [53-55, 59-62]. Among them, Varshni equation is being used most often to

describe non-linear temperature dependence of the bandgap. Figure 3.3 shows the temperature dependence of the band-edge emission peak between 250 and 800 K for different compositions ($0 \leq x \leq 1$).

The solid curves are the least squares fit of experimental data with Varshni equation [63]

$$E_g(T) = E_g(0) - \frac{\alpha T^2}{\beta + T},$$
(3.1)

where $E_g(0)$ is the bandgap of $Al_xGa_{1-x}N$ alloy at T = 0 K; α is an empirical constant; and β is associated with the Debye temperature. Above the Debye temperature, the bandgap changes almost linearly with temperature due to linear changes of lattice parameters and electron-phonon interaction. Because of the large localization energies of excitons in AlGaN alloys, experimental values of the band-edge emission peaks deviate from Varshni equation in the low temperature region (<200 K) [55] and higher measurement temperatures are necessary for an accurate determination of α and β. We apply Eq. (3.1) to fit with experimental data obtained in the high temperature range 200 K – 800 K,where the effect of exciton localization is negligible. This allows us to determine α and β with unprecedented accuracy. From Fig. 3.3, the fitted values of $E_g(0)$ are 3.495 eV for x = 0, 4.311 eV for x = 0.38, 4.961 eV for x = 0.6, 5.649 eV for x = 0.8, and 6.064 eV for x = 1. Whereas, α and β increase from 0.94 meV/K and 791 K for x = 0 to 2.63 meV/K and 2082 K for x = 1. To further validate the present method for obtaining the values of α and β for AlGaN ternary alloys by fitting Eq. (3.1) with high temperature (T > 200K) data, we note that the present values of α and β obtained for binary compounds GaN and AlN using data in the high temperature range of 200 – 800 K are very close to the previously measured values using experimental data ranging from low to high temperatures (10 – 700 K) [53]. The direct comparison can be made for GaN and AlN binary compounds because the

exciton/carrier localization effect due to compositional fluctuation in GaN and AlN is negligibly small. The measured compositional dependence of α and β in $Al_xGa_{1-x}N$ alloys for $0 \leq x \leq 1$ are shown in Fig. 4.4, which clearly exhibits a trend of parabolic increase of α and β with x.
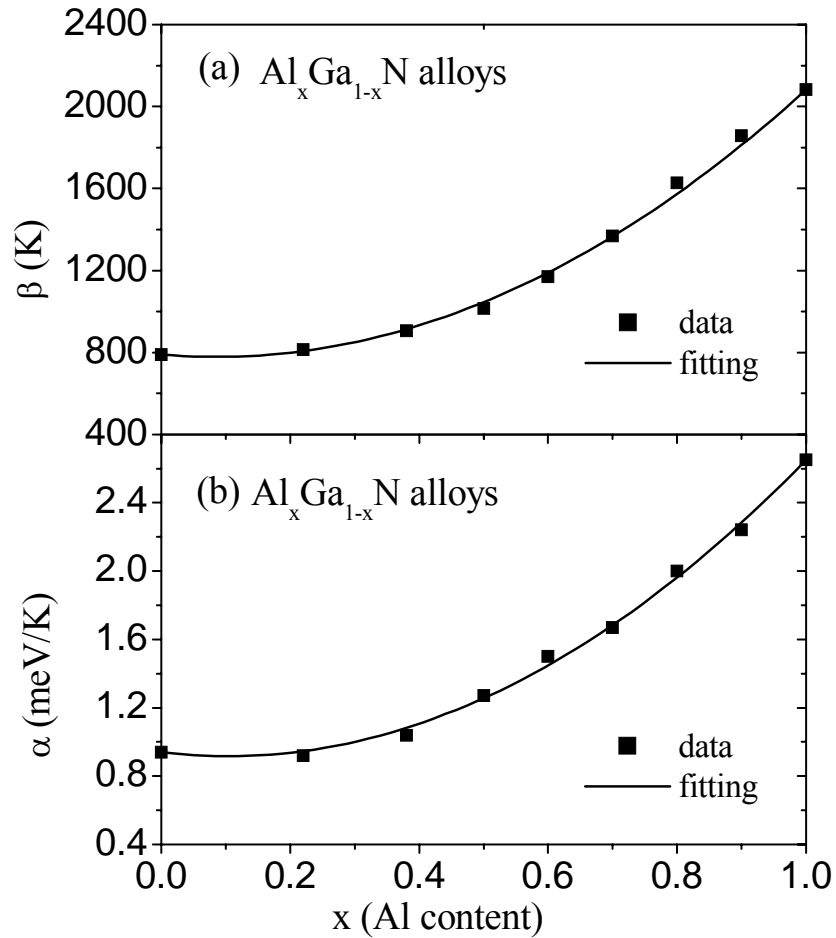
Fig. 3.4 Compositional dependence of the Varshni coefficients (a) $\alpha(x)$ and (b) $\beta(x)$ in $Al_xGa_{1-x}N$ for $0 \leq x \leq 1$. Solid curves are the least square fit of the data with Eqs. (3.2) and (3.3) for $\alpha(x)$ and $\beta(x)$, respectively.

Based on experimental data, we obtain the following empirical equations to describe α and β:

$$\alpha(x) = (1-x)\,\alpha\,(GaN) + x\alpha(AlN) - cx(1-x)\,, \qquad (3.2)$$

$$\beta(x) = (1-x)\,\beta\,(GaN) + x\beta(AlN) - dx(1-x)\,, \qquad (3.3)$$

where c and d are related with quadratic terms of $\alpha(x)$ and $\beta(x)$, and $\alpha(GaN)$, $\alpha(AlN)$, $\beta(GaN)$, and $\beta(AlN)$ are the Varshni coefficients for the binary compounds of GaN and AlN. Solid curves shown in Fig. 3.4 are the least squares fit of the experimental data of $\alpha(x)$ and $\beta(x)$ with Eqs. (3.2) and (3.3). Fitted values of c for $\alpha(x)$ is 2.15 meV/K and d for $\beta(x)$ is 1561 K. By knowing $\alpha(x)$, $\beta(x)$, c, and d together with Eq. (3.1), compositional and temperature dependence of the energy gap, $E_g(x,T)$ of $Al_xGa_{1-x}N$ alloys for the entire alloy range $0 \leq x \leq 1$ can be obtained and described by

$$E_g(x,T) = E_g(x,0) - \frac{\alpha(x)T^2}{\beta(x)+T}\,, \qquad (3.4)$$

where $E_g(x, 0)$ can be written in terms of the low temperature bandgaps of GaN and AlN - the commonly known compositional dependence of the bangap of $Al_xGa_{1-x}N$:

$$E_g(x) = (1-x)E_g(GaN) + xE_g(AlN) - bx(1-x)\,, \qquad (3.5)$$

where b (≈ 1 eV) is the bowing parameter, $E_g(GaN)$ the low temperature band gap value of GaN (≈ 3.5 eV), and $E_g(AlN)$ the low temperature band gap value of AlN (≈ 6.1 eV). It is important to note that compared to the previous published work, the present study employed a broader measurement temperature range covering much higher temperatures, which we believe is

necessary for obtaining accurate measurements of compositional and temperature dependence of the energy bandgap of AlGaN alloy.

In summary, we have measured compositional and temperature dependence of the bandgap of $Al_xGa_{1-x}N$ alloys covering the entire alloy range, $0 \leq x \leq 1$, by employing deep UV PL spectroscopy measurements up to 800 K. Band-edge emission peaks were fitted with Varshni equation to obtain Varshni coefficients α and β. A parabolic dependence of α and β with x in $Al_xGa_{1-x}N$ was observed, from which we have obtained an empirical equation that describes the compositional and temperature variations of the energy bandgap of AlGaN alloys.

3.2 Exciton localization in AlGaN alloys

AlGaN alloys have the capability of tuning the direct band gap in large energy range, from around 3.4 to 6.1 eV, which makes them very useful for ultraviolet (UV) and deep UV optoelectronic device applications. For device applications, high quality AlGaN alloys are essential. It is therefore important to understand better structural, electronic and optical properties of these alloys. One of the important properties, which affect the optical and electrical properties of AlGaN alloy, is the carrier and exciton localization. Exciton localization energy and photoluminescence (PL) emission linewidth yield the information about the compositional and potential fluctuations occurring in semiconductor alloys.

Theoretical and experimental investigations have been carried out to obtain a better understanding of the excitonic emission linewidth in semiconductor alloys [57,58, 64,65]. Coli et al. found that the emission linewidth of the excitonic transition in $Al_xGa_{1-x}N$ alloys increases with Al concentration and reaches a maximum at x ~ 0.7, which implies that the potential fluctuation caused by alloy disorder is also a maximum at that value of x in $Al_xGa_{1-x}N$ alloys. Potential fluctuation causes localization of carriers and excitons at low temperatures. Increase in fluctuating potential barriers in $Al_xGa_{1-x}N$ alloys with x has been reported for x ≤ 0.25 [66]. Increase in exciton localization energy with x in $Al_xGa_{1-x}N$ alloys grown on GaN template for x ≤ 0.76 has been previously reported by fitting data with Bose-Einstein expression in the temperature range between 200 and 300 K [54]. An increase in exciton localization energy (E_{Loc}) from 7 to 34 meV as x increased from 0.05 to 0.35 was also measured by fitting the exciton emission peak energy with the Varshni equation in the temperature range of T ≤ 300°C [55]. However, the direct measurement of E_{Loc} from the Varshni equation and its relation with

the localized exciton activation energy and low temperature emission linewidth in the entire compositional range x, $0 \leq x \leq 1$, has not been previously established in $Al_xGa_{1-x}N$ alloys.

In this work, the effect of exciton localization in $Al_xGa_{1-x}N$ alloys was probed by deep UV PL emission spectroscopy. The exciton localization energy in $Al_xGa_{1-x}N$ alloys of the entire composition range ($0 \leq x \leq 1$) has been measured by fitting the exitonic emission peak energy with the Varshni equation. The relations between the exciton localization energy, the activation energy, and the emission linewidth have been established.

The 1 μm thick $Al_xGa_{1-x}N$ alloys were grown by metalorganic chemical vapor deposition (MOCVD) on sapphire (0001) substrates. Trimethylgallium and trimethylaluminium were used as Ga and Al sources, respectively. Energy dispersive X-ray (EDX) micro-analysis and x-ray diffraction (XRD) were employed to determine Al contents. Atomic force microscopy (AFM) and scanning electron microscopy (SEM) studies revealed excellent surface morphologies. Structural characterization was done with XRD measurement. The samples were mounted on a high temperature stage with a cold finger in a closed-cycle helium refrigerator and temperature was controlled between 10 and 800 K. The deep UV PL spectroscopy system consists of a frequency quadrupled 100 femtosecond Ti:sapphire laser with an average power of 3 mW with excitation photon energy set at 6.28 eV (repetition rate of 76 MHz), and a 1.3 m monochromator (1.3 m) with a detection capability ranging from 185 – 800 nm [28].
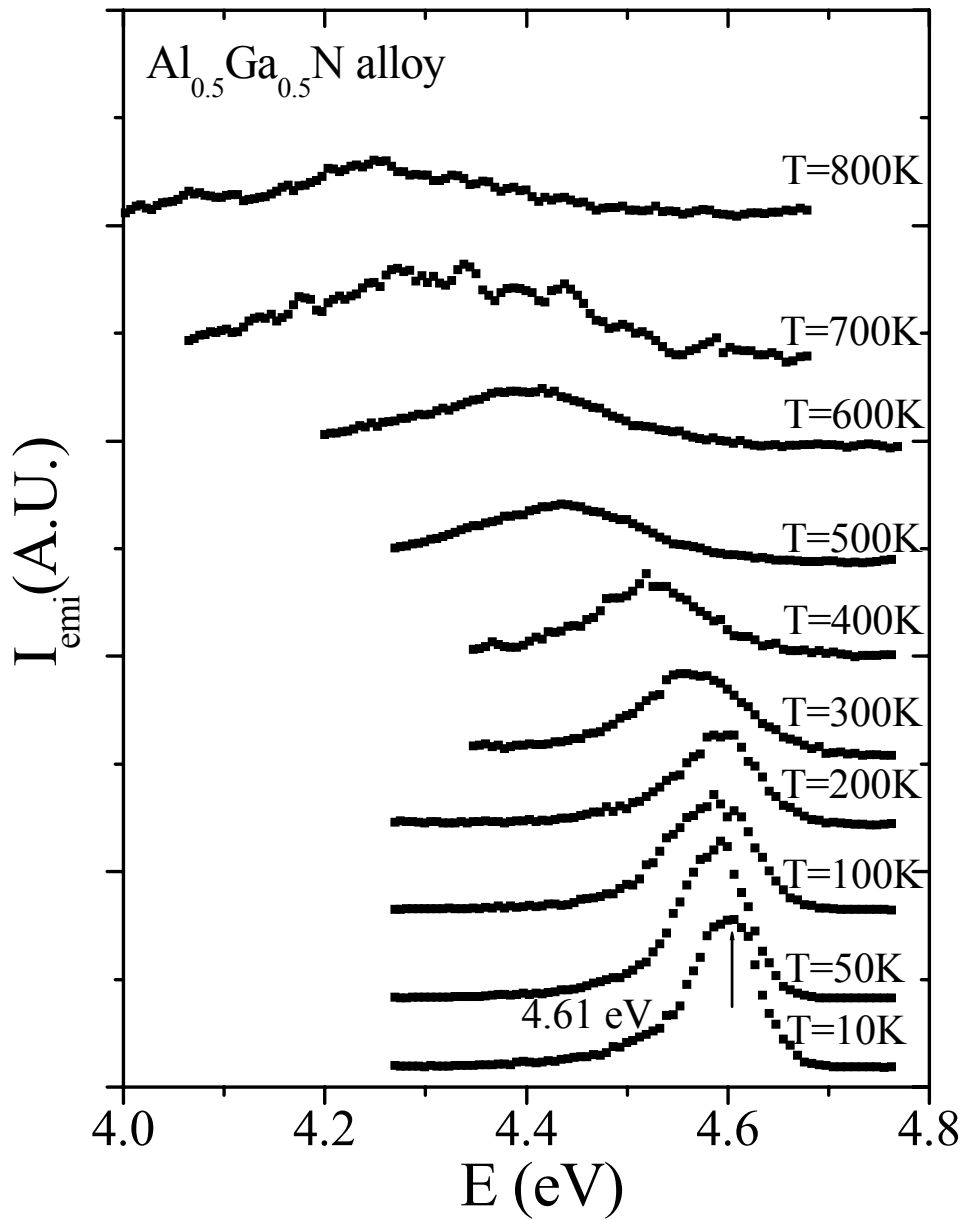
Fig. 3.5 PL spectra of $Al_{0.5}Ga_{0.5}N$ alloy measured from 10 to 800 K.

The temperature evolutions of the PL spectra of $Al_xGa_{1-x}N$ alloys have been measured between 10 and 800 K for the entire composition range. Figure 3.5 shows the temperature evolution of the PL spectra for one representative $Al_xGa_{1-x}N$ sample with x = 0.5. The dominant

emission line at 10 K (4.61 eV) is attributed to the localized exciton transition [54,55,57,58,64-66]. The PL emission intensity, I_{emi}, decreases with increasing temperature due to thermal activation of the localized excitons. The spectral peak position is red-shifted from 4.61 eV at 10 K to 4.25 eV at 800 K due to the variation of the band gap with temperature. The energy band gap variation with temperature for different semiconductors has been previously studied by fitting with different equations [54,55,59-63]. Among them the Varshni equation is the most common to study the non-linear temperature dependence of the band gap. Figure 3.6 shows the temperature dependence of the localized exciton emission peak energy measured between 10 and 600 K for different x (0 ≤ x ≤ 1). The solid lines are the least squares fit of the experimental results with the Varshni equation (3.4) for T > 200 K for $Al_xGa_{1-x}N$ alloys.

At low temperatures, the exciton localization dominates and the PL emission peak energy is lower than the energy value predicted by Eq. (3.4) by an amount of the localization energy. At higher temperatures, the PL emission peak follows the temperature dependence described by Eq. (3.4). Thus, the deviation at the lowest measurement temperature provides a direct measure of the exciton localization energy. Figure 3.7(a) shows E_{Loc} as a function x for $Al_xGa_{1-x}N$ alloys, which clearly shows that the exciton localization energy, E_{Loc}, obtained by measuring the deviation from the Varshni equation also increases with x and reaches maximum for x = 0.7. The measured value of E_{Loc} in $Al_{0.7}Ga_{0.3}N$ alloys is about 95 meV, which is the largest exciton localization energy ever reported for semiconductor alloys. In semiconductor alloys, the excitons are localized at low temperatures and free at higher temperatures. The onset temperature for the localized excitons to become free depends on the degree of localization. Due to the large values of the exciton localization energies, this onset temperature is much higher in

$Al_xGa_{1-x}N$ than in other semiconductor alloy systems and increases with x (for x < 0.7). Thus, a wide measurement temperature range is required to measure E_{Loc} accurately.
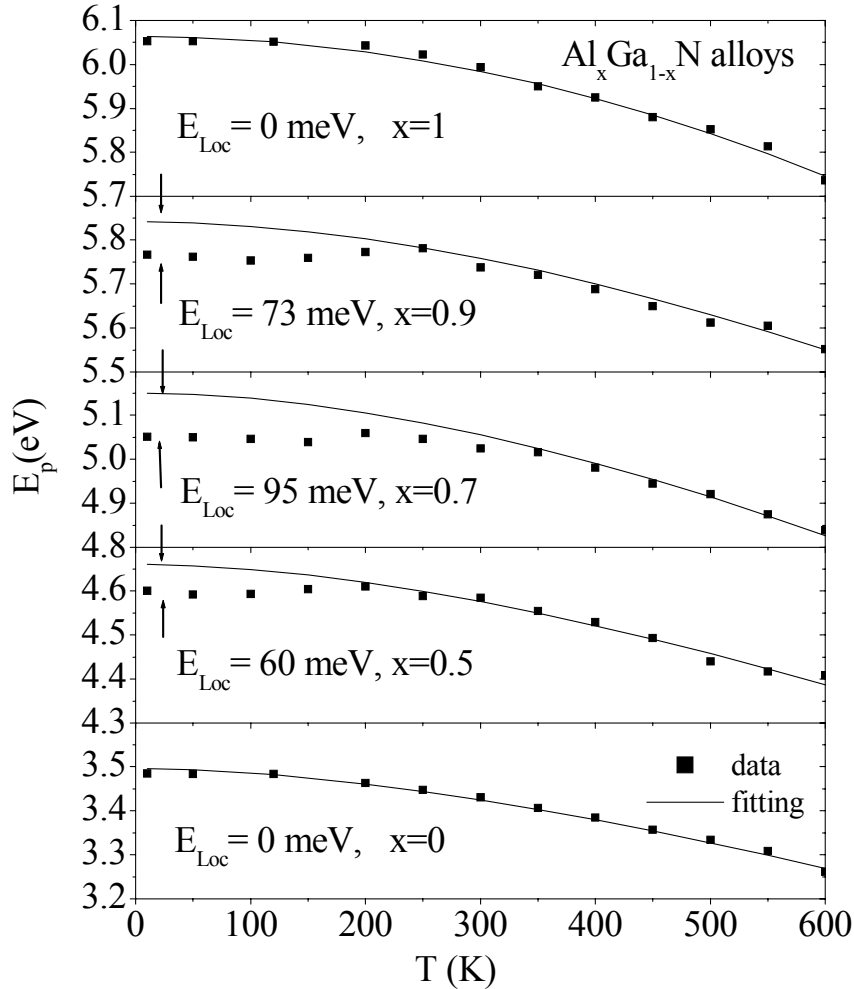
Fig. 3.6 Temperature dependence of the excitonic emission peak energy between 10 and 600 K for different x (0 ≤ x ≤ 1). The solid lines are the least squares fit of the data with Eq. (3.4). Deviations from Eq. (3.4) at the lowest measurement temperatures are the measures of the exciton localization energies, E_{Loc}.
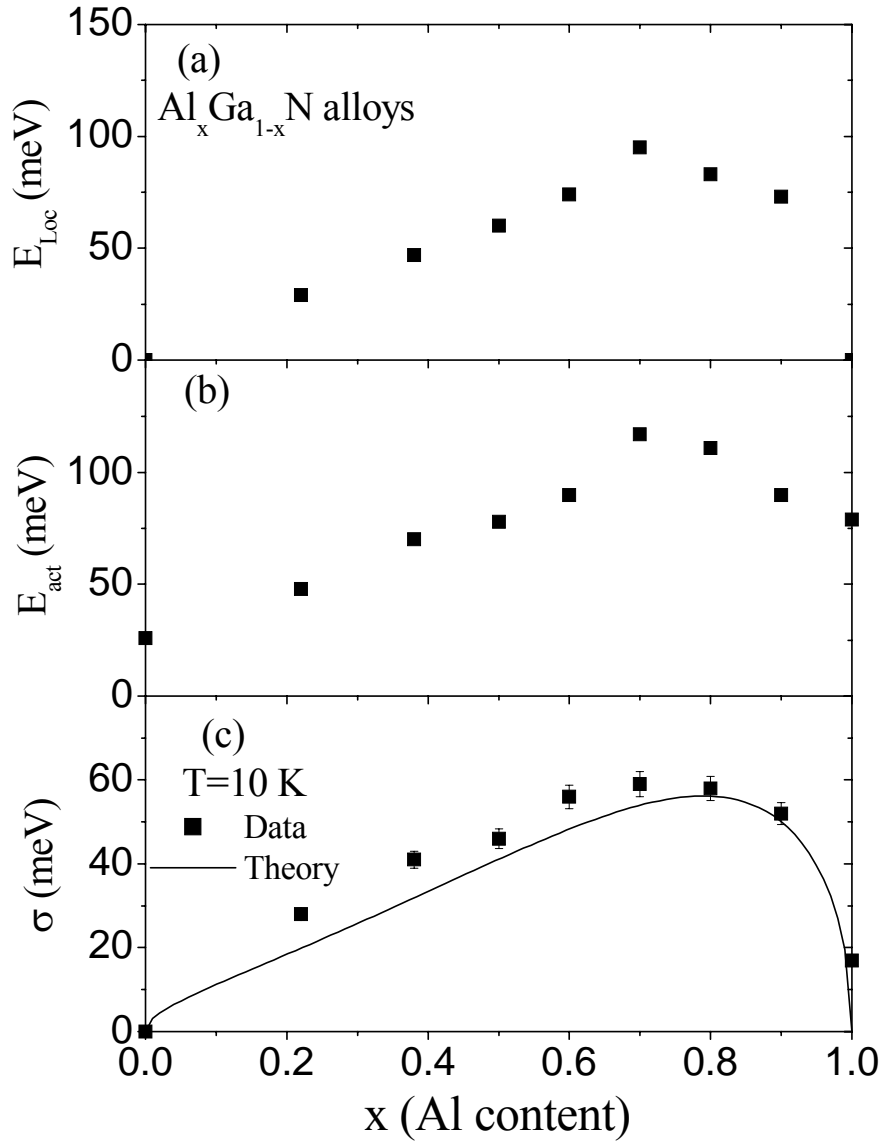
Fig. 3.7 Variations of the (a) exciton localization energy (E_{Loc}), (b) thermal activation energy (E_{act}), and (c) full width at half maximum (σ) of the PL emission line with Al content (x) in $Al_xGa_{1-x}N$ alloys. E_{Loc}, E_{act}, and σ, all increase with x for $x \leq 0.7$, and decrease with x for $x \geq 0.8$, and have a maximum at $x \sim 0.7$. [The solid curve in (c) is a calculation result of Eq. (3.7)]

The integrated emission intensity (I_{emi}) of the localized exciton transition between 150 and 400 K for samples with different x ($0 \leq x \leq 1$) can be well described by the thermal activation process

$$\ln(I_{emi}) = \ln(I_0) - \left(\frac{E_{act}}{k}\right)\frac{1}{T},$$ (3.6)

where E_{act} is the thermal activation energy, and k is the Boltzmann constant. The fitted values of E_{act} as a function of Al content, x are plotted in Fig. 3.7(b). Similar to the behavior of E_{Loc} shown in Fig. 3.7(a), the activation energy increases with x for $x \leq 0.7$ and decreases with x for $x \geq 0.8$.

Alloy heterogeneity also lead to a statistical distribution in the excitonic transition energies, which causes the linewidth broadening. The dependence of the exciton emission line full width at half maximum (σ) on composition, x, can be calculated by employing a quantum statistical approach assuming completely random alloys and is given by [57,58, 65]

$$\sigma(x) = 0.41 \frac{dE_g(x)}{dx} \sqrt{8\ln(2)\, x(1-x) \frac{V_c(x)}{4\pi a_{ex}^3(x)/3}} \,,$$ (3.7)

where $dE_g(x)/dx$ describes the variation of the direct band gap energy with alloy composition, $V_c(x) = a_0^3(x)/\sqrt{2}$ is the volume of primitive cell, and $a_{ex} = \epsilon \hbar^2/\mu e^2$ is the exciton Bohr radius. To calculate the value of $\sigma(x)$ in $Al_xGa_{1-x}N$ alloys, we have used the physical values given in Refs. 57 and 58. We have used lattice constant in the hexagonal plane, $a_0(x) = 3.160(1-x) + 3.112x$ (Å), dielectric constant $\varepsilon(x) = 9.6(1-x) + 6.3x$, effective

47

masses of electrons and holes $m_e/m_0 = 0.22(1-x) + 0.33x$ and $m_h = 1.5m_0$, where m_0 is the electron mass in the free space. The variation of the band gap energy $E_g(x)$ is given as

$$E_g(x) = (1-x)\, E_g\,(GaN) + x\, E_g\,(AlN) - bx(1-x) \qquad (3.8)$$

where b is the bowing parameter. We have used low temperature (T=10 K) band gap $E_g(GaN)$ = 3.5 eV, $E_g(AlN)$ = 6.1 eV, and b = 1 eV.   The measured (squares) and calculated (solid curve) variations of $\sigma(x)$ with x for $0 \le x \le 1$ are shown in Fig. 3.7(c). The error bars are indicated for each x. In the experimental data we have subtracted σ of GaN at 10 K to consider only the compositional disorder. Experimental results appear to be in good agreement with the theoretical calculation. The variation of σ with x follows the same trend as the localization energy and thermal activation energy shown in Fig. 3.7(a) and 3.7(b) and σ increases with x for $x \le 0.7$ and decreases with x for $x \ge 0.8$.   The alloy fluctuation (or σ) is a maximum at x ~ 0.7 instead at x ~ 0.5.   This is because $\sigma(x)$ depends on two terms, $\sigma(x) \propto \sqrt{x(1-x)} \cdot dE_g(x)/dx$.   Although $\sqrt{x(1-x)}$ is symmetric and maximum around x = 0.5, $dE_g(x)/dx$ increases linearly with x. This combination makes $\sigma(x)$ non-symmetric about x ~ 0.5 and having a maximum at x ~ 0.7 instead at x ~ 0.5.

   To see the correlation between the localization parameters, in Fig. 3.8(a), we plot the exciton localization energy obtained by measuring the peak energy deviations from the Varshni equation (E_{Loc}) as a function of the thermal activation energy of the excitonic emission intensity (E_{act}). The solid line is a linear fit of the experimental data with a slope of 1. This establishes the identical characteristic of E_{Loc} and E_{act} in $Al_xGa_{1-x}N$ alloys.
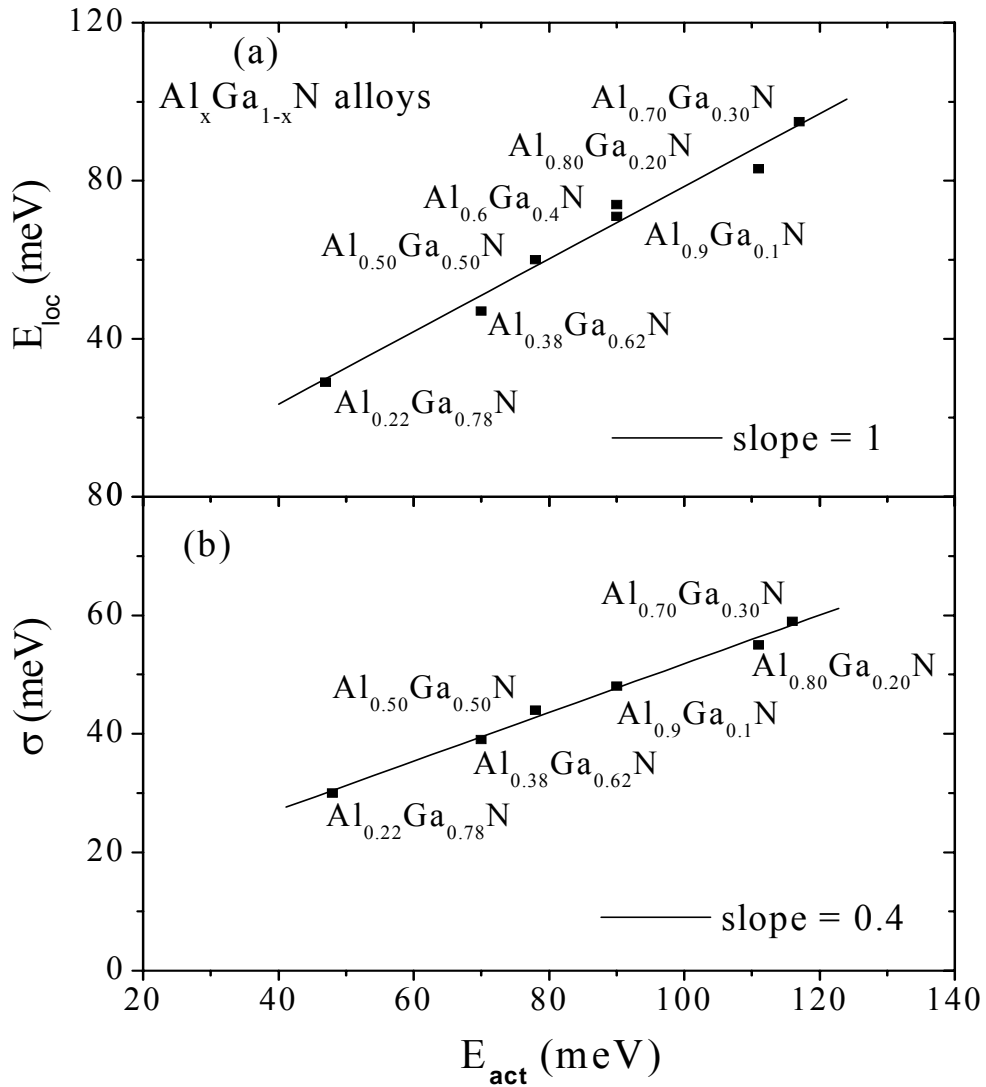
Fig. 3.8 (a) Exciton localization energy (E_{Loc}) as a function of the thermal activation energy (E_{act}) of the localized exciton in AlGaN alloys. Solid line is a linear fit with slope of 1. (b) Full width at half maximum (σ) of the localized exciton emission line as a function of E_{act} in AlGaN alloys. Solid line is a linear fit with slope of 0.4.

Fig. 3.8(b) shows the variations of σ as a function of E_{act}. The solid line is the linear least squares fit of the experimental values with a slope of 0.4 indicating a linear correlation between the exciton localization energy and the emission linewidth in $Al_xGa_{1-x}N$ alloys. S. Lankes et al. found a linear relation ($\sigma = 0.26\,E_{Loc}$) between the localization energy and linewidth in $ZnSe_xTe_{1-x}$ alloys [67].

In summary, we have studied the exciton localization effect in $Al_xGa_{1-x}N$ alloys for the entire composition range, $0 \leq x \leq 1$. Our experimental results demonstrated that the localized exitons in AlGaN alloys have the largest localization energies compared to all other semiconductor alloys. We have established effective methods for directly measuring the exciton localization energies (E_{Loc}) in AlGaN alloys and confirmed that E_{Loc} can be obtained by measuring either the deviation of the exciton emission peak energy with the Varshni equation at low temperatures or the thermal activation energy of the exciton emission intensity or the exciton emission linewidth. The exciton localization energy in $Al_xGa_{1-x}N$ alloys was observed to increase with x and reach maximum for x ~ 0.7, implying that the potential fluctuation caused by alloy disorder is also a maximum at that value of x, consistent with the theoretical calculation result assuming completely random alloys [66,67]. Exciton localization is prominent in wide-gap AlGaN alloys due to their small Bohr radius and a large difference in energy gaps between GaN and AlN. This large exciton localization may give rise to increased quantum efficiency due to reduction of nonradiative recombination rate under the influence of the carrier localization effect. However, carrier localization will reduce significantly the conductivity of AlGaN alloys, particularly for Al content around 70%. Thus, strong carrier and exciton localization can have a significant effect on the optical and electrical properties of deep UV optoelectronic devices.

3.3 Photoluminescence studies of impurity transitions in AlGaN alloys

AlGaN alloys are recognized as promising materials for applications in optoelectronic devices in deep ultraviolet (UV) spectral range. Highly conductive (p- and n-type) AlGaN alloys are essential for device applications. Although n-type AlN has been reported by Si doping with Si energy level ranging from 86 - 250 meV [20-23], further improvements in the material quality and conductivity are still needed for many device applications. One of the major difficulties in obtaining highly conductive n-type Al-rich AlGaN alloys is due to the effect of compensation of electrons by cation vacancies $(V_{III})^{3-}$ and their complexes. It was recognized that suppressing such intrinsic defects could significantly improve the conductivity and material quality of Al-rich AlGaN alloys [20,-23, 29-33].

Theoretical and experimental studies have been carried out to explore different intrinsic defects in III-nitrides. Calculations have indicated that the cation vacancy and its complex in undoped and Si-doped AlGaN alloys (particularly in Al-rich alloys) have small formation energies and are easily formed during the crystal growth [23,29-32]. The capacitance deep-level transient spectroscopy studies revealed that at least three dominant deep levels with the same origin in low Al content n-type AlGaN alloys [68]. We have reported two groups of deep impurity transitions in $Al_xGa_{1-x}N$ alloys, which were assigned to the recombination between shallow donors and two different deep acceptors [33], one of which was identified as an isolated cation vacancy with 3-negative charges $(V_{cation})^{3-}$ and the other V_{cation} complex with 2-negative charges $(V_{cation}\text{-complex})^{2-}$. The energy levels of these deep acceptors in AlGaN alloys are pinned to common energy levels in vacuum [33]. By minimizing the densities of these defects, we have been able to achieve a room temperature n-type resistivity of about 40 Ωcm with a free electron concentration of about 1×10^{17} cm^{-3} in Si-doped AlN epilayers grown on sapphire

substrates [21]. More recently, a room temperature resistivity as low as 1 Ωcm with an electron concentration up to 7.4×10^{17} cm^{-3} has also been reported for Si-doped AlN epilayers grown on SiC substrates by molecular beam epitaxy (MBE) [23].

In this work, deep UV photoluminescence (PL) studies of impurity transitions in $Al_xGa_{1-x}N$ alloys grown on sapphire substrates by metal organic chemical vapor deposition (MOCVD) has been carried out. In addition to the previously reported V_{III}^{3-} and $(V_{III}\text{-complex})^{2-}$ related transitions, a group of impurity transitions with higher emission energies has been observed. Based on the spectral peak positions, decay lifetime measurements, and the similar features with V_{III}^{3-} and $(V_{III}\text{-complex})^{2-}$ related transitions, we attributed this group of impurity transitions to the recombination between shallow donors (Si) and deep acceptors involving cation vacancy complexes with one-negative charge, $(V_{III}\text{-complex})^{1-}$.

Undoped and Si-doped $Al_xGa_{1-x}N$ alloys of about 1 μm thick were grown by MOCVD on AlN/sapphire templates. Trimethylgallium (TMGa) and trimethylaluminium (TMAl) were used as Ga and Al sources, respectively. The Al contents of $Al_xGa_{1-x}N$ ($0\leq x \leq1$) alloys were determined by energy dispersive x-ray (EDX) and x-ray diffraction (XRD) measurements. The full width at half maximum (FWHM) of the XRD rocking curve of the (0002) reflection peaks was between 50 to 300 arcsec. Atomic force microscope (AFM) and scanning electron microscopy (SEM) were employed to study the surface morphology of these AlGaN alloys, which revealed crack free smooth surfaces with a roughness of about 1 nm across a 2 μm x 2 μm scanning area. Deep UV PL spectroscopy was employed to investigate the emission properties of $Al_xGa_{1-x}N$ epilayers. The PL system consists of a frequency quadrupled 100 femtosecond Ti:sapphire laser with an average power of 3 mW with excitation photon energy set at 6.28 eV (repetition rate of 76 MHz), and a monochromator (1.3 m) [28].

Room temperature (300 K) PL spectra for a set of $Al_xGa_{1-x}N$ alloys covering the entire alloy range are shown in Fig. 3.9. The bandedge transition peak energy blue-shifts from 3.42 eV for x = 0 to 5.96 eV for x = 1 in $Al_xGa_{1-x}N$ alloys. In addition to the bandedge transition, each spectrum also exhibits deep impurity transitions. The impurity emission peak at around 2.15 eV (yellow line or YL) in GaN has been extensively studied. It was previously attributed to the transition from a shallow donor to a deep acceptor [29,30, 69-72]. It was suggested that the deep acceptor involved in YL may be linked to V_{Ga}-O_N and V_{Ga}-$2O_N$ based on local-density-functional calculation [73]. Since O_N sits as a next neighbour of V_{Ga} to reduce the coulomb energy, V_{Ga} forms defect complex with it [29,30]. More recent studies have suggested that the deep acceptor involved in the YL is related to V_{Ga} complexes with two negative charges (V_{III}-complex)$^{2-}$ such as (V_{Ga}-O_N)$^{2-}$ or (V_{Ga}-Si_{Ga})$^{2-}$ [31-33]. The PL emission peak at 3.4 eV (violet line or VL) in AlN was first observed by Youngman and Harris [74]. Our recent studies have suggested that the VL in AlN is due to the transition from shallow donors to isolated Al vacancies with 3-negative charges (V_{Al})$^{3-}$ [33]. Al-rich AlGaN alloys with reduced emission intensities associated with deep impurity transitions generally show improved conductivity. By examining the PL spectra shown in Fig. 3.9, besides (V_{III})$^{3-}$ and (V_{III}-complex)$^{2-}$, a group of impurity transitions (indicated with dark arrows) with emission energies above those of (V_{III})$^{3-}$ and (V_{III}-complex)$^{2-}$ related transitions have been observed in $Al_xGa_{1-x}N$ alloys. The spectral peak position of this group of impurity transitions blue-shifts from 2.86 eV in GaN to 4.71 eV in AlN. The blue band (2.8 eV) has been observed in Si and undoped GaN in PL, cathodoluminescence (CL), and photoconductivity measurements [75-77] and was attributed to a V_{Ga}-O_N complex [75].
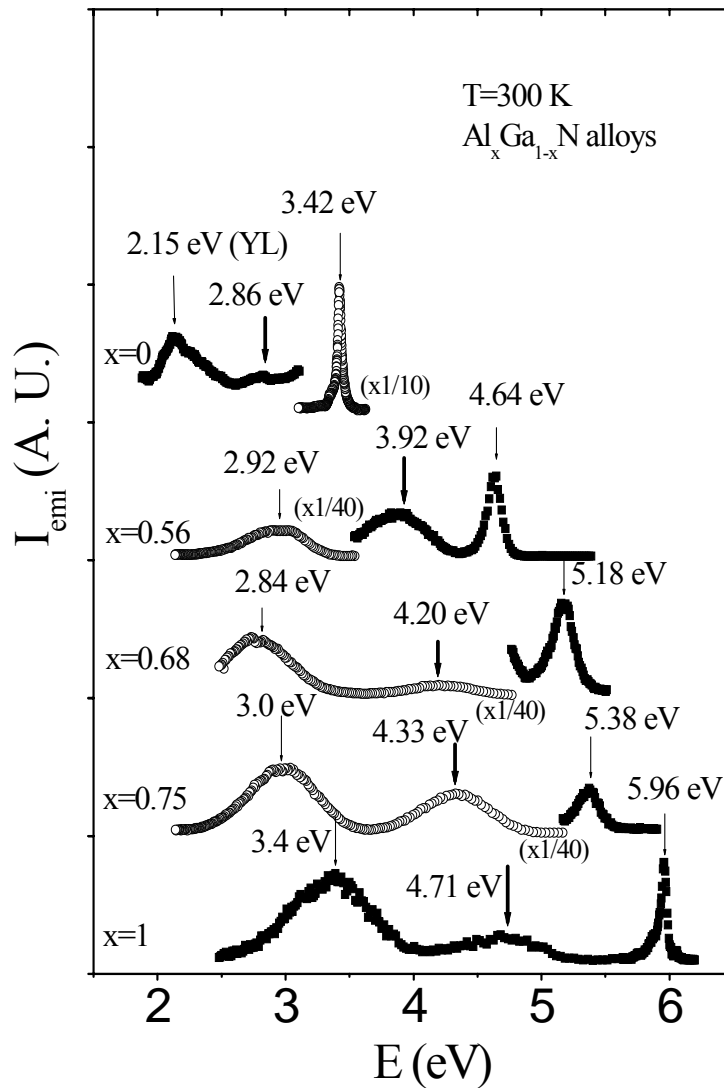
Fig. 3.9 Room temperature PL spectra of $Al_xGa_{1-x}N$ alloys with x between 0 and 1, showing the bandedge and impurity transitions. A new group of impurity transitions has been identified and their peak positions are marked with bold arrows.

In Fig. 3.10, we plot the room temperature PL spectral peak position (E_{imp}) of newly observed impurity transition in $Al_xGa_{1-x}N$ alloys as a function of x (closed squares) together with

those of $(V_{III})^{3-}$ and $(V_{III}$-complex$)^{2-}$ related transitions (open circles and open squares, respectively) [33].
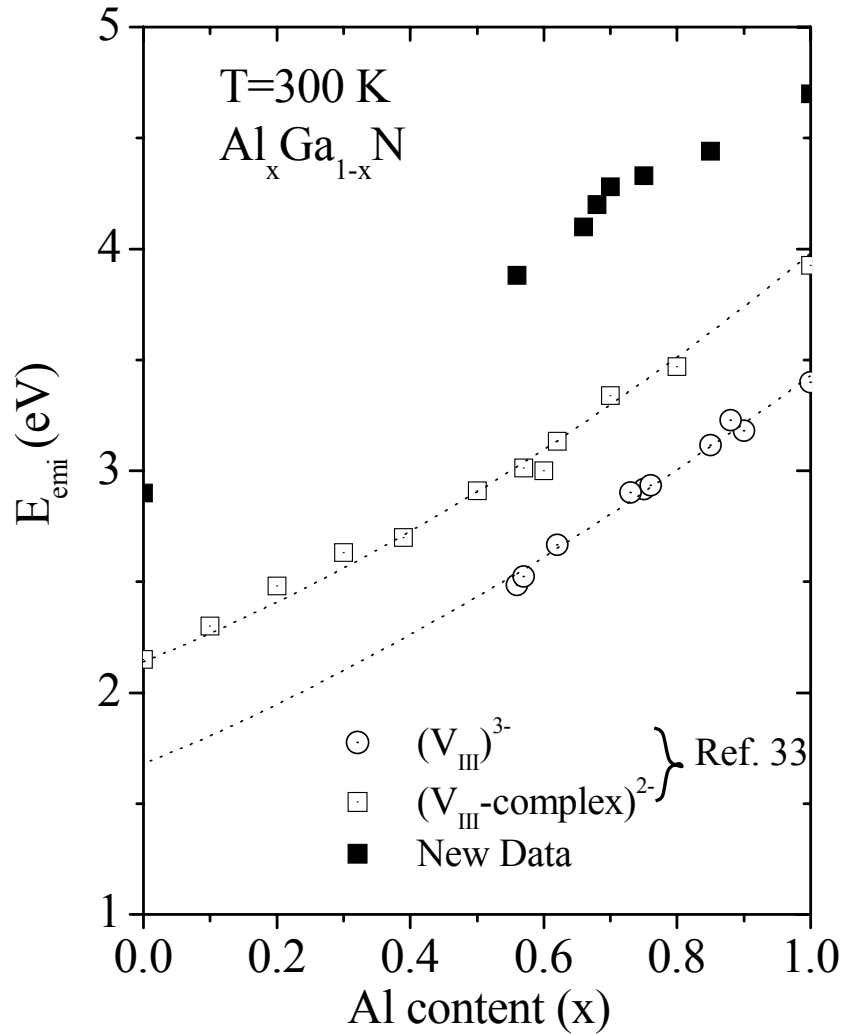
Fig. 3.10 PL peak position (E_{imp}) of the newly observed impurity transition obtained from Fig. 3.9 (closed squares) and those of $(V_{III})^{3-}$ and $(V_{III}$-complex$)^{2-}$ related transitions from Ref. 33 (open circle and squares) in $Al_xGa_{1-x}N$ as functions of Al content (x). Dotted lines are guide to the eyes.

The energy position of this impurity transition shows a continuous increase with x and follows the same trend as those of $(V_{III})^{3-}$ and $(V_{III}\text{-complex})^{2-}$ related impurity transitions, indicating that they are of the similar nature – the presently observed impurity transition shown in Fig. 3.9 is of donor-acceptor pair (DAP) type involving shallow donors and deep acceptors. Our time-resolved PL measurements also revealed long decay lifetimes (longer than 0.1 μs) for this group of impurity transitions, which supports our assignment.

To further identify the origin of this deep acceptor, we plot in Fig. 3.11 its energy level (E_A) together with the conduction (E_c) and valence (E_v) band edges as functions of Al content (x). In obtaining Fig. 3.11, we used the commonly known compositional dependence of the bangap of $Al_xGa_{1-x}N$, $E_g(x) = (1-x)E_g(GaN) + xE_g(AlN) - bx(1-x)$, where the bowing parameter (b) and the room temperature energy bandgaps of GaN and AlN were taken as 1, 3.44 and 6.05 eV, respectively. The conduction (E_c) and valence (E_v) band offset parameters have been assumed to be 70% and 30% for $Al_xGa_{1-x}N$ ($0 \leq x \leq 1$) alloys, respectively. The valence band maximum of GaN is chosen as E=0. The chemical origin of the shallow donors involved here is believed to be either Si or O in $Al_xGa_{1-x}N$ alloys. Assuming the ionization energies of the shallow donors (E_D^0) increase linearly from 25 to 86 meV with varying x from 0 to 1 in $Al_xGa_{1-x}N$ alloys [20,21], the acceptor level (E_A) deduced from in Figs. 3.9 and 3.10 with neglecting the Coulomb interaction between the ionized donors and acceptors is then given by

$$E_A = E_g(x) - E_{emi} - E_D + E_v \quad\quad\quad\quad (3.9)$$

where $E_g(x)$ is the bandgap of $Al_xGa_{1-x}N$ alloys, $E_v = -0.3\Delta E_g(x)$, $E_c = E_g(GaN) + 0.7\ \Delta E_g(x)$, and E_D is the shallow donor energy level. E_A is plotted in Fig. 3.11 (closed squares) together with E_c

and E_v as functions of x. The result clearly shows that the newly observed deep acceptor has a binding energy of 1.25 eV (0.55 eV) in AlN (GaN). The striking feature is that, similar to $(V_{III})^{3-}$ and $(V_{III}\text{-complex})^{2-}$ deep acceptor levels in $Al_xGa_{1-x}N$ alloys, the deduced energy level of the presently observed deep acceptor as a function of x is also a horizontal line in the whole range of x. This clearly indicates that the energy levels of these deep acceptors in $Al_xGa_{1-x}N$ alloys are also pinned to a common energy level in vacuum with energy separations of 0.7 eV and 1.2 eV from those of $(V_{III}\text{-complex})^{2-}$ and $(V_{III})^{3-}$, respectively.

The formation energies (E_f) of cation vacancies and vacancy complexes have been calculated in GaN and AlN, which shows that E_f of $(V_{III})^{3-}$ and $(V_{III}\text{-complex})^{2-}$ are lower than that of $(V_{III}\text{-complex})^{1-}$ and anion vacancies cannot be formed in Si doped GaN and AlN [30-32]. From the energy position relative to the those of $(V_{III})^{3-}$ and $(V_{III}\text{-complex})^{2-}$, we believe that the deep level acceptor involved in the presently observed impurity transitions is cation vacancy complex with one-negative charge $(V_{III}\text{-complex})^{1-}$, such as $(V_{Ga}\text{-}2O_N)^{1-}$. The possibility of isolated $(V_{III})^{1-}$ as the origin of the presently observed deep acceptor in $Al_xGa_{1-x}N$ alloys can be excluded due to its much higher formation energy than $(V_{III}\text{-complex})^{1-}$. The binding energies of the $(V_{III}\text{-}2O_N)^{1-}$ deep level acceptors increase almost linearly from about 0.55 to 1.25 eV with varying x from 0 to 1 in $Al_xGa_{1-x}N$ alloys. The calculated binding energy of $(V_{Al}\text{-}2O_N)^{1-}$ ranges from 1.0 to 1.12 eV in AlN [30-32]. The calculated differences in binding energies between $(V_{III})^{3-}$ and $(V_{Al}\text{-}O_N)^{2-}$ and between $(V_{Al}\text{-}O_N)^{2-}$ and $(V_{Al}\text{-}2O_N)^{1-}$ in AlN, respectively, are about 0.5 and 0.7 eV [30-32], which agree perfectly with our experimentally measured values shown in Fig. 3 (0.5 and 0.7 eV).
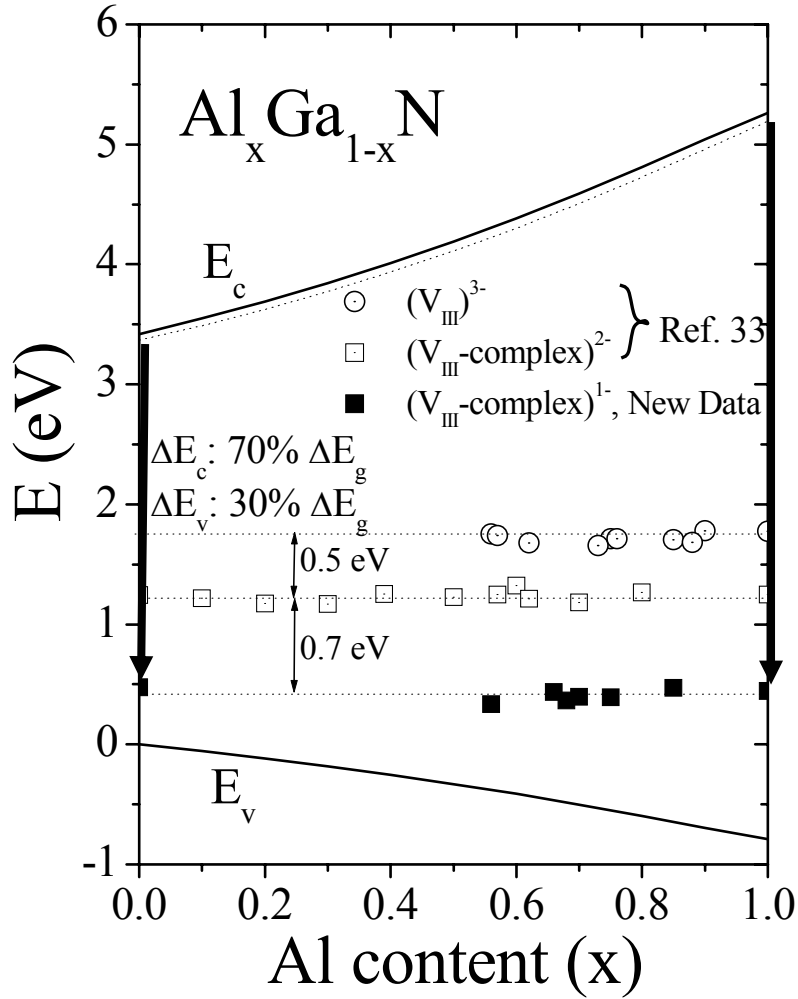
Fig. 3.11 The deep acceptor energy levels (E_A) associated with (V_{III}-complex)$^{1-}$ (closed squares), (V_{III}-complex)$^{2-}$ (open squares) and (V_{III})$^{3-}$ (open circles) obtained from Figs. 3.9 and 3.10 and Ref. 33 plotted together with E_c, E_v, and E_D^0 as functions of Al content (x).

Since (V_{III}-2O_N)$^{1-}$ captures only one electron, their presence will not detriment the conductivity as severely as the presence of (V_{III})$^{3-}$ and (V_{Al}-O_N)$^{2-}$ defects, which is consistent with our experimental results presented in Fig. 3.12. Fig. 3.12 illustrates the evolution of room temperature (300 K) PL spectra and resistivity of $Al_xGa_{1-x}N$ alloys (x~0.66) grown under various conditions. The arrows indicate the peak positions of the spectra. All samples exhibit a

bandedge transition at 5.10 eV and the bandedge emission intensity increases with decreasing resistivity.
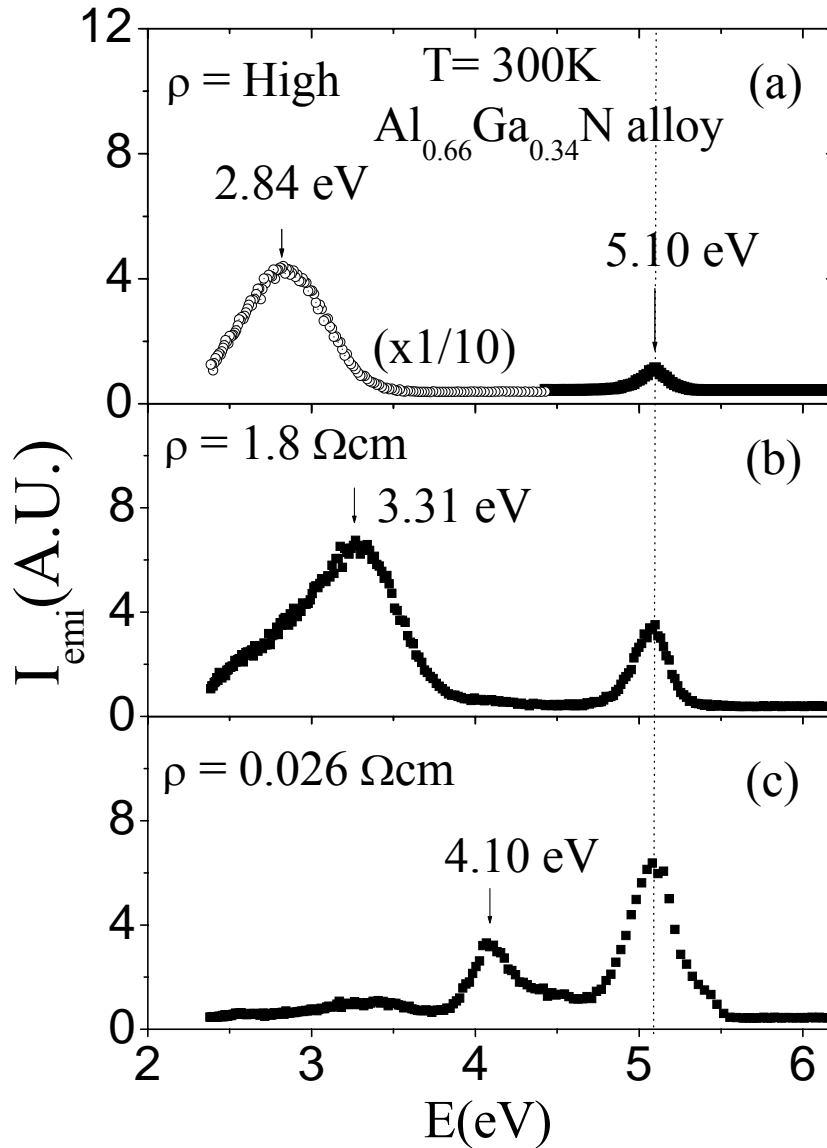
Fig. 3.12 Room temperature PL spectra of $Al_{0.66}Ga_{0.34}N$ alloys with different resistivities.

As shown in Fig. 3.12(a), for an early grown Si-doped $Al_{0.66}Ga_{0.34}N$ alloy with high resistivity (beyond our instrument limitation), the dominant impurity peak at 2.84 eV is related to the isolated cation vacancy, $(V_{III})^{3-}$ [33]. The triply charged cation vacancy captures three

electrons and thus their presence significantly increases the resistivity. As illustrated in Fig. 3.12(b), suppression of $(V_{III})^{3-}$ related transition results in a reduction in resistivity to 1.8 Ωcm and simultaneously an emission peak at 3.31 associated with the presence of $(V_{III}\text{-complex})^{2-}$ [33]. Since V_{III}^{3-} and $(V_{III}\text{-complex})^{2-}$ defects in AlGaN alloys capture three and two electrons, respectively, these defects act as compensating centers for n-type doping and their densities have to be minimized in order to further enhance the conductivity. As illustrated in Fig. 3.12(c), once $(V_{III})^{3-}$ and $(V_{III}\text{-complex})^{2-}$ related transitions were suppressed by varying the growth conditions, we have significantly reduced the sample resistivity to 0.026 Ωcm. However, the impurity transition involving $(V_{III}\text{-complex})^{1-}$ at 4.10 eV is evident. We believe that the conductivities of Al-rich AlGaN alloys and pure AlN will continue to improve by further reducing the densities of the intrinsic defects - cation vacancies (and complexes) with triple, double, and single negative charges.

In summary, we have investigated impurity transitions involving cation vacancies and complexes in $Al_xGa_{1-x}N$ alloys between x = 0 and 1 grown on sapphire substrates by MOCVD. A group of impurity transitions of DAP type with higher emission energies than those of the previously identified $(V_{III})^{3-}$ and $(V_{III}\text{-complex})^{2-}$ related transitions was observed. The deep level acceptors involved in these transitions have been identified as $(V_{III}\text{-complex})^{1-}$. The energy levels of these deep acceptors in $Al_xGa_{1-x}N$ alloys increase almost linearly with x from 0.55 eV in GaN to 1.25 eV in AlN and are pinned to a common energy level in vacuum. Experimentally measured energy difference between the $(V_{III}\text{-complex})^{2-}$ and $(V_{III}\text{-complex})^{1-}$ deep level acceptors in AlGaN alloys (0.7 eV) agrees with the calculated value (0.7 eV). AlGaN alloys predominantly exhibiting the bandedge and $(V_{III}\text{-complex})^{1-}$ transitions possess improved conductivities over those emitting predominantly $(V_{III})^{3-}$ and $(V_{III}\text{-complex})^{2-}$ related transitions.

3. 4 Time-resolved photoluminescence studies of Mg-doped AlN epilayers

AlN with a bandgap 6.1 eV is emerging as an important semiconductor due to its applications in ultraviolet (UV) light emitters, laser diodes (LDs), and other optoelectronic devices. It has high mechanical hardness, high thermal conductivity, large dielectric constant and high resistance to harsh environment [78]. AlN is unique due to the fact that no other semiconductor possesses such a large direct bandgap as well as the ability of bandgap engineering through the use of heterostructures. By alloying AlN with GaN, the band-gap changes systematically from 3.4 to 6.1 eV, that can be used to tune the wavelength of optoelectronic devices in UV and deep UV spectral ranges. For device applications, conductive AlN and $Al_xGa_{1-x}N$ with high x are essential. P-type doping in $Al_xGa_{1-x}N$ has been proven to be extremely difficult due to high activation energy of Mg dopant as well as reduced crystalline quality of the alloys. The resistivity of Mg-doped $Al_xGa_{1-x}N$ was found to increase with increasing x and it is expected to be extremely high in Mg-doped AlN. Our group has obtained p-type $Al_xGa_{1-x}N$ alloys with x up to 0.27 with Mg doping [26]. We have obtained a room temperature resistivity of around 10^5 Ωcm for $Al_{0.7}Ga_{0.3}N$ and confirmed p-type conduction at elevated temperatures (>700 K) with a resitivity of 40 Ωcm at 800 K [79]. Our group has grown high optical quality AlN epilayers on sapphire substrate by metalorganic chemical vapor deposition (MOCVD) [80]. Very efficient bandedge PL emission lines have been observed with above bandgap excitation. Binding energy and recombination lifetime of free exciton (FX) and donor-bound exciton (I_2) have been determined previously in undoped AlN epilayer [81]. A photoluminescence (PL) study on Si-doped AlN has found that the I_2 transition to be the dominant emission line at low temperatures [82]. We also have studied transition lines involving Mg in AlN from which energy level of Mg impurity in AlN was obtained [27]. However,

excitonic transitions in Mg-doped AlN were not observed and the dominant transitions were donor-acceptor pair (DAP) type involving Mg acceptors and two donors, one shallow and another deep. Significant improvement in material quality of Al-rich Si- and Mg-doped $Al_xGa_{1-x}N$ alloys allowed us to investigate the fundamentally important optical processes as well as basic parameters in $Al_xGa_{1-x}N$ alloys with high x [27,79-82].

Due to high insulating nature of Mg-doped Al-rich $Al_xGa_{1-x}N$ alloys, PL is proven to be a powerful characterization method to study optical properties of these materials. Understanding optical properties not only helps to characterize materials but also is very useful to probe their fundamental properties. In this work, optical studies of Mg-doped AlN epilayers has been carried out by deep UV time-resolved PL. Recombination lifetime and binding energy of the neutral acceptor-bound exciton (I_1) transition in Mg-doped AlN have been measured. The measured values in AlN are compared with those in Mg-doped GaN. We also measured the decay lifetimes of impurity transitions in Mg-doped AlN epilayers.

The 1 μm thick Mg-doped AlN epilayers were grown by MOCVD on sapphire (0001) substrates with low temperature AlN nucleation layers [27]. Trimethylaluminum (TMAl) and blue ammonia (NH_3) were used as Al and N sources. For Mg doping, bis-cylopentadienylmagnesium (Cp_2Mg) was used as Mg source. Secondary ion mass spectroscopy measurements (performed by Charles Evans & Associates) revealed that Mg-dopant concentration was about 6×10^{18} cm^{-3} in Mg-doped AlN epilayer. Atomic force microscope (AFM) and scanning electron microscope (SEM) were used to characterize the surface morphology of these epilayers. Structural characterization was done with x-ray diffraction (XRD) measurement. Full width at half maximum (FWHM) of XRD rocking curve of (0002) peak of as-grown AlN epilayers was between 50 to 300 arcsec. Deep UV time-resolved PL

spectroscopy was employed to investigate the sample. The PL system consists of a frequency quadrupled 100 femtosecond Ti:sapphire laser with an average power of 3 mW with excitation photon energy set at 6.28 eV (repetition rate of 76 MHz), a monochromator (1.3 m), and a streak camera with a detection capability ranging from 185 – 800 nm and a time resolution of 2 ps [28].
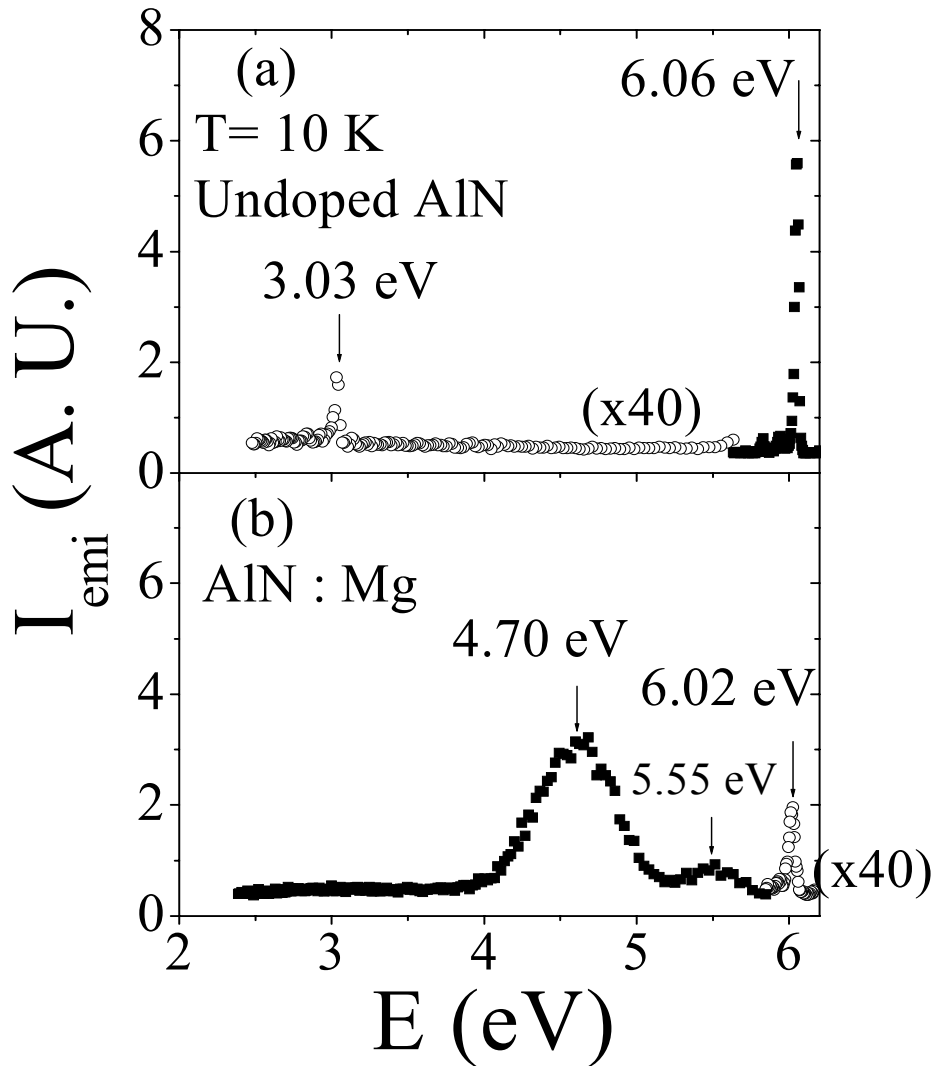
Fig. 3.13 PL spectra of (a) undoped AlN and (b) Mg-dope Mg-doped AlN epilayer measured at 10 K which covers a broad spectral range from 2.4 to 6.2 eV. Mg-doped AlN has two broad impurity emission lines at 4.70 and 5.55 eV.

Figure 3.13 shows the low temperature (10 K) PL spectra of (a) undoped and (b) Mg-doped AlN epilayers covering a broad spectral range from 2.4 to 6.2 eV. The arrows indicate the peak positions of the spectra. The undoped AlN epilayers exhibit a strong band-edge emission line at 6.06 eV due to FX transition and its second order at 3.03 eV due to grating of the monochromator, however Mg-doped AlN has two broad and intense impurity emission lines at 4.70 and 5.55 eV and a weak bandedge transition at 6.02 eV. Impurity transition at 4.7 eV is several orders stronger than the bandedge transition in Mg-doped AlN. It was observed that the optical and electrical quality of Mg-doped AlN depends strongly on the growth conditions.

Figure 3.14 compares the low temperature (10 K) PL spectra of (a) undoped and (b) Mg-doped AlN epilayers in the smaller spectral range. The undoped AlN epilayers exhibit a strong band-edge emission line at 6.06 eV due to FX transition and its longitudinal optical (LO) phonon replica at 5.95 eV (1 LO) and 5.84 eV (2 LO), with LO phonon energy of 110 meV. As undoped GaN is n-type, the neutral donor-bound exciton (I_2) transition is often dominant at low temperatures. However, undoped AlN is highly insulating due partly to the presence of native defects, such as Al vacancy or vacancy complex, which are deep acceptors and act as compensating centers for electrons. Thus, in undoped AlN, there is either very low concentration of neutral donor; D^0 (if $D^0 > A^0$) or no D^0 at all (if $D^0 < A^0$) at low temperatures and FX would be dominant due to large binding energy of FX.

For the Mg-doped AlN epilayer, the new emission line with a peak position at 6.02 eV is evident, which is attributed to excitons bound to the neutral Mg acceptor impurities (A^0,X) or I_1 line in AlN. With Mg doping, the I_1 transition is expected to be dominant instead of FX, which is consistent with the results. The intensity of this new emission line is about 50 times smaller than that of FX transition in undoped epilayer. The new emission line in Mg-doped AlN is 40

meV below the FX transition in undoped AlN, which corresponds to the binding energy, $E_{bx,}$ of the I_1 transition in AlN. This value is about two times larger than that of I_1 in Mg doped GaN [E_{bx}(GaN) = 20.0 - 21.5 meV] [83]. Mg-doped AlN epilayers were thermally annealed in nitrogen ambient up to 1325°C; however, the peak position of the I_1 transition is almost the same when compared with as-grown samples.
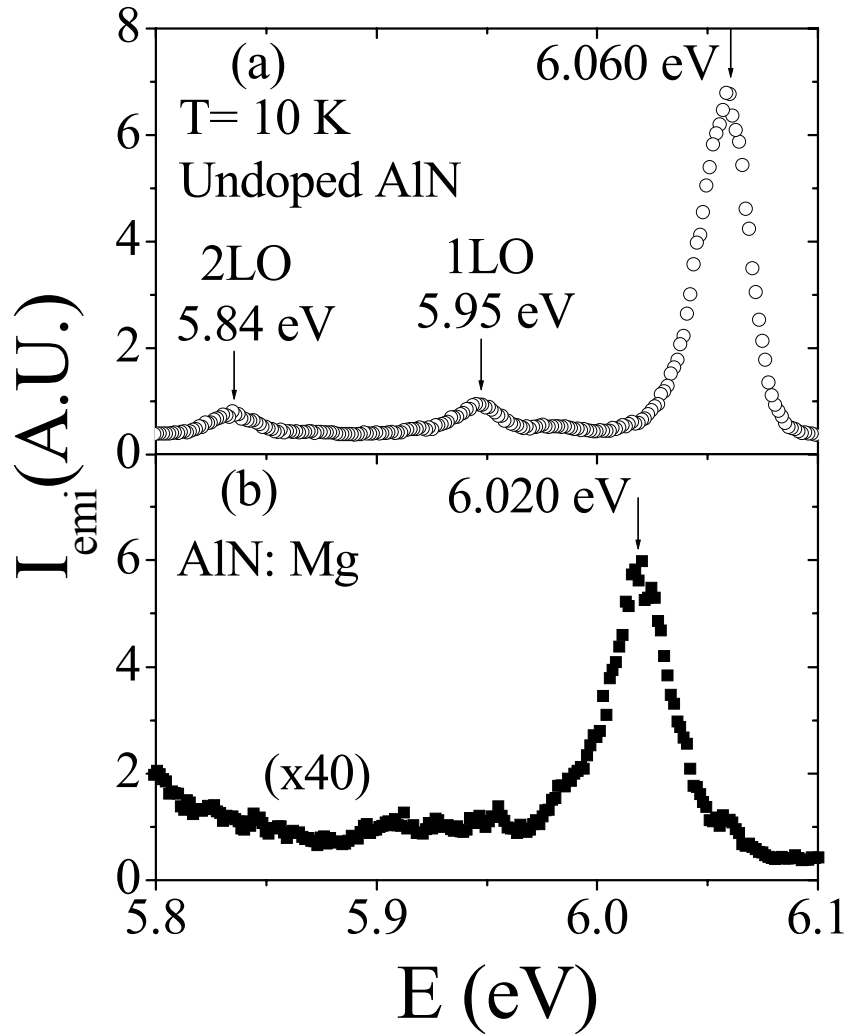
Fig. 3.14 PL spectra of (a) undoped AlN and (b) Mg-doped AlN epilayer measured at 10 K in the small spectral range. For the Mg-doped AlN epilayer, the transition at 6.06 eV disappears and a new emission line at 6.02 eV appears.
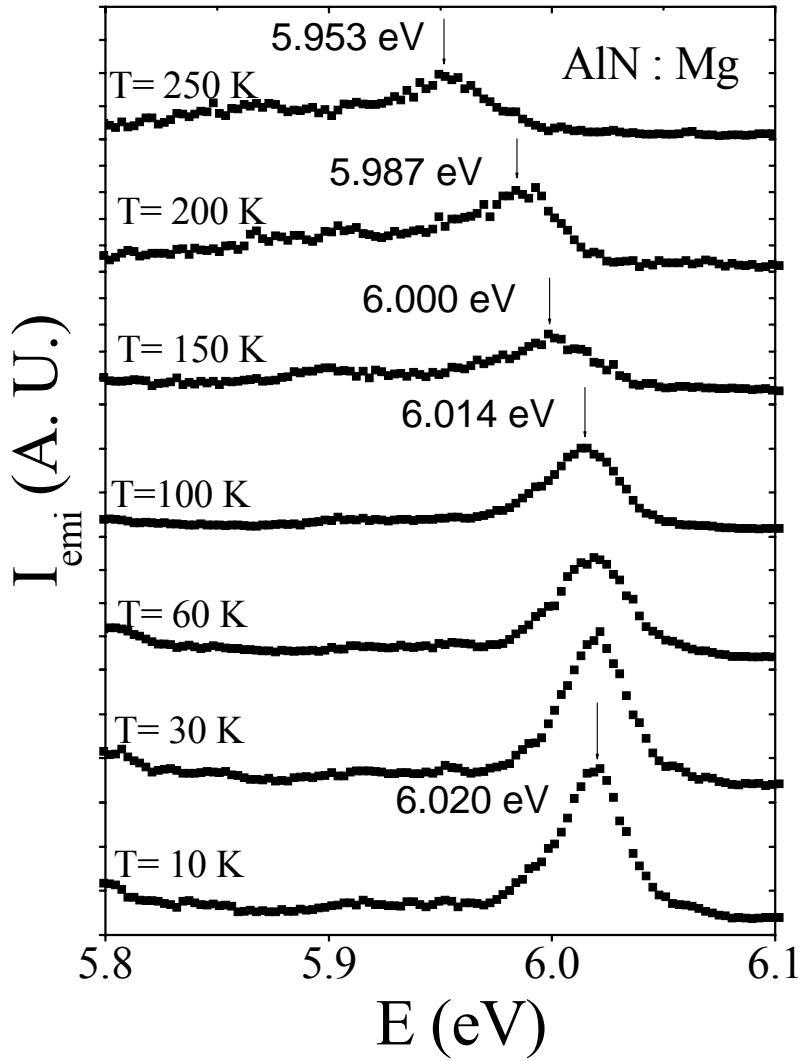
Fig. 3.15 PL spectra of Mg-doped AlN epilayer measured from 10 to 250 K.

The temperature evolution of the 6.02 eV emission line in the Mg-doped AlN epilayer measured from 10 to 250 K is shown in Fig. 3.15. The intensity decreases monotonically and the spectral peak position of this emission line is redshifted with increasing temperature. The thermal

quenching of the I_1 transition is due to dissociation of neutral acceptor-bound exciton described by

$$(A^0,X) \longrightarrow A^0 + X, \qquad\qquad (3.10)$$
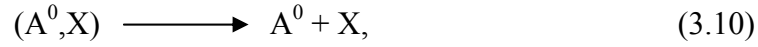
where A^0 and X are neutral acceptor and free exciton, respectively.
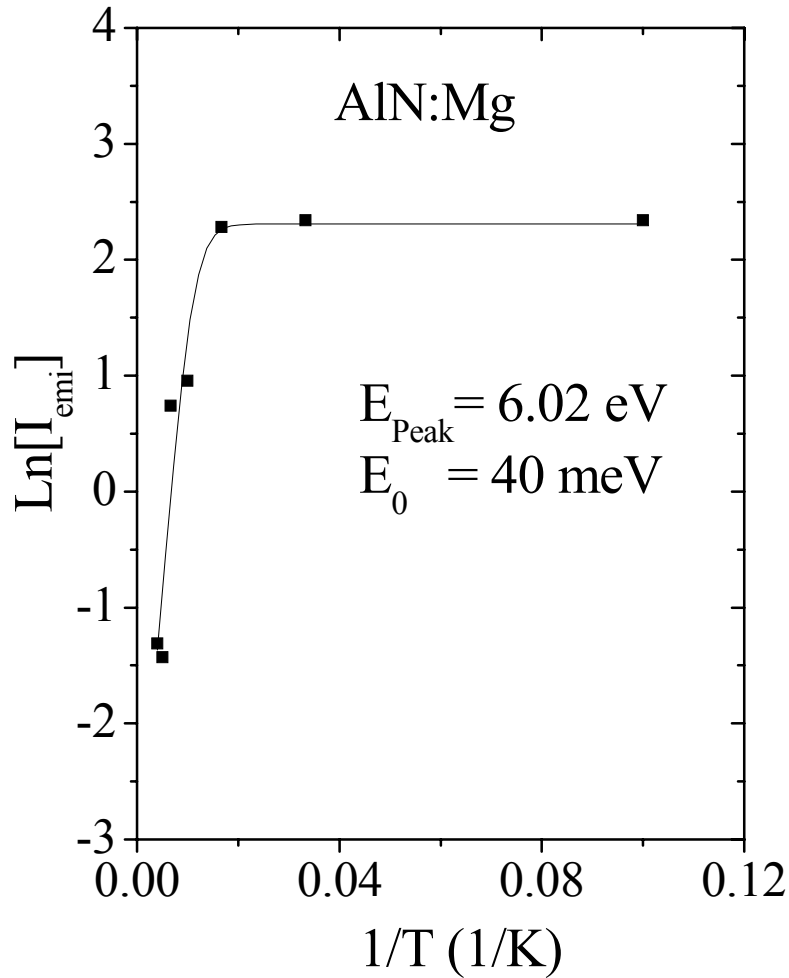
Fig. 3.16 The Arrhenius plot of the integrated PL emission intensity at 6.02 eV (10 K) between 10 and 250 K. The solid line is the least squares fit of data with Eq. (2). The fitted vale of the activation energy (E_0) is also indicated.

Figure 3.16 shows the Arrhenius plot of the PL intensity of the 6.02 eV emission line for the temperature range between 10 and 250 K. The solid line is the least-squares fit of the data with equation,

$$I_{emi} = \frac{I_0}{1 + c\,e^{-E_0/KT}}, \qquad (3.11)$$

where E_0 is the activation energy and c is the constant. The fitted value of E_0 is 40 meV and is consistent with the value obtained from the difference between the peak position of FX in undoped AlN and the I_1 peak position in Mg-doped AlN epilayers. This value of activation energy is in a rough agreement with Haynes' rule; for Mg-doped AlN the binding energy of the exciton-neutral-impurity complex is about 10% of the impurity binding energy if we neglect the central-cell correction [84]. Using Haynes' rule, the expected energy level of Mg impurity in AlN is 400 meV, which is close to our reported value of 500 meV [27]. The binding energy of 20 meV for the I_1 transition in Mg-doped GaN is also roughly about 10% of the energy level for Mg impurity (~ 170 meV).

Time-resolved PL was employed to measure the recombination lifetime of the I_1 transition at 6.02 eV, which is shown in Fig. 3.17. The measurement reveals that the decay kinetics was a single exponential with a decay lifetime constant of about 130 ps at 10 K, which is about three to five times smaller than the PL decay lifetime of the I_1 transition in GaN (370 - 660 ps) [83].

The relation between the oscillator strength of the impurity-bound exciton (F) and the free excitons (F_{eX}) is [85]

$$F = \left(E_1/E_{bx}\right)^{\frac{3}{2}} F_{eX}, \qquad (3.12)$$

where E_{bx} is the binding energy of the impurity-bound excitons, $E_1 = (2\hbar^2 / m)(\pi / \Omega_0)^{2/3}$, m is the effective mass of the FX, and Ω_0 is the volume of the unit cell. From Eq. (3.12), we thus have the ratio of radiative decay lifetime of I_1 and I_2 transitions as
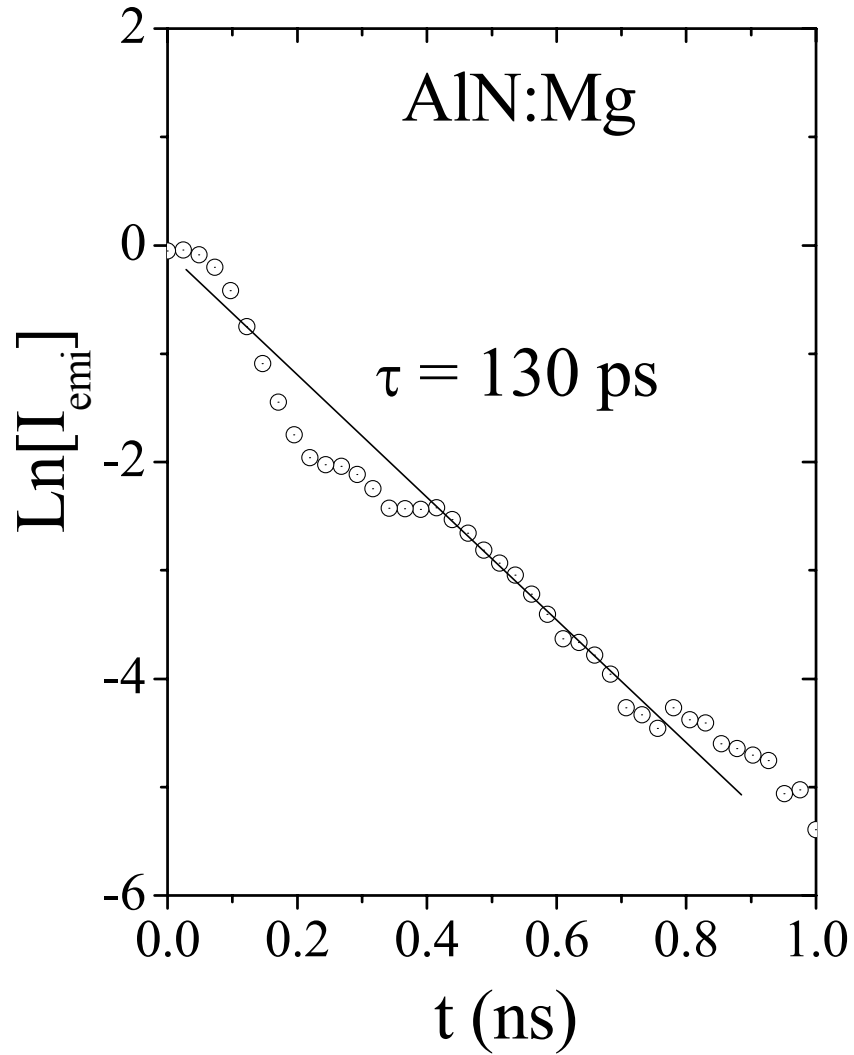
Fig. 3.17 Temporal response of the I_1 transition in Mg-doped AlN epilayer measured at 10 K. Observed recombination lifetime is 130 ps.

$$\tau(I_1)/\tau(I_2) = F(I_2)/F(I_1) = \left(E_{bx}(I_1)/E_{bx}(I_2)\right)^{\frac{3}{2}}, \qquad (3.13)$$

From Eq. (3.13), the ratio $\tau(I_1)/\tau(I_2) = 3.9$ is obtained by using the binding energy of I_1 and I_2 transitions in AlN as 40 and 16 meV [81], respectively. The decay lifetime of the I_2 transition in Si-doped AlN decreases from 80 to about 40 ps with increasing Si concentration (N_{Si}) from 1.5×10^{17} to 1.5×10^{18} cm^{-3} [82]. If we use 80 (40) ps as the decay lifetime for the I_2 transition in Si-doped AlN, we get the expected lifetime of 312 (158) ps for the I_1 transition in Mg-doped AlN, which is in reasonable agreement with the observed value of 130 ps. The trend of increased decay lifetime with increased binding energy is also clearly demonstrated.

Temporal response of the 5.55 and 4.7 eV emission peaks in Mg-doped AlN epilayer measured at 10 K is shown in Fig. 3.18. Decay lifetime of 5.55 eV peak is two exponential while 4.7 eV peak has a very long decay lifetime. The emission peak at 5.55 eV has been assigned to the free electrons to the neutral Mg level transition [86]. Observed two exponential decay of 5.55 eV peak with one very short lifetime and another very long lifetime supports this assignment. Very long (`> 1μm) decay lifetime of 4.70 eV peak in Mg-doped AlN indicates that it is DAP type transition involving deep donor and neutral magnesium, which is consistent with our previous results [27,86]. We previously attributed the 4.70 eV peak to be the transition from nitrogen vacancy with positive three-charge state (V_N^{3+}) to the neutral magnesium level [86]. Suppressing the 4.70 eV emission peak and increasing the intensity of I_1 transition improves the optical and electrical quality of the Mg-doped AlGaN alloys. Conductive Al-rich Al$_x$Ga$_{1-x}$N alloy of x = 0.7 has been obtained by suppressing V_N^{3+} related transition [79]. Time-resolved PL has

been used as a characterization tool to characterize and hence improve Mg-doped AlN epilayers

and the resistivity of about (1 - 5) x 10^3 Ωcm was measured at room temperature [86].
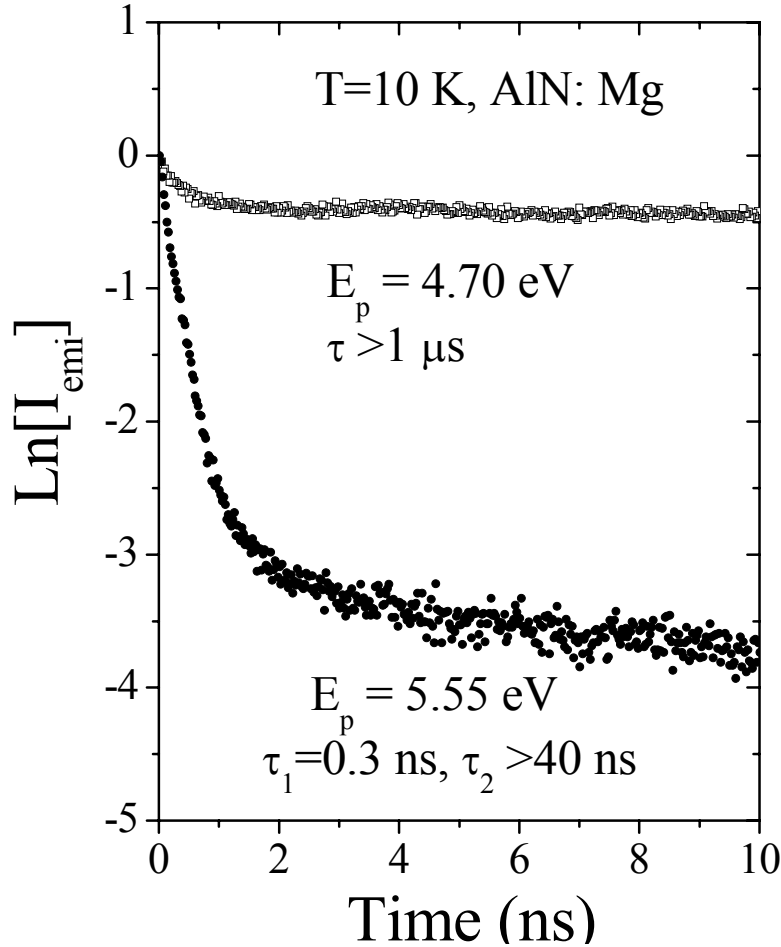
Fig. 3.18 Temporal response of the 5.55 eV and 4.7 eV emission peaks in Mg-doped AlN epilayer measured at 10 K. $\tau >1$ μs for E_p = 4.70 eV and lifetime of 5.55 eV emission peak is two-exponential.

Temporal response of the I_1 transition in Mg-doped AlN epilayer under two different excitation intensities is shown in Fig. 3.19. In Fig. 3.20 we plot the decay lifetimes of the I_1 transition as a function of relative excitation intensity I_{exc} measured at 10 K. The lifetime

decreases as the I_{exc} increases. We attribute the observed behavior to the exciton–exciton interaction, under high exciton densities. The radiative quantum efficiency η is given by

$$\eta = \frac{1}{1 + \dfrac{\tau_r}{\tau_n}} \qquad (3.14)$$

where τ_r and τ_n are the radiative and non radiative recombination lifetimes, respectively. Our results show that η is enhanced under the influence of the exciton-exciton interaction through decreasing τ_r with I_{exc} and the PL quantum yield increases superlinearly with I_{exc} in Mg-doped AlN. Similar results have been observed for FX transition in GaN [87,88]. At the lowest I_{exc}, the recombination lifetime of I_1 transition in Mg-doped AlN is about 172 ps.
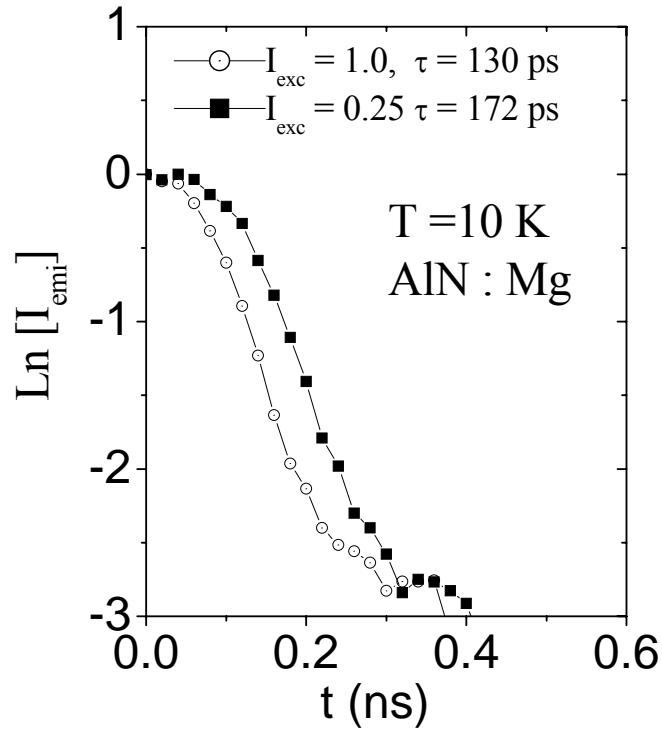
Fig. 3.19 Temporal responses of the I_1 transition measured at two representative excitation intensities for I_{exc} =1 and 0.25 (normalized).
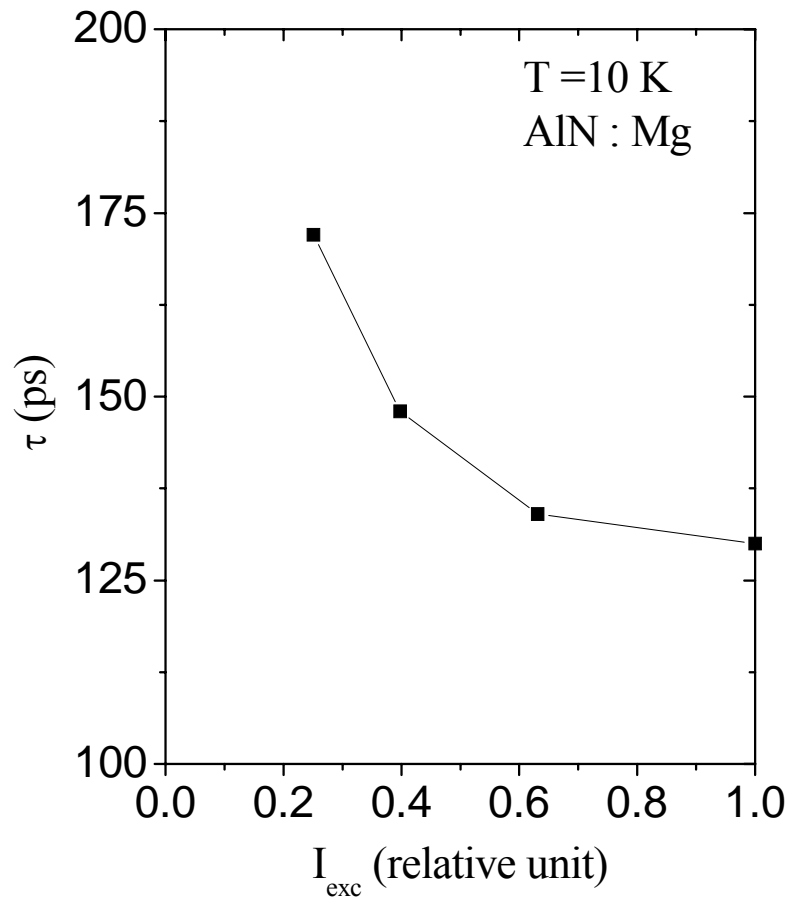
Fig. 3.20 Excitation intensity, I_{exc} dependence (normalized) of the recombination lifetimes of the I_1 transition in Mg-doped AlN.

Table I displays the binding energy and decay lifetime of FX, I_1, and I_2 transitions in AlN and GaN epilayer. The table summarizes the results of this work and a survey of references [20,25,3581-83,89,90]. Energy levels of Mg acceptor and Si donor in AlN and GaN are also listed. All parameters in AlN are almost a factor of 2-3 times larger than that in GaN. Decay lifetimes of excitonic transitions in AlN are smaller compared to GaN due to large bandgap and increased effective masses of electrons and holes.

Table I Binding energy (in meV) and decay lifetime (in ps) of the fundamental transitions as well as energy levels (in meV) of Si donor and Mg acceptor impurities in AlN and GaN.

	E_{FX}	$E_{BX}(I_1)$	$E_{BX}(I_2)$	E_A	E_D	τ_{FX}	$\tau(I_1)$	$\tau(I_2)$
GaN	20-25	20-21	6-7	160-180	25-29	50-350	370-660	35-100
AlN	80	**40**	16	500	80 -250	50	**130**	80
AlN/GaN	3.6-4.0	2.0	2.6	3.1	3.2 – 8.6	1.0-0.1	0.4-0.2	2.3-0.8

MOCVD grown Mg-doped AlN epilayers have been studied by deep UV time-resolved PL spectroscopy. An emission line at 6.02 eV has been observed, which was absent in undoped AlN epilayers and is 40 meV below the FX transition in undoped AlN. This emission line is due to the recombination of the exciton bound to neutral Mg acceptor in AlN. This assignment has been confirmed by the time-resolved measurement at 10 K and the temperature dependence of the PL intensities. Measured binding energy of exciton bound to Mg impurity in AlN is 40 meV that is twice as that in GaN, as expected with larger effective masses of electrons and holes in AlN than in GaN. The observed large acceptor-bound exciton binding energy implies that excitons in AlN are extremely robust entities. The measured PL decay lifetime of the I_1 transition in Mg-doped AlN is 130 ps. The decay lifetime increases with decreasing excitation intensity, which indicates that the PL quantum yield increases with increasing excitation intensity.

3.5 Growth and photoluminescence studies of Zn-doped AlN epilayers

AlN is emerging as an active semiconductor material due to the recent development of high quality AlN epilayer growth on sapphire, SiC, and AlN bulk substrates. Because of its large direct band gap (~ 6.1 eV), AlN can be used for the development of optoelectronic devices operating from 200 – 350 nm by alloying with GaN. A recent demonstration of an AlN light emitting diode (LED) with emission wavelength at 210 nm has shown its high potential for obtaining optoelectronic devices active in the ultraviolet C-band (UVC) spectral range [16]. Potential applications of compact light sources and detectors operating in the UVC spectral region range from sterilization, bio-agent detection, and acoustic sound wave (SAW) devices, to x-ray detectors [18,19, 43, 91].

For the applications of AlN as an active material, conductive n- and p-type materials are required. While n-type AlN epilayers with reasonable conductivities have been achieved by Si-doping [20-23], p-type conductivity is extremely difficult to obtain due to the large activation energy of Mg acceptors. GaN with p-type conductivity can be reproducibly grown by metal-organic chemical vapor deposition (MOCVD) by Mg-doping and subsequent annealing [92]. The activation energy of Mg is about 160 meV in GaN, increases with Al content in AlGaN alloys, and is about 0.51 eV in AlN [24-27]. Zn elements have been previously utilized as p-type dopants in GaN [93], which, however, rendered semi-insulating materials. The binding energy of Zn in GaN is about 0.34 eV, as determined by optical measurements [4,93,94,]. A previous calculation predicted that Zn occupies Al site in AlN and the activation energy of Zn acceptor in AlN is in the range of 0.22 – 0.44 eV [95], which is significantly smaller than that of Mg in AlN. Since the free hole concentration increases exponentially with a decrease of the acceptor activation energy, any strategies that have the potential to reduce the activation energies

of acceptors in AlN are worth pursuing. In this work, the growth and photoluminescence (PL) studies of Zn-doped AlN epilayers has been presented.

Zn-doped AlN epilayers of thickness ~ 1 μm were grown by MOCVD. Prior to the growth of Zn doped layer, a 0.5 μm thick undoped AlN epilayer was first grown on sapphire substrate as a template, and was then followed by the growth of Zn-doped AlN. Trimethyl aluminum (TMAl) and blue ammonia were used as aluminum and nitrogen sources, respectively. Dimethyl zinc (DMZn) was used as Zn source. The Zn dopant concentration was on the order of 10^{20}cm^{-3} as determined by secondary ion mass spectrometry (SIMS) measurement. The growth temperature and pressure were 1200°C and 40 torr, respectively. The samples were characterized by atomic force microscope (AFM) and x-ray diffraction (XRD).   Hall-effect measurements were attempted to measure the conductivity of Zn-doped AlN epilayers. However, as-grown epilayers were highly resistive. Furthermore, subsequent post growth annealing of Zn-doped AlN in nitrogen ambient did not result in p-type conduction. Deep UV PL spectroscopy was employed to study the optical properties of Zn-doped AlN. Our PL system consists of a frequency quadrupled 100 femtosecond Ti: sapphire laser with an average power of about 3 mW at 197 nm (repetition rate of 76 MHz), a monochromator (1.3 m), and a streak camera with a detection capability ranging from 185 – 800 nm and a time resolution of 2 ps [28].

Low temperature (10 K) PL spectra of Zn- and Mg-doped AlN and undoped AlN epilayers are shown in Fig. 3.21. The PL spectrum of undoped AlN exhibits a strong band-edge emission at 6.06 eV due to the free exciton transition (FX) [96] and virtually no impurity transitions. Since FX binding energy in AlN is around 0.08 eV [38,81], the bandgap of AlN at 10 K is thus around 6.14 eV ($\approx$ 6.06 eV + 0.08 eV). The PL spectrum of Mg doped AlN comprises a band edge transition at 6.02 eV due to the recombination of excitons bound to

neutral Mg acceptors (I_1 transition). Two additional impurity emission lines at 4.70 and 5.54 eV in Mg doped AlN are also observable and believed to be donor-acceptor-pair (DAP) transitions involving two different donors (deep and shallow level donors) and Mg acceptor [27]. The deep level donors participated in the 4.70 eV transition in Mg doped AlN were identified as nitrogen vacancies with three positive charges (V_N^{3+}) that act as compensating centers for p-type doping [97].

Compared to the PL spectrum of Mg doped AlN, the PL spectrum of Zn-doped AlN has a very similar line shape, however, with the two impurity transitions red shifted to 4.50 and 5.40 eV (with respect to 4.70 and 5.54 eV in Mg doped AlN).   The band edge emission line at 6.01 eV in Zn doped AlN can be indisputably assigned to the recombination of excitons bound to neutral Zn acceptors (I_1 transition).   The measured recombination lifetime of the 4.50 eV emission line is rather long (~1 μs) and is comparable to that of the 4.70 eV line in Mg doped AlN. Based on the assignment of the 4.70 eV emission line in Mg doped AlN, we assign the emission line at 4.50 eV in Zn-doped AlN to a DAP transition of electrons bounded to nitrogen vacancies with three positive charges (V_N^{3+}) to neutral Zn acceptors, which is consistent with the measured long recombination lifetime. The binding energy of V_N^{3+} in AlN has been calculated to be about 0.9 eV [98], from which an energy level for Zn acceptors in AlN is thus deduced to be about 0.74 eV ($E_A \approx$ 6.14 eV - 4.50 eV - 0.90 eV = 0.74 eV) with neglecting Coulomb interactions between the ionized acceptors and donors.
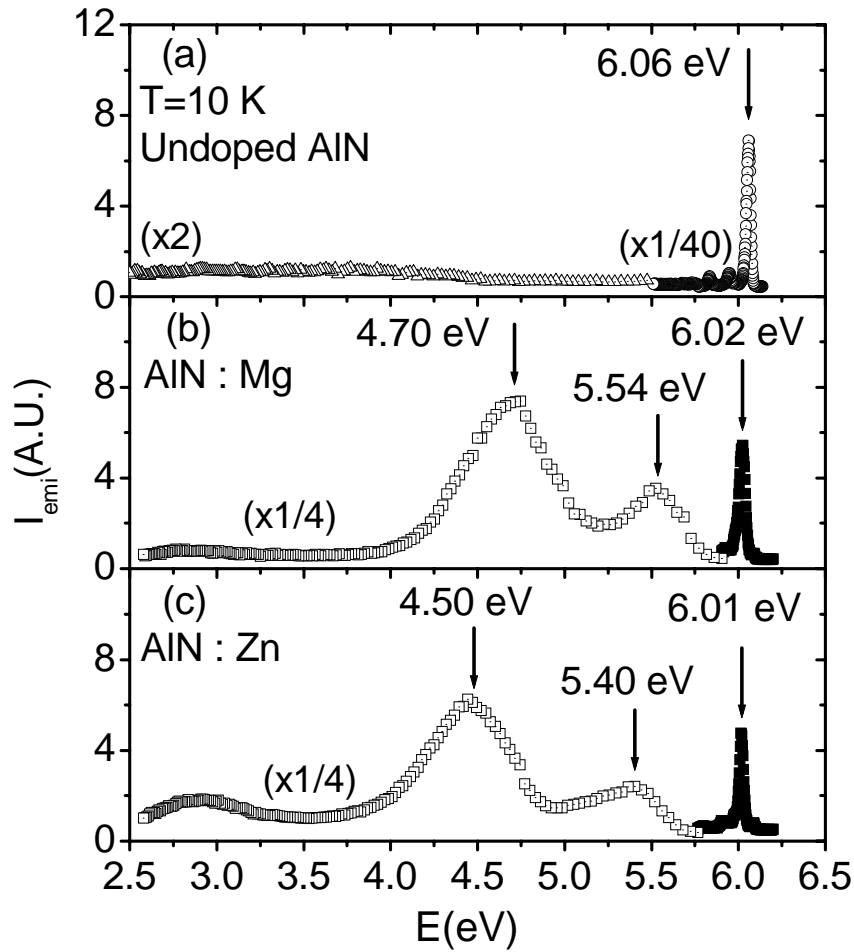
Fig. 3.21 PL spectra of (a) undoped, (b) Mg-doped, and (c) Zn-doped AlN epilayers measured at 10 K. For the Mg- (Zn-) doped AlN epilayers, the band edge transition at 6.06 eV disappears and a new band edge emission line is observed at 6.02 (6.01) eV. Additional impurity emission lines observed in Mg- (Zn-) doped AlN at 4.70 (4.50) and 5.54 (5.40) eV are related with Mg (Zn) acceptor impurities.
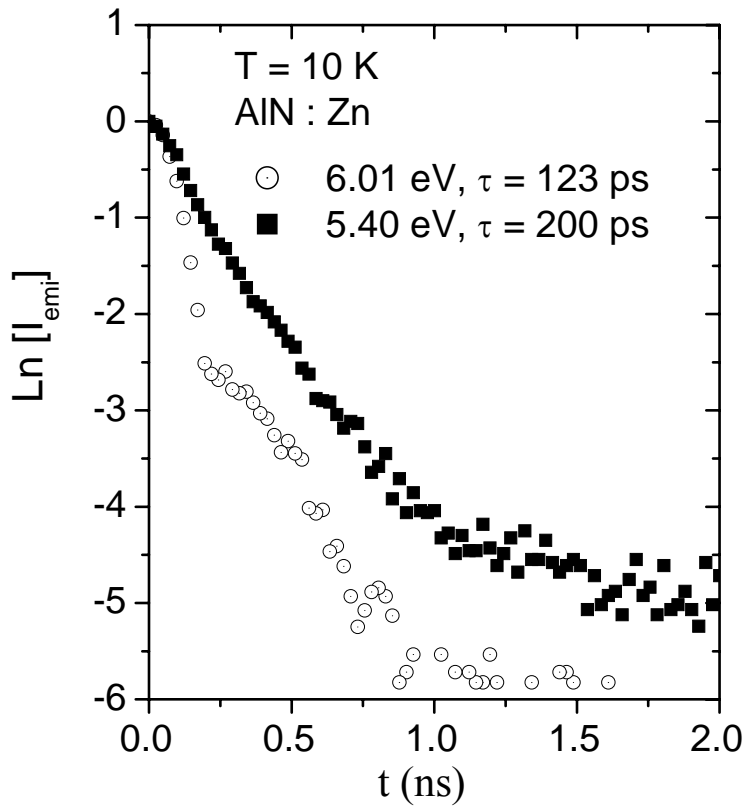
Fig. 3.22 Temporal responses of the I_1 and 5.40 eV emission lines in Zn-doped AlN epilayers measured at 10 K.

Figure 3.22 shows the temporal responses of the I_1 transition at 6.01 eV and the impurity transition at 5.40 eV in Zn-doped AlN epilayer measured at 10 K, which revealed a roughly single exponential decay kinetics with a decay time constant of about 123 ps for the I_1 transition and 200 ps for the 5.40 eV impurity transition. The measured decay time constant of I_1 is comparable to a value of 130 ps observed in Mg doped AlN [96]. The recombination lifetime of 200 ps observed for the 5.40 eV emission line in Zn doped AlN is rather short, which seems to suggest that it is of a band-to-impurity type of transition. Based on this, we assign the 5.40 eV emission peak to the transition of free electrons to neutral Zn acceptors (Zn^0), although a DAP

type of transition involving shallow donors and Zn^0 cannot be totally precluded. This assignment provides an energy level of Zn acceptors in AlN to be $E_A \approx 6.14$ eV - 5.40 eV = 0.74 eV, which agrees with the value deduced from the 4.50 eV emission line discussed above. It is worth noting that the identified origins of the two impurity transitions at 5.40 and 4.50 eV in Zn doped AlN provide identical activation energy of 0.74 eV for Zn acceptors in AlN, which offers confidence in our assignments. Our results thus point to that the energy level of Zn is about 0.23 eV deeper than that of Mg in AlN (0.51 eV). The energy levels related to Zn acceptors and corresponding transitions in AlN are shown in Fig. 3.23. Optically measured Zn level in GaN is also indicated in Fig. 3.23 [93,94].

CB

0.9 eV

1.84 eV (70%)

V_N^{3+}

0.39 eV V_N^{3+}

5.40 eV

6.14 eV

4.50 eV

3.50 eV

Zn^0

0.34 eV

Zn^0

0.79 eV (30%)

Mg^0

0.51 eV

0.74 eV

VB

GaN   AlN
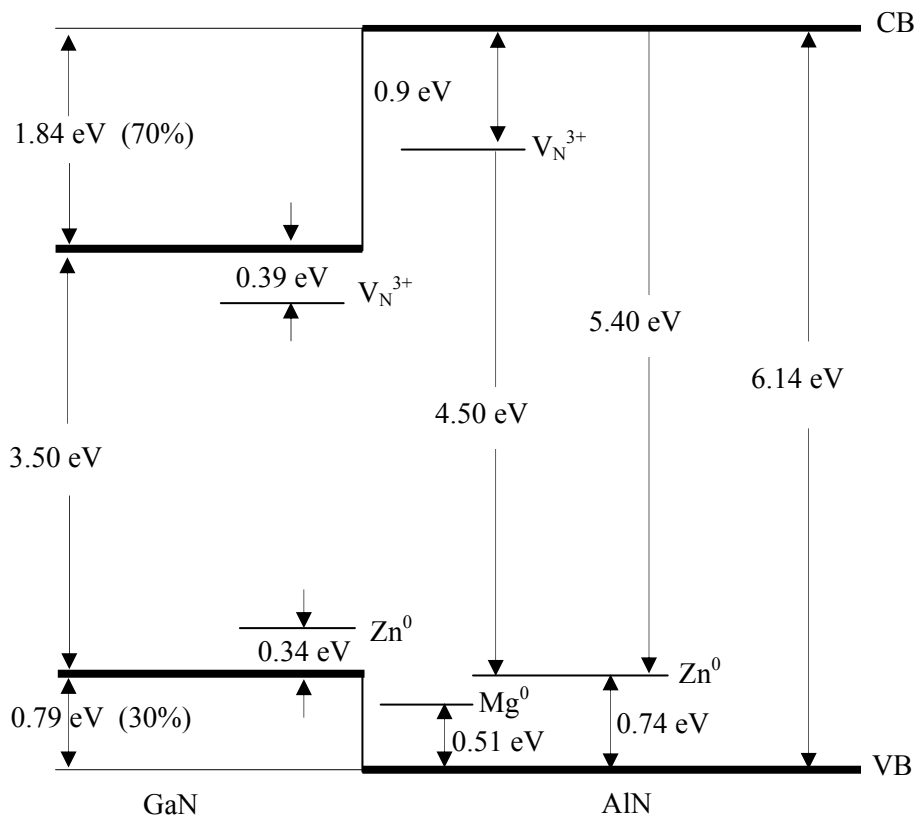
Fig. 3.23 Energy diagram showing the energy levels of Mg and Zn acceptors in AlN. Zn energy level in GaN is also included.

80
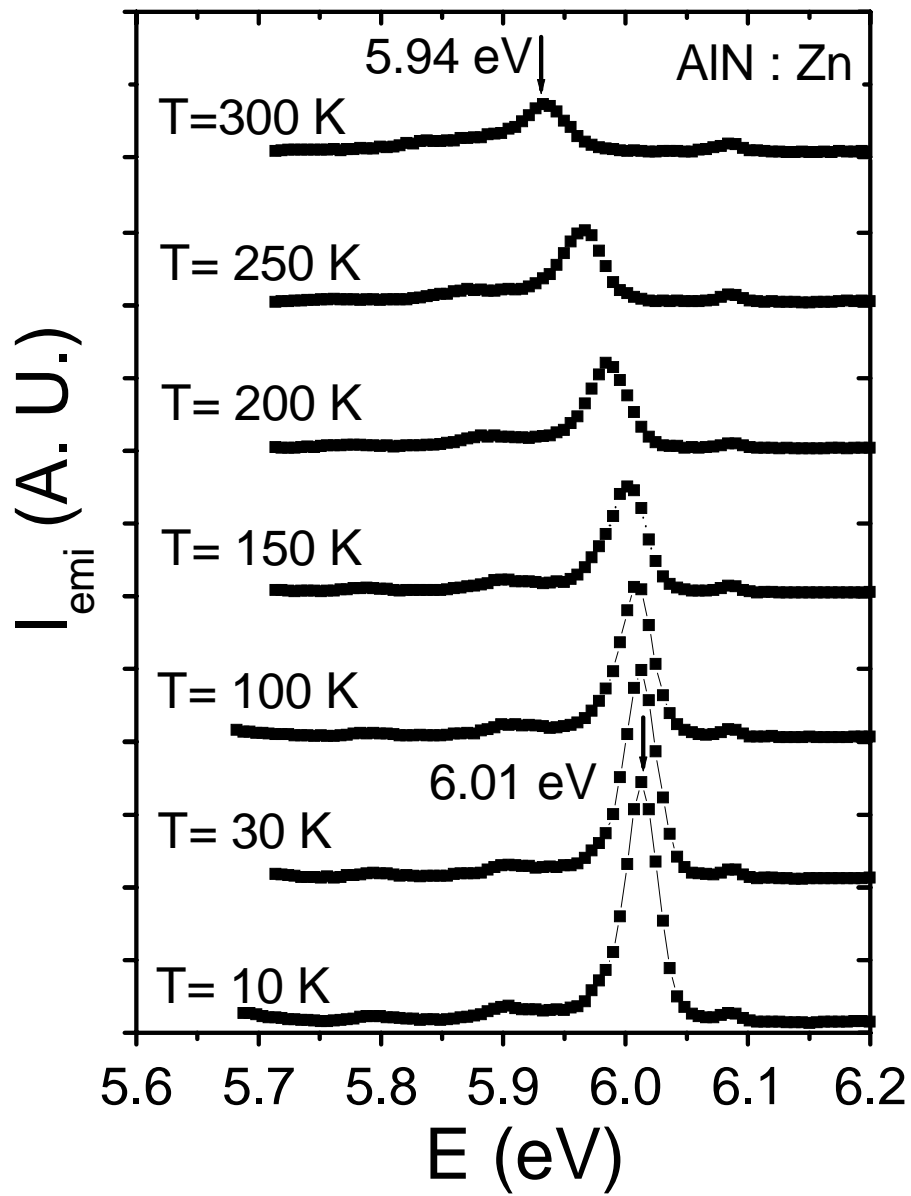
Fig. 3.24 The temperature evolution of PL spectra of Zn-doped AlN epilayer measured from 10 to 300 K.
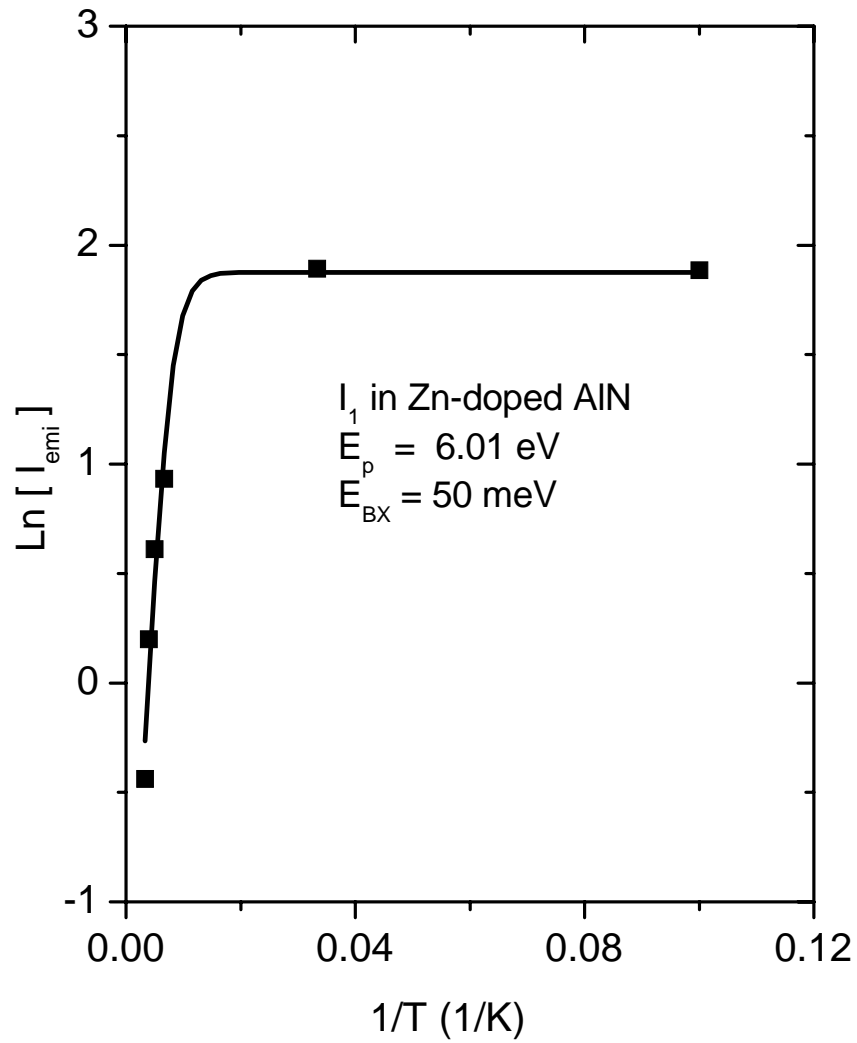
Fig. 3.25 The Arrhenius plot of the integrated PL emission intensity of the I_1 emission peak in Zn-doped AlN between 10 and 300 K. The solid line is the least squares fit of data with Eq. (3.11). The fitted value of the binding energy of neutral acceptor bound exciton, I_1, (E_{BX}) is also indicated.

To determine the binding energy of Zn acceptor-bound exciton in AlN, we have measured the temperature dependence of the I_1 emission intensity in Zn doped AlN and the result is shown in Fig. 3.24. The PL intensity (linewidth) decreases (increases) monotonically and the spectral peak position is red-shifted with increasing temperature. The thermal quenching of the I_1 transition is due to the dissociation of neutral acceptor-bound excitons in Zn-doped AlN. Figure 3.25 shows the Arrhenius plot of the PL intensity of the I_1 emission line in Zn doped AlN for the temperature range between 10 and 300 K. The solid line is the least-squares fit of the data with equation 3.11. The fitted value of binding energy is 50 meV and is consistent with the value obtained from the difference between the spectral peak positions of FX in undoped AlN and I_1 in Zn-doped AlN epilayers (6.06 eV − 6.01 eV = 0.05 eV). Experimentally measured binding energy of neutral Mg acceptor bound excitons in AlN is about 0.04 eV [96]. From Haynes' rule [84], the larger E_{BX} value in Zn-doped AlN compared to that in Mg-doped AlN also hints a deeper energy level of Zn than Mg in AlN.

In summary, Zn-doped AlN epilayers were grown by MOCVD and their optical properties were probed by deep UV time-resolved PL. Zn related impurity transitions were observed at 5.40 and 4.50 eV in Zn-doped AlN, which are absent on undoped AlN layers. By comparing the PL spectra of Zn-, Mg-doped and undoped AlN epilayers, the energy level of Zn acceptor in AlN was deduced to be about 0.74 eV, which is about 0.23 eV deeper than Mg level in AlN. In contrary to a previous theoretical prediction, our results thus suggest that Zn is not a better candidate than Mg as a p-type dopant in AlN. More theoretical and experimental investigations are required to further understand doping issues in AlN, particularly pertaining p-type doping. Besides searching for suitable acceptor elements, innovative doping methods also need to be developed to bring a breakthrough in this field.

3. 6 Optical properties of the nitrogen vacancy in AlN epilayers

Aluminum nitride (AlN) has attracted much interest due to its applications in ultraviolet (UV) light emitters and other optoelectronic devices. It has high mechanical hardness, high thermal conductivity, large dielectric constant, and high resistance to harsh environments [78]. It may also be promising in the emerging field of spintronics, due to its predicted high curie temperature (T_C) when doped with particular transition metals [99,100]. For further applications of AlN, it is very important to understand its fundamental properties. For optoelectronic device applications based on AlN, understanding the properties of native defects and impurities is crucial; particularly their charge states and energy levels.

As-grown GaN is usually *n* type; however, as-grown AlN is highly resistive and *n*-type conductivity is very difficult to obtain. For many years, it was believed that nitrogen vacancies (VN) are the cause of the high background *n*-type conductivity in unintentionally doped GaN [101]. First principle calculations indicate that the isolated nitrogen vacancy in GaN has large formation energy and can be excluded as the source of *n*-type conductivity [102]. More recently, nitrogen vacancies have been observed in electron-irradiated GaN epilayers and the energy level of V_N in GaN was determined to be around 25 meV [103]. This is close to a value of 30 meV obtained from a tight-binding calculation [104] and is consistent with the value obtained from the effective-mass theory without central-cell correction [105]. While the properties of V_N in GaN are relatively well understood now, little is known about V_N in AlN. Previous theoretical investigation showed that V_N is a shallow donor with an energy level of about 300 meV [104]. While deep levels offer preferential recombination routes, they are frequently nonradiative and thus disadvantageous to luminescent devices.

In this work, deep UV photoluminescence (PL) results of cobalt (Co) implanted AlN epilayers has been presentd, from which the energy band diagram for the V_N levels in GaN and AlN has been deduced. The 1- μm-thick AlN epilayers were grown by metalorganic chemical vapor deposition (MOCVD) on sapphire (0001) substrates with low emperature AlN nucleation layers [80]. Trimethylaluminum and blue ammonia (NH3) were used as Al and nitrogen sources. Co^+ ions were implanted in AlN at an energy of 250 keV and with a fixed dose of $3x10^{16}$ cm^{-2} as described elsewhere [100] and Co-implanted AlN epilayers were then thermally annealed in nitrogen ambient at various temperatures up to 1325 °C for 15 min. Structural characterization was done through high-resolution x-ray diffraction (XRD) measurements. Full width at half maximum of XRD rocking curve of (0002) peak of the as-grown AlN epilayers was around 400 arc sec, which increased by about 30% for Co-implanted AlN epilayers, but the peak position didn't change. Deep UV PL spectroscopy was employed to investigate the optical properties of the Co-implanted samples. The PL system consists of a frequency quadrupled 100 fs Ti:sapphire laser having an average power of 3 mW. The excitation photon energy was set at 6.28 eV with a repetition rate of 76 MHz. A 1.3 m monochromator and a streak camera, with a detection capability ranging from 185 to 800 nm and a time resolution of 2 ps, were used [28].

Figure 3.26 compares the low temperature (10 K) PL spectra of (a) as-grown and (b) Co-implanted AlN epilayers. The arrows indicate the peak positions of the spectra. The asgrown epilayer exhibits a strong band edge emission line at 6.05 eV and its LO phonon replicas at 5.94 eV (1 LO) and 5.83 eV (2 LO) . For the Co-implanted AlN, the band edge transition at 6.05 eV is absent. However, an emission line with a peak position at 5.87 eV is evident. The spectral peak position and the intensity of the peak suggest that point defect recombination centers were created during ionimplantation. Furthermore, PL spectra of Mn and Crimplanted samples

(published in Ref. 100) were identical to that of the Co-implanted sample independent of the implanted species, which also suggests that the 5.87 eV emission line is not related with the Co ions, but to the defect recombination centers created during ion implantation. The band edge transition at 6.05 eV could not be recovered by thermal annealing in nitrogen ambient up to 1325 °C.
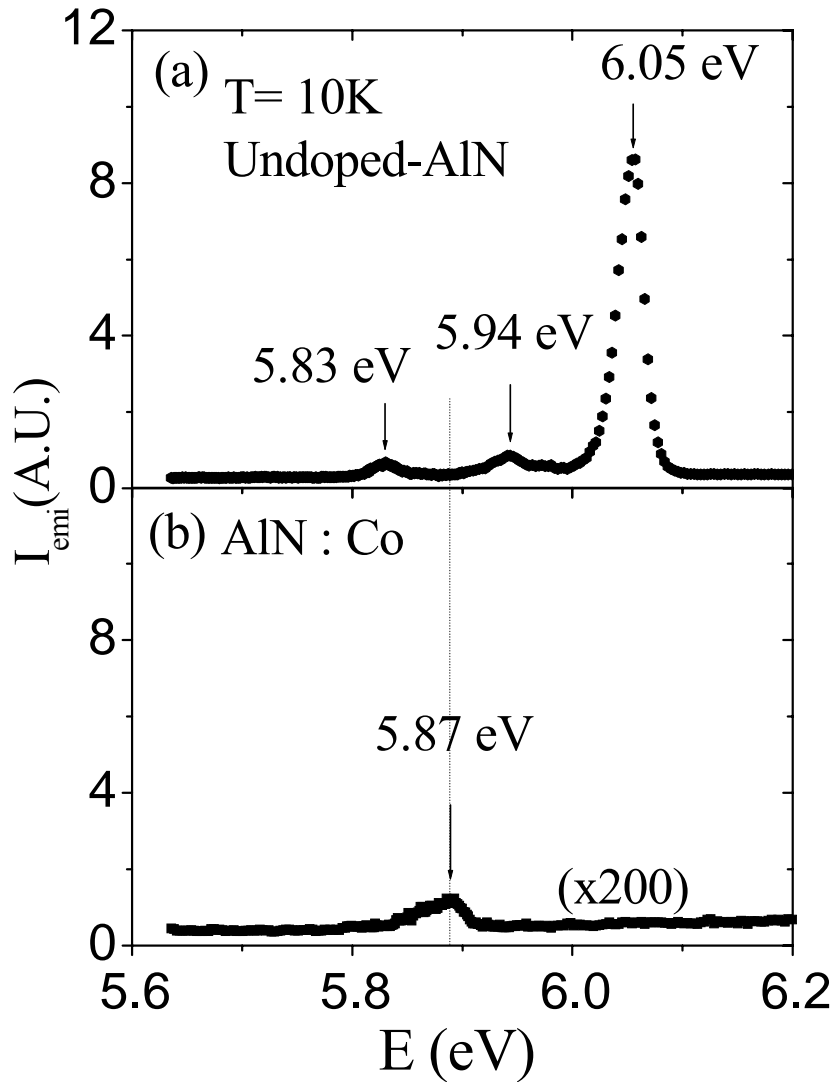
Fig. 3.26 PL spectra of (a) as-grown AlN and (b) ion-implanted AlN epilayer measured at 10 K. For the ion-implanted AlN epilayer, the band-edge transition at 6.05 eV disappears and a new emission line is observed at 5.87 eV.

Time-resolved PL was employed to measure the recombination lifetime of the 5.87 eV emission line. The measurement reveals that the decay kinetics was a single exponential with a very short decay time constant (<20 ps), which precludes the possibility for a donor-acceptor-pair (DAP) transition. Fast decay lifetime indicates that it is a band-toimpurity type rather than DAP type transition. For the band-to- impurity transitions, the decay rate is proportional to the total impurity (defect) concentration. Our experimental results thus indicate that the defect concentration is very high, which is consistent with the absence of the band edge transitions (6.05 eV) in ion-implanted samples. In general, ion implantation generates a large number of vacancies in the crystal. In GaN, high dose ion implantation is known to induce nitrogen vacancies that cannot be recovered completely by thermal annealing [106]. Since the Al vacancy (V_{Al}) is believed to be a deep acceptor with an energy level larger than 2 eV, [104] the possibility of V_{Al} being involved in the 5.87 eV PL emission can be precluded. We thus believe that Co ions with energy 250 keV only displace nitrogen atoms to generate nitrogen vacancies (V_N) in AlN. Antisites and N intersitials (N_i) are energetically less favorable due to the large lattice mismatch in the covalent radii of Al and N. Our results thus indicate that the 5.87 eV emission line is a band-to-impurity transition, involving electrons bound to V_N and free holes. As-grown AlN epilayers do not contain V_N because of the high formation energy of V_N in AlN [107]. Thus, the V_N related optical transition is absent.

Figure 3.27 shows the temperature dependence of the 5.87 eV emission line in the Co-implanted AlN measured from 10 to 250 K. The peak position changes slightly with temperature and in fact depicts a weak blueshift with increasing temperature in the range from 10 to 180 K. This further supports our assignment that the 5.87 eV emission line is a band-to-impurity transition, since the spectral peak position of this type of emission is expected to follow the

temperature variation of the band gap with an initial blueshift before thermal energy for impurity

ionization is reached. Above 170 K, the integrated PL intensity (Iint) of the 5.87 eV emission

line decreases with temperature rapidly and diminishes completely above 250 K, which based on

our assignment is predominantly due to the thermal activation process of V_N :

$$V_N^0 \underset{E_0}{\rightleftarrows} V_N^+ + e^-$$ (3.15)

where E_0 is the thermal activation energy.
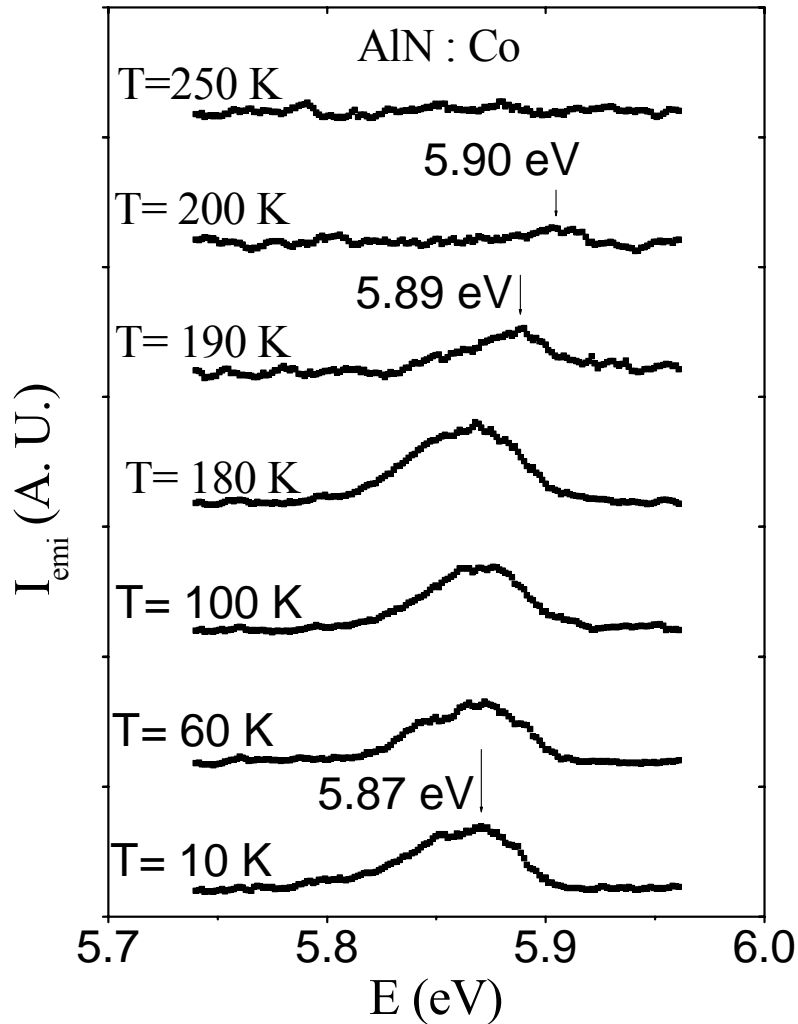
Fig. 3.27 PL spectra of cobalt implanted AlN epilayer measured from 10 to 250 K.

Figure 3.28 shows the Arrhenius plot of the PL intensity of the 5.87 eV emission line for the temperature range between 170 and 250 K. The solid line is the least squares fit of the data with equation (3.11). The fitted value of E_0 is 260 meV, which agrees quite well with the theoretically calculated energy level of V_N of 300 meV [104].
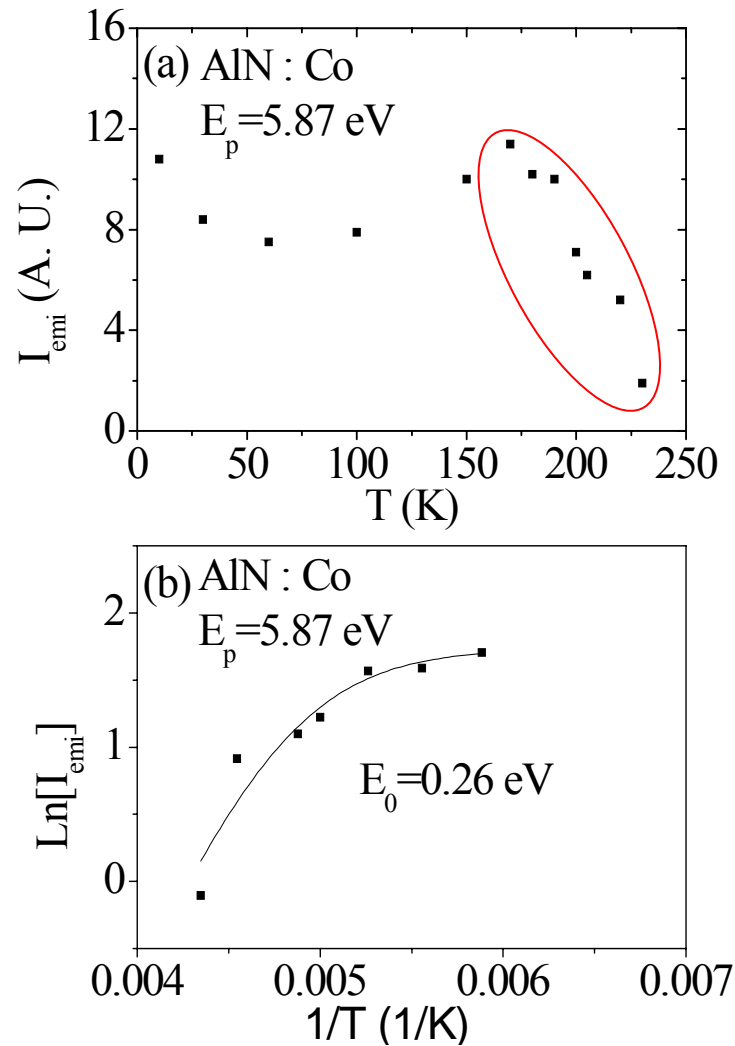
Fig. 3.28 (a) Integrated PL intensity of the 5.87 eV emission line for ion-implanted AlN measured at different temperatures from 10 to 250 K. (b) The Arrhenius plot of the integrated PL emission intensity at 5.87 eV between 170 and 230 K. The solid line is the least squares fit of data with Eq. (3.11). The fitted vale of activation energy (E_0) is also indicated.

Based on the PL results, we have constructed an energy band diagram in Fig. 3.29 for the V_N levels in GaN and AlN. For band alignment, a conduction-band-offset parameter of 70% between AlN and GaN was used [108] and the energy gap of GaN was taken as 3.50 eV. Since V_N is located at 5.87 eV with an energy level of 260 meV, the band gap of AlN can be deduced to be 5.87 eV+0.26 eV = 6.13 eV, which agrees well with a previous determination of 6.11 eV [81]. This, in turn, also supports our interpretation that the emission line at 5.87 eV in Co-implanted AlN is due to a band-to-impurity transition involving V_N. In contrast to GaN, the V_N in AlN cannot contribute to the n-type conductivity, as a consequence of the large activation energy.
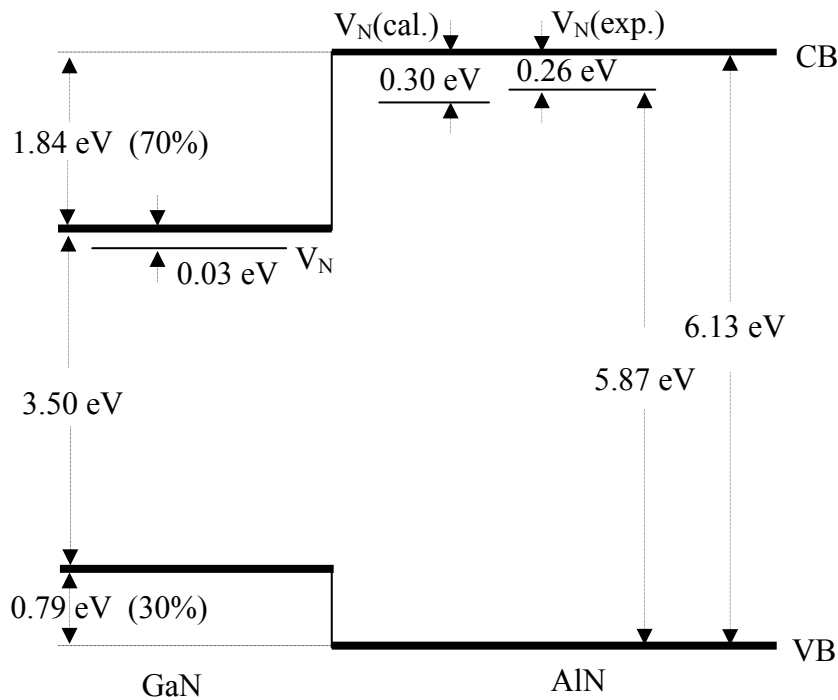
Fig. 3.29 The energy band diagram of AlN compared with GaN together with energy levels of V_N.

In summary, MOCVD grown AlN epilayers have been implanted with Co ions and studied by deep UV PL. An emission line at 5.87 eV has been observed, which was absent in as-grown AlN epilayers. This emission line has been attributed to a band-to-impurity transition between electrons bound to nitrogen vacancies and free holes. The experimentally determined nitrogen vacancy energy level is around 260 meV, which is in reasonable agreement with the calculated value of 300 meV. As a consequence of the large activation energy (0.26 eV) as well as high formation energy, V_N in AlN cannot contribute significantly to the n-type conductivity.

3.7 Higher lying conduction band in GaN and AlN probed by photoluminescence spectroscopy

III-nitrides are recognized as technologically important materials for optoelectronic and electronic devices. In particular, AlN is unique due to its ultrahigh direct bandgap as well as the ability of bandgap engineering through the use of alloying and heterostructures with GaN and is becoming more important for III-nitride device development. For device realization, understanding the fundamental properties of these materials is crucially important. Probing the optical properties such as the temperature dependence of the band edge transitions reveals important information pertaining to the fundamental band structures, exciton and carrier recombination and activation processes.

In undoped GaN, the dominant band edge transitions are due to the free exciton or free carrier recombination and the activation process is generally attributed to the dissociation of free excitons into free carriers [35,109-116]. Free-excitons in AlN have a very large binding energy and hence are expected to survive well above room temperatures [38,81]. However, high temperature emission properties of GaN and AlN have not been well studied.

In this work, the growth and photoluminescence (PL) studies of the band edge transitions in GaN and AlN epilayers up to 800 K has been presented. Two different activation processes have been observed in GaN and AlN. The first occurring at lower temperatures is attributed to the well-known process of exciton dissociation into free carriers, whereas the second newly observed process is an evidence for a higher lying energy level (or a satellite valley, Γ_3) of about 300 meV above the conduction band minimum (Γ_1). We attribute the second activation process to the electron population into this satellite valley (Γ_3) at higher temperatures. An emission line due to the recombination between free electrons in the Γ_3 satellite band and free holes in the top

most A-valence band has been directly observed in GaN at high temperatures, which corroborates our assignment. The results reported here are consistent with a previous result obtained by ballistic electron emission microscopy measurement, which revealed a satellite valley (Γ_3) of about 340 meV above the conduction band minimum (Γ_1) in GaN [117]. The onset temperature at which free excitons dissociate into free carriers has been determined for both GaN and AlN.

The 1 μm thick GaN and AlN epilayers were grown by metalorganic chemical vapor deposition (MOCVD) on sapphire (0001) substrates. Trimethylgallium (TMGa) and trimethylaluminium (TMAl) were used as Ga and Al sources, respectively. Atomic force microscopy (AFM) reveals crack free smooth surface with a 1 nm roughness across a 2 μm x 2 μm scanning area. The samples were mounted stress free on a high temperature stage with a cold finger in a closed-cycle helium refrigerator and the temperature was controlled between 10 and 800 K. Deep ultraviolet (UV) PL spectroscopy was employed to investigate the emission properties of these samples. The PL system consists of a frequency quadrupled 100 femtosecond Ti:sapphire laser with a repetition rate of 76 MHz and an average power of 3 mW at an excitation photon energy of 6.28 eV and a monochromator (1.3 m) [28].

The temperature evolutions of the dominant band edge emission lines in GaN and AlN epilayers have been measured in the temperature range from 10 to 800 K and are presented in Fig. 3.30 and 3.31 respectively. For GaN, the PL signals above 700 K were below the detection limit of our system, whereas the PL emission in AlN exhibits much weaker thermal quenching effect than in GaN due to the larger bandgap. In general, the spectral peak positions red shift with increasing temperature following the bandgap variations with temperature.
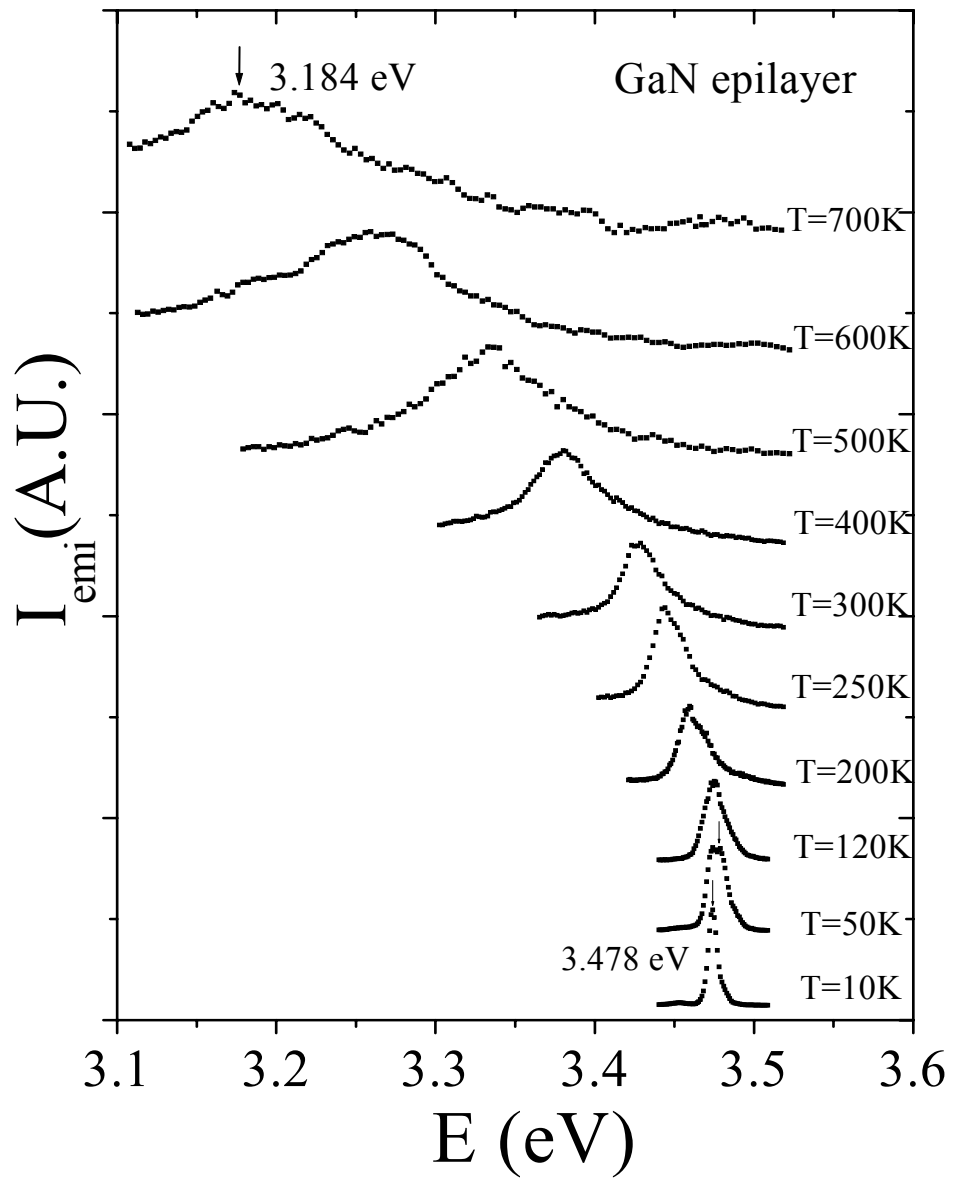
Fig. 3.30 PL spectra of GaN epilayer measured from 10 to 700 K.
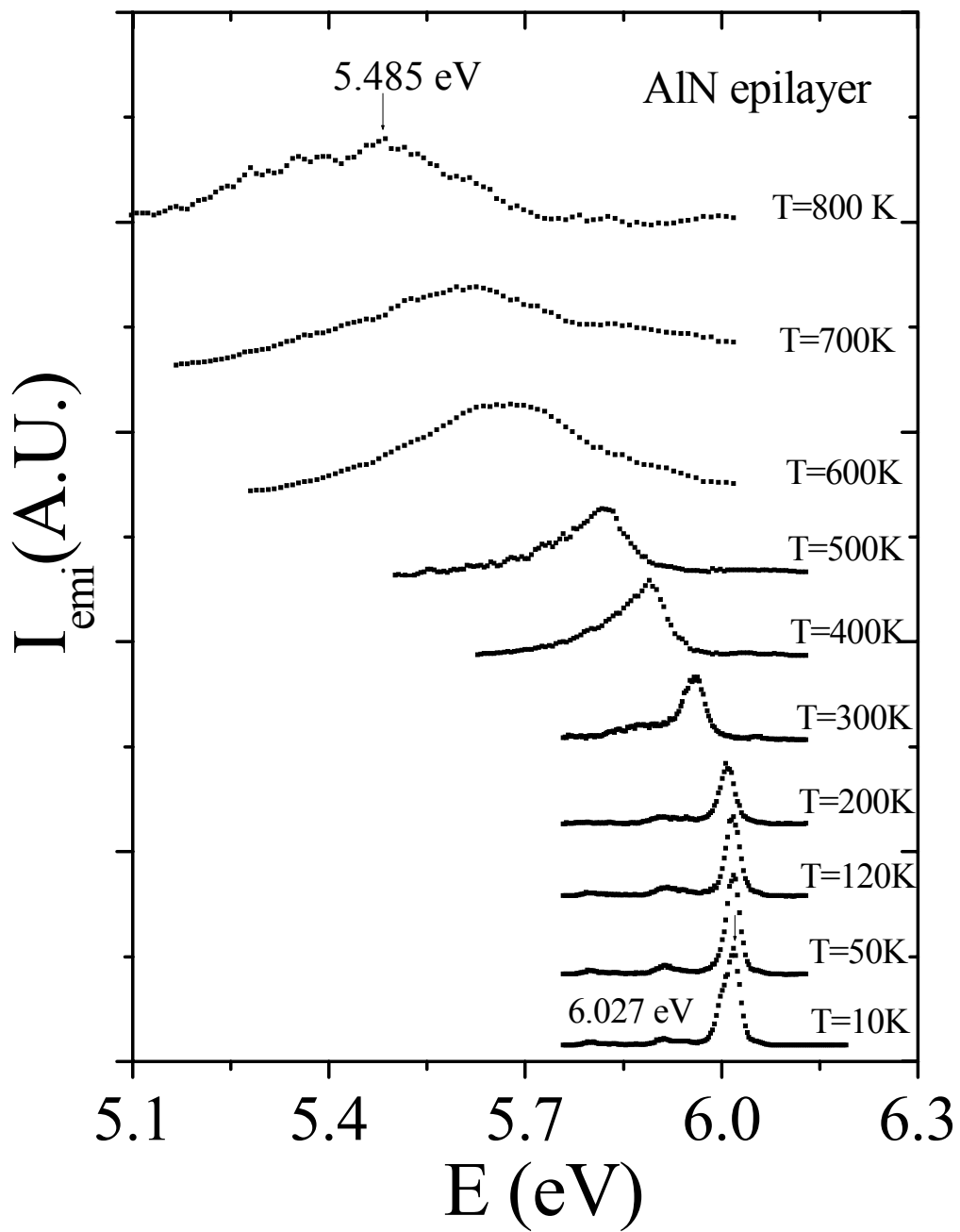
Fig. 3.31 PL spectra of AlN epilayer measured from 10 to 800 K.

The Arrhenius plot of the integrated PL emission intensity (I_{emi}) of the bandedge transition between 150 and 700 K for GaN epilayer is shown in Fig. 3.32. The solid curves are the least squares fit of the experimental results with the equation (3.6). It is clear that there are two distinctive activation processes in GaN. The first occurring between temperatures 150 and 325 K has been well studied and is due to the dissociation of free excitons into free carriers. The measured activation energy of 26 meV is very close to the exciton binding energy in GaN [110-116]. The second activation process occurring at elevated temperatures ($T_t > 325$ K) has not been previously observed. Above T_t (= 325 K), I_{emi} decreases more rapidly with temperature and the fitted value of the second activation energy is 0.29 ± 0.01 eV. The temperature, T_t, which separates the two distinctive activation processes, is also the measure of the onset temperature at which free excitons dissociate into free carriers.

A similar feature was observed for AlN epilayers. Figure 3.33 shows the Arrhenius plot of the integrated PL emission intensity, I_{emi}, of the band edge transition in AlN epilayer measured between 150 and 800 K. The band edge emission in AlN also exhibits two different activation processes, which however is separated by a temperature of $T_t = 500$ K that is much higher than that in GaN (325 K). The first activation energy of 79 meV is very close to the free exciton binding energy in AlN [38,81], once again suggesting that the process below T_t is due to the dissociation of free excitons into free carriers. The measured second activation energy is about 0.30 ± 0.01 eV. It is interesting to note the onset temperature, T_t, is much higher in AlN than in GaN and the free excitons survives up to 500 K in AlN, which is a direct consequence of a larger binding energy of free excitons in AlN. This demonstrates the advantage of AlN for high temperature and high power device applications.
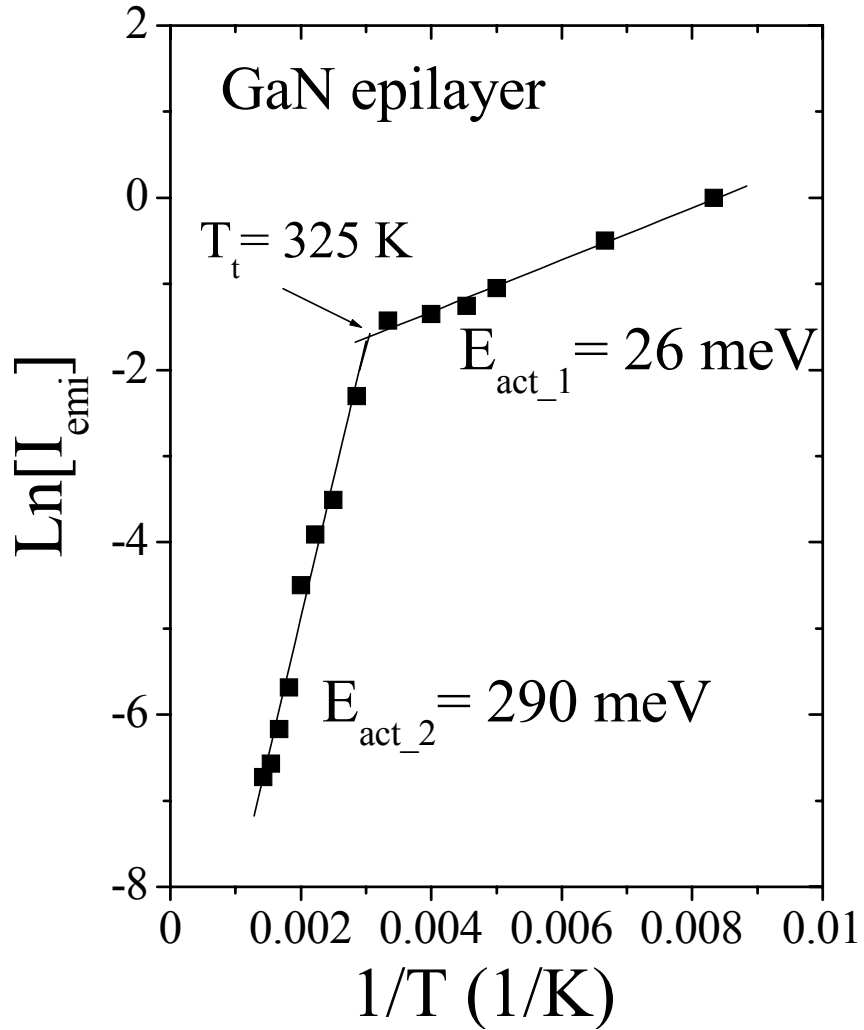
3.32 The Arrhenius plot of the integrated PL emission intensity (I_{emi}) of the dominant band edge transition in GaN. The solid lines are the least squares fit of the data with Eq. (3.6) for two different temperature ranges. Measured values of activation energies (E_{act_1} and E_{act_2}) are also indicated.
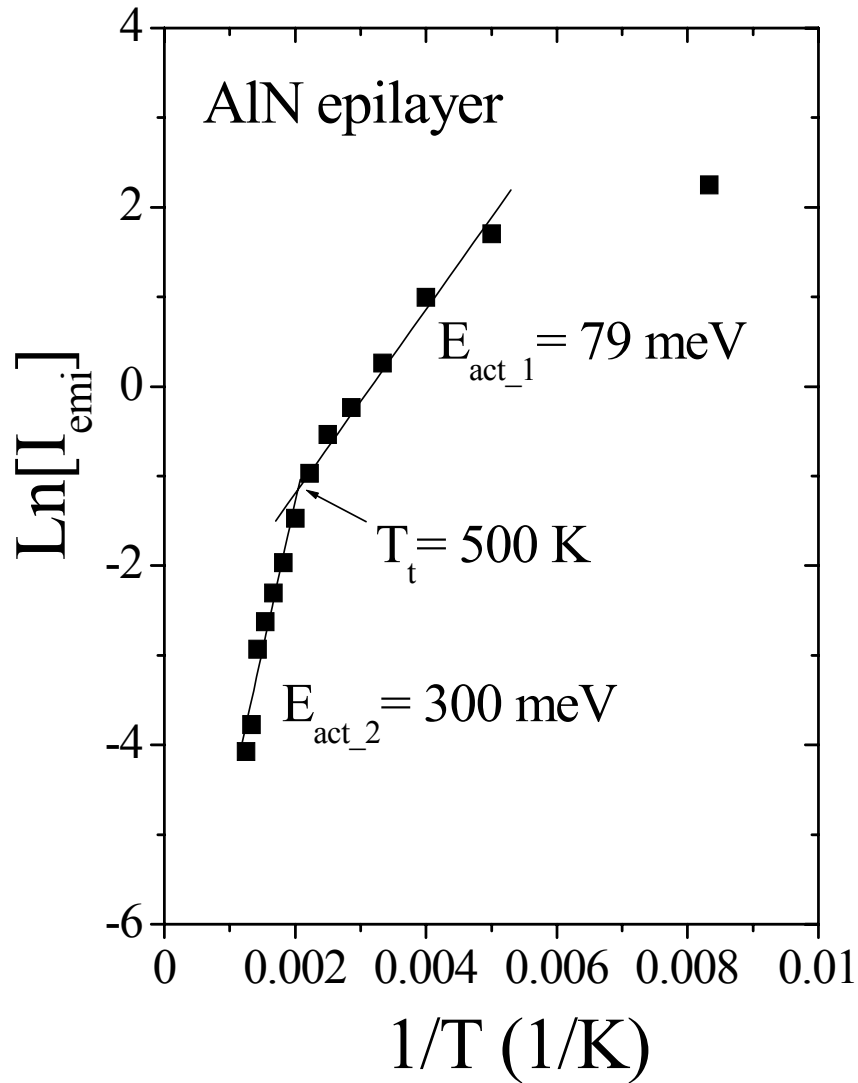
Fig. 3.33 The Arrhenius plot of the integrated PL emission intensity (I_{emi}) of the dominant band edge transition in AlN. The solid lines are the least squares fit of the data with Eq. (3.6) for two different temperature ranges. Measured values of activation energies (E_{act_1} and E_{act_2}) are also indicated.

Previous ballistic electron emission microscopy measurements revealed the existence of Γ_3 satellite valley at about 0.34 eV above Γ_1 [117]. Previous high-resolution reflectivity

experiment performed on GaN also showed evidence for a higher lying conduction band, Γ_3, at 300 – 400 meV above Γ_1 [118]. Although, these previous experimental results are inconsistent with the generally assumed energy band structure, which predicated that the nearest satellite valley is at about 2 eV above Γ_1 [119-120], our PL results presented here support a close higher lying energy level of about 0.29 eV (0.30 eV) above the conduction band minimum Γ_1 in wurtzite GaN (AlN). The newly observed second activation process in GaN and AlN can be naturally attributed to the activation of free electrons from in the conduction band minimum (Γ_1) to the satellite valley (Γ_3) at elevated temperatures.

Recent time-resolved electroabsorption measurements [121] have revealed an electron peak velocity lower and shifted to higher field than its theoretical counterpart obtained by assuming Γ_3 is about 2 eV above Γ_1 [122], which also hinted on the existence of a more closely located satellite valley above Γ_1 band that limits the electron drift velocity. A recent theoretical model has suggested a more closely located satellite valley at about 400 meV above Γ_1 [123].

To directly probe this higher lying satellite valley, we have performed more careful measurements on PL emission spectra of GaN and AlN at high temperatures and the result obtained at 700 K for GaN is shown in Fig. 3.34. An emission peak at 3.474 eV is clearly resolved, which is about 0.29 eV above the dominant band edge transition (at 3.184 eV). We believe that this is a direct observation of the recombination between the free electrons in the higher lying conduction band Γ_3 and the free holes in the A-valence band. The energy separation (0.29 eV) obtained from the PL spectrum shown in Fig. 3.32 agrees with the second activation energy measured from the temperature dependence of I_{emi} for $T > T_t$ shown in Fig. 3.32. An emission line of the same nature in AlN was not observable up to 800 K. It is possible that even

higher measurement temperatures may be needed in order to directly observe this emission line in AlN.
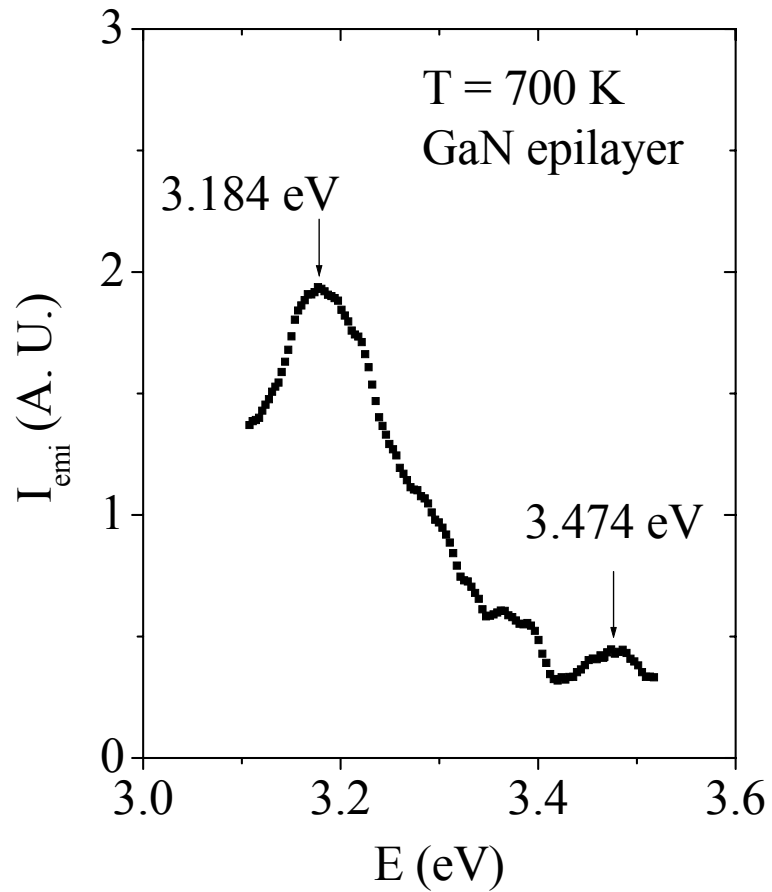
Fig. 3.34 PL spectrum of GaN epilayer at 700 K. A new emission peak at 3.474 eV, which is 0.29 eV above the dominant band edge transition at 3.184 eV, is evident.
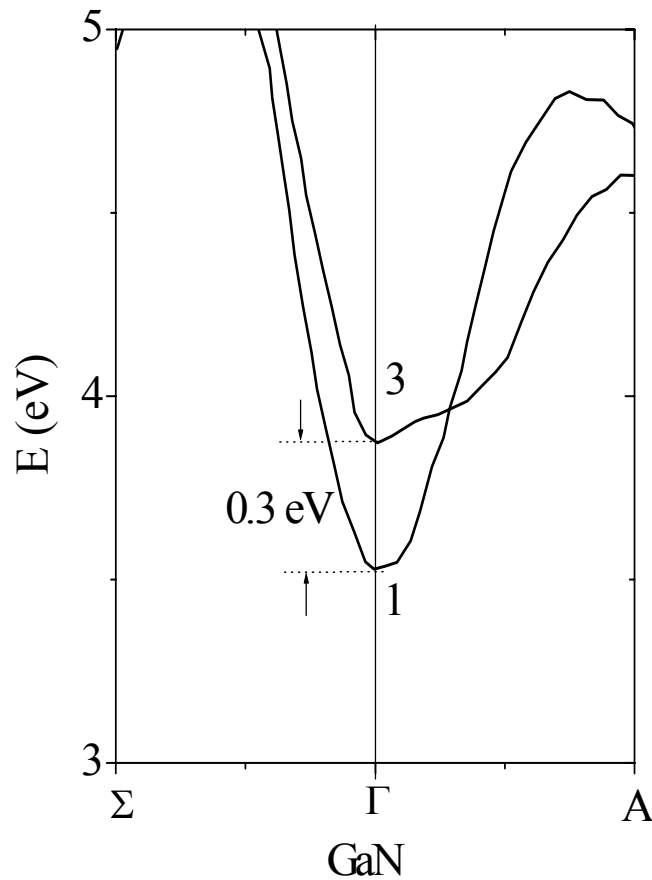
Fig. 3.35 The conduction band of GaN near the Γ-point (after Ref. 118).

Since wurtzite structure has 4 atoms/cell, there are twice as many bands per k point in the Brillouin zone (BZ) compared to that of zincblende structure (ZB). Consequently Γ_{3c} band in the wurtzite structure is the projection of L_c band in ZB structure and has less symmetry compared to Γ_{1c} band [124]. Because of the folded band, the radiative recombination efficiency associated with electrons in the Γ_3 band is expected to be low. Based on the experimental observations, the conduction band of wurtzite GaN near the Γ point with the proposed Γ_3 satellite band can be constructed and is schematically shown in Fig. 3.35 [118].

In summary, we have studied the band edge transitions in GaN and AlN epilayers by PL spectroscopy at elevated temperatures. Two different activation processes have been observed. The first activation process was due to the dissociation of free excitons into free carriers and the second activation process was attributed to the electron population in a higher lying conduction band, Γ_3, at about 290 meV (300 meV) above the conduction band minimum, Γ_1, of GaN (AlN). At 700 K, a PL emission peak at 0.29 eV above the dominant bandedge transition, which is associated with the Γ_3 satellite valley, was directly observed in GaN. The optically measured value of the Γ_3 satellite valley position in GaN is in good agreement with previously reported value obtained by BEEM measurements. The onset temperature at which free excitons dissociate into free carriers has been determined for both GaN and AlN.

3.8 Deep ultraviolet photoluminescence studies of AlN photonic crystals

Recently, there has been intensive R&D effort in the area of ultraviolet (UV) and deep UV optoelectronic materials and devices. One of the main challenges is finding effective methods and schemes to enhance the extraction efficiencies of deep UV emitters. A large fraction of the light generated in the semiconductors is trapped by total internal reflection as guided modes due to the higher refractive index of semiconductor and eventually lost due to parasitic absorption within the semiconductor. Moreover, the UV emitters using AlGaN as active layers possess unique polarization properties compared to more conventional semiconductors. In Al-rich AlGaN alloys the recombination between the conduction band electrons and holes in the top-most valance band is prohibited for the polarization configuration of **E⊥c**, while the allowed **E//c** emission component cannot easily get out of the escaping cone [38,125]. Various schemes have been employed to enhance the extraction of light from light emitting diodes (LEDs). Among these techniques, surface roughening [126-129], μ-LED arrays [130], photonic crystals (PCs) [131-142], and integrated microlens arrays [143] have been utilized.

Much progress has been made on the understanding and fabrication PCs that function in the infrared (IR) region [131-134]. A maximum of 30-fold enhancement in photoluminescence (PL) emission intensity from a freestanding InGaAs PC slab has been reported at a wavelength of 1100 nm [133]. A 6-fold enhancement in emission intensity at 925 nm has been obtained from an LED structure upon PC formation under optical pumping [134]. Nitride PCs that function in the visible and UV regions have been studied only very recently due to the challenges associated with the fabrication of PCs with sub-micron periodicity [135-142]. We reported a 20-fold enhancement in PL emission intensity from an InGaN/GaN multiple quantum well (MQW) at 475 nm [135]. Under the guidance of the optical pumping studies, we have realized nitride PC

LEDs active in the wavelength range of 333 - 460 nm and a maximum of 2.5-fold power enhancement at 333 nm was obtained under current injection [136-139].

In this work, the successful fabrication and deep UV PL studies of AlN PCs has been presented. Two-dimensional arrays of PCs were fabricated on AlN epilayers grown by metal-organic chemical vapor deposition (MOCVD) using electron-beam (e-beam) lithography and inductively coupled plasma (ICP) dry etching. In order to observe the PC effects in the deep UV region, we patterned the air hole size below 100 nm. A 20-fold enhancement in the PL emission intensity in the deep UV region (down to 208 nm) was observed upon PC formation in AlN. The emission intensity was observed to increase with a decrease of the PC lattice constant.

The 1 μm thick AlN epilayers were grown by MOCVD on sapphire (0001) substrates. Trimethylaluminium (TMAl) and blue ammonia were used as Al and N sources, respectively. Atomic force microscopy (AFM) and scanning electron microscopy (SEM) were used to characterize the surface morphology of these epilayers. Structural characterization was done with x-ray diffraction (XRD) measurement. Full width at half maximum (FWHM) of XRD rocking curve of (0002) peak of AlN epilayers was between 50 to 100 arcsec. The PCs with triangular lattice patterns of circular air holes with varying diameter (d) from 75 to 300 nm and periodicity or lattice constant (a) from 150 to 600 nm were defined in an area of 10 μm x 10 μm using e-beam lithography and ICP dry etching as described previously [135,136,138,139]. Figure 3.36(a) and 3.36(b) show the AFM and SEM images of AlN PCs with periodicity/diameter (a/d) of 180/90 nm.
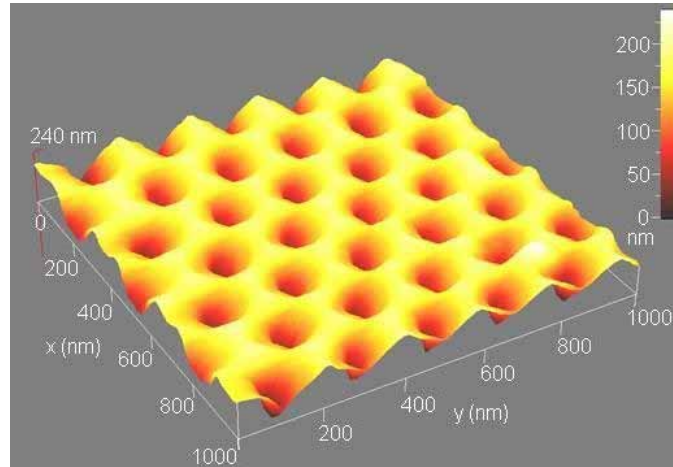
(a)
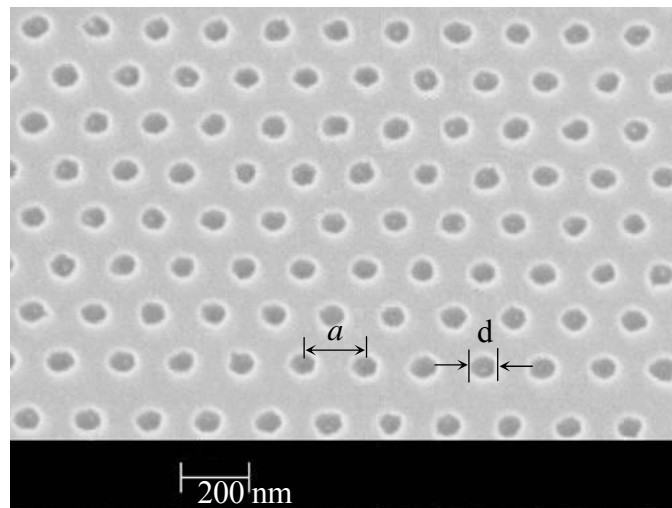
(b)

Fig. 3.36 (a) AFM and (b) SEM images of the AlN PCs with periodicity/diameter (*a*/d) of 180/90 nm.

Deep UV PL spectroscopy was employed to investigate the optical properties of AlN PCs. The PL system consists of a frequency quadrupled 100 femtosecond Ti:sapphire laser with an average power of 3 mW with excitation photon energy set at 197 nm or 6.28 nm (repetition

rate of 76 MHz), a monochromator (1.3 m) [28]. An UV objective was used to focus 197 nm laser beam onto a tight spot of about 2 μm in diameter on AlN PCs with different size features. Schematic diagram of the PL setup used for the optical measurement is shown in Fig. 3.37. Samples were mounted on a sample holder in such a way that the **k** vector of the emitted light is parallel to the c-axis and the incident laser beam with vertical polarization makes 45° degrees with respect to the c-axis.
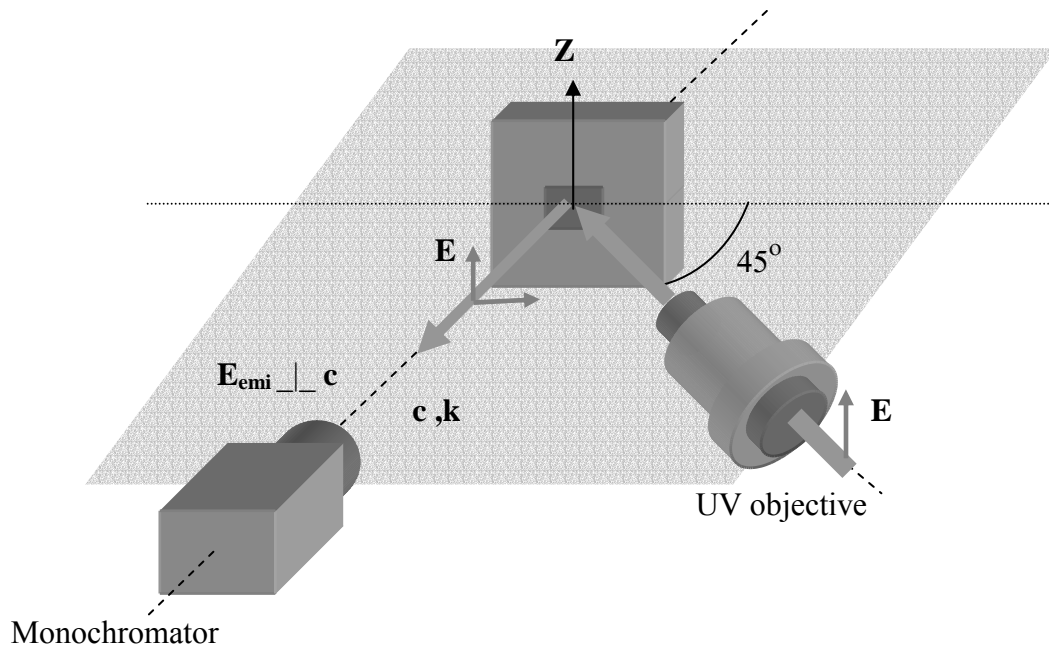
Fig. 3.37 Schematic diagram of the PL setup for the optical measurement of AlN PCs.

The room temperature PL spectra of AlN epilayers with and without PC formation are shown in Fig. 3.38. The dominant emission line at 5.97 eV is attributed to the band edge emission in AlN. An additional weak emission line endicated as E_{exc}-2LO is also visible, which was attributed to the Raman scattering of the excitation laser line with two longitudinal optical (2LO) phonons with LO phonon energy of 110 meV. (2LO) of excitation laser line at 6.28 eV,

with LO phonon energy of 110 meV [38]. An interesting fact is that E_{exc}-LO is absent, which may be related to the symmetry properties involved.
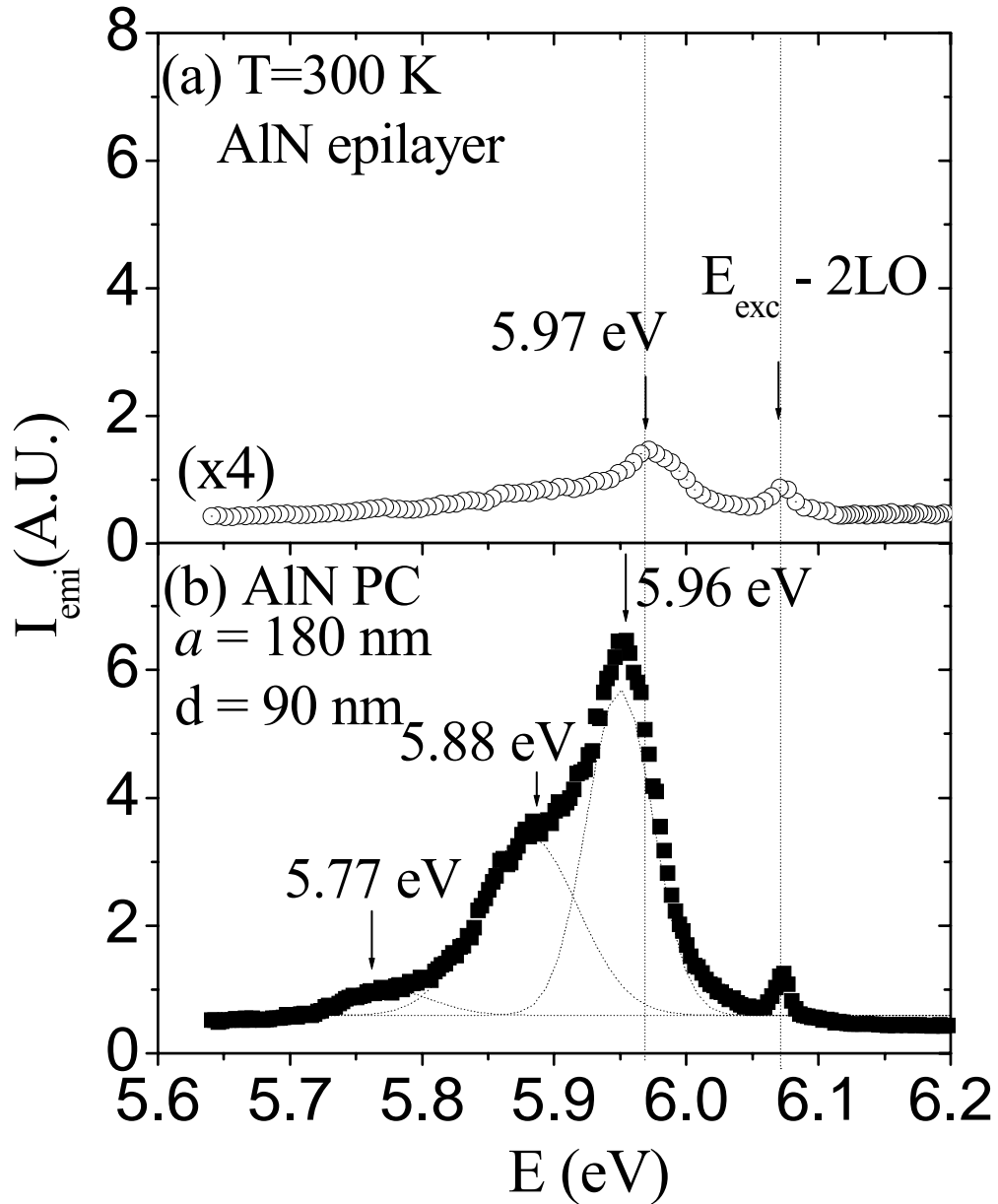
Fig. 3.38 PL spectra of (a) AlN epilayer (b) AlN PCs with periodicity/diameter (a/d) of 180/90 nm at 300 K. The PL emission intensity (I_{emi}) of AlN PCs is 20 times higher than that of unpatterned AlN epilayer.

The spectral peak position of the band edge emission decreases to 5.96 eV in AlN PCs of dimension a/d = 180/90 nm. There are also emission lines at 5.88 and 5.77 eV. Since we are probing the sample using vertically polarized laser at an angle of about 45°, mixed A_1-E_1 symmetry phonons may also be observed besides pure transverse optical (TO) or LO phonons. Measured phonon energies of E_1(TO) and A_1(LO) phonons in AlN were 80 and 110 meV, respectively [144]. We believe that the emission peaks at 5.88 (80 meV below 5.96 eV) and 5.77 eV (80+110 meV below 5.96 eV) are due to E_1(TO) and E_1(TO)+A_1(LO) phonon replicas, respectively. The formation of PCs on AlN produced emission intensity enhancement of 20-fold as compared to that of unpatterned AlN epilayer. Besides the band edge transition, PCs also enhance emission intensity of the TO and TO+LO phonon replica lines. PC folds the guided modes at the Brillouin zone boundaries allowing phase matching to the radiation mode that lie above the air light line. Hence enhancement could be due to Bragg scattering of the emitted light by PCs.

Figure 3.39 shows the periodicity and hole size dependence of the room temperature PL spectra for a = 150 to 600 nm measured for AlN PCs. The ratio of air-hole radius r (d = 2r) to the lattice constant a is fixed at 0.25 for all AlN PCs. We attribute the dominant emission line to the band edge transition in AlN PCs and there is a laser 2LO phonon line at 6.06 eV in each spectrum. The spectral peak position of the band edge transition, E_p, decreases from 5.970 eV at a = infinity (epilayer) to 5.952 eV at a = 150 nm. However the emission intensity (I_{emi}) increases with decreasing the lattice constant.
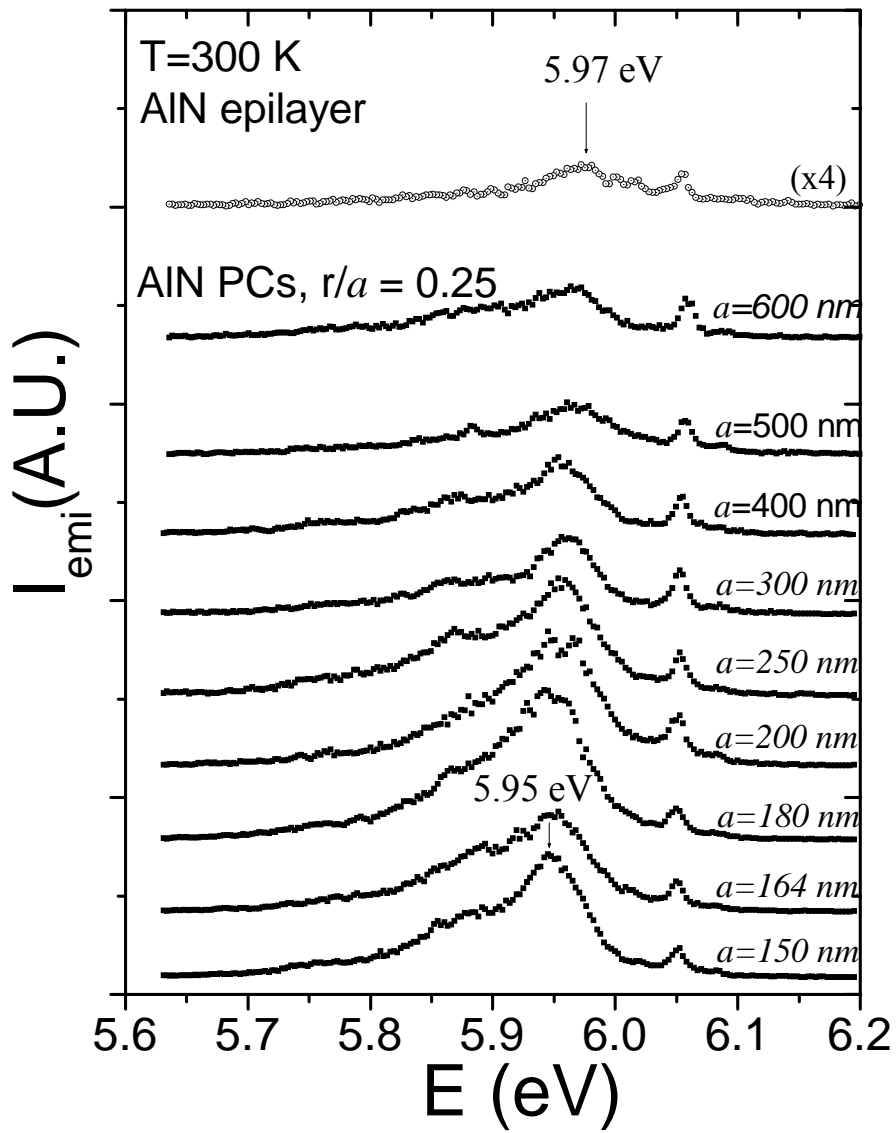
Fig. 3.39 PC size feature dependence of the PL spectra. The integrated emission intensity (I_{emi}) of AlN PCs increases with decreasing lattice constant for a constant air-filling factor (r/a = 0.25).
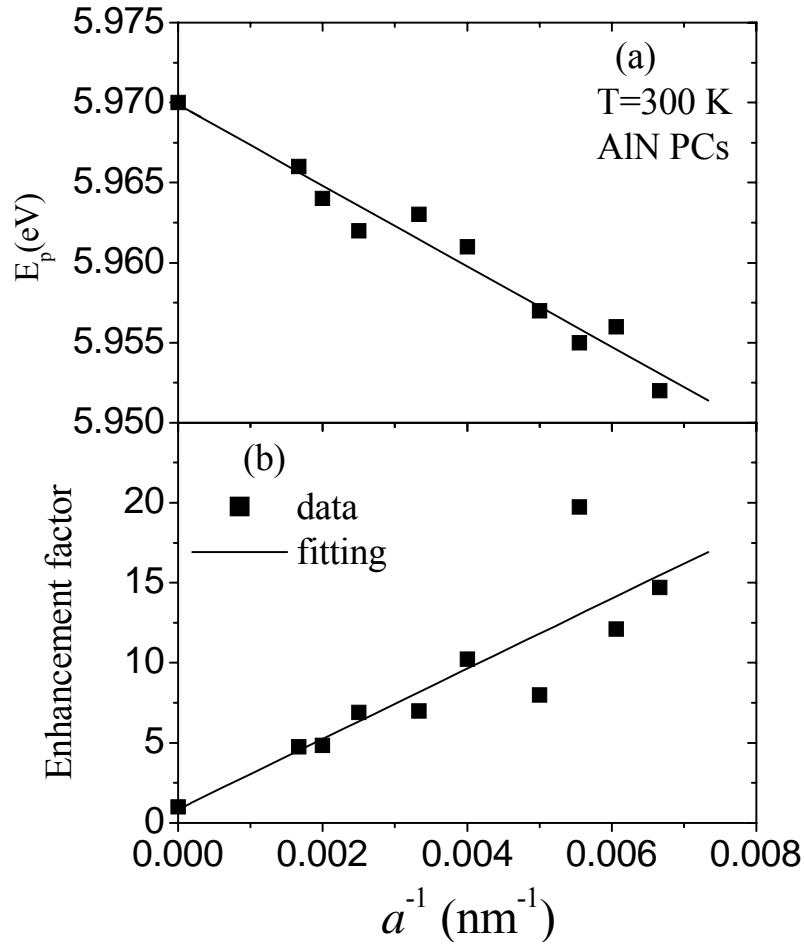
Fig. 3.40 Lattice constant dependence of the (a) PL emission peak energy and (b) light enhancement factor in AlN PCs. The solid lines are the linear fits of data. The PL emission spectral peak energy decreases, while the integrated emission intensity increases with decreasing lattice constant, a.

The lattice constant dependence of the emission peak energy of AlN PCs is shown in Fig. 3.40(a). The straight line is the linear fit of the data with $E_p = E_p(a = \infty) - c/a$, where c is a proportionality constant. Figure 3.40(a) shows that E_p decreases linearly with $1/a$ of PCs. This is due to the fact that the PC feature is small enough to alter the strains in the epilayer. TEM and

high-resolution XRD studies provide evidence that the final resultant stress is compressive in our AlN epilayers grown on sapphire substrate [145]. E_p decreases when compressive stresses are released because of etched air holes. The enhancement factor for I_{emi} varies linearly with the inverse of the lattice constant (a^{-1}) of AlN PCs, as illustrated in Fig. 3.40 (b). We define the PL enhancement factor as the integrated PL emission intensity of AlN PCs relative to that of the unpatterned AlN epilayer. The enhancement factor increases with decreasing lattice constant for a constant air-filling factor (r/a = constant) and reaches a maximum of 20-fold for a = 180 nm. Variation of PL enhancement factor with lattice constant has been reported in a previous work at an emission wavelength of 1100 nm for InGaAs PCs [136], in which the enhancement factor was a maximum at a = 800 nm and then decreases with a on both sides for either a > 800 nm or a < 800 nm. In the case of AlN deep UV PCs, the PL enhancement factor increases with decreasing lattice constant in the range of the present study down to a = 150 nm. In a typical as-grown sample, the extraction efficiency is about 5%. Numerically, the 20-fold enhancement corresponds to an extraction efficiency approaching 100%.

PCs enhance emission intensity in several ways. Enhancement due to Purcell effect may be limited. Bragg scattering of photons by periodically varying refractive indices creates a photon band gap (PBG) in which lateral propagation of the Bloch guided mode is prohibited and light generated in the bandgap region can couple only to the radiation modes and is radiated outward. Also, the PCs fold the guided modes into the Brillouin zone boundaries, allowing phase matching to the radiation modes that lie above the air light line [146]. The guided modes that phase match with the radiation modes escape eventually as Bragg scattered light. The midgap frequency of the PBG of triangular PCs of air hole in GaN with dielectric constant ε = 8.9 is estimated to be around the normalized frequency (a/λ) of 0.5 [147]. In AlN a periodicity of less

than 104 nm is required to tune the PBG to the emission wavelength in deep UV (~208 nm) region. The smallest normalized frequency of our structure is 0.72 for emission wavelength at 208 nm, which implies that photon modes in our structure lie above the cut-off frequency of guided modes. We therefore believe that the PL enhancement in our AlN PCs is mainly due to coupling of leaky modes above the cut-off frequency of the Bloch guided modes. Another factor is that the light cannot escape from AlN epilayers due to the unique polarization property. With PC formation, much of the **E**//**c** emission component can be extracted from the epilayers.

In summary, PCs with feature size down to 75 nm have been fabricated on AlN epilayers. The optical properties were studied with deep UV PL spectroscopy. PC formation produced an enhancement factor of about 20 in band edge PL emission intensity over unpatterned AlN epilayer at 208 nm for a/d = 180/90 nm. It was found that the PL enhancement factor increases with decreasing the lattice constant. The emission peak energy was observed to decrease with decreasing lattice constant possibly due to the relive of compressive strain in AlN epilayers upon PC formation.

CHAPTER 4 General Conclusions

Deep ultraviolet (UV) photoluminescence (PL) spectroscopy has been employed to study optical properties of MOCVD grown AlGaN alloys and AlN epilayers. CW PL, temperature dependent, time-resolved PL, and optical pumping have been carried out on AlGaN alloys and AlN epilayers.

Compositional and temperature dependence of the bandgap of $Al_xGa_{1-x}N$ alloys covering the entire alloy range, $0 \leq x \leq 1$ has been measured up to 800 K. Band-edge emission peaks were fitted with Varshni equation to obtain Varshni coefficients α and β. A parabolic dependence of α and β with x in $Al_xGa_{1-x}N$ was observed, from which we have obtained an empirical equation that describes the compositional and temperature variations of the energy bandgap of AlGaN alloys.

The exciton localization effect in $Al_xGa_{1-x}N$ alloys have been investigated for the entire composition range, $0 \leq x \leq 1$. Our experimental results demonstrated that the localized exitons in AlGaN alloys have the largest localization energies compared to all other semiconductor alloys. We have established effective methods for directly measuring the exciton localization energies (E_{Loc}) in AlGaN alloys and confirmed that E_{Loc} can be obtained by measuring either the deviation of the exciton emission peak energy with the Varshni equation at low temperatures or the thermal activation energy of the exciton emission intensity or the exciton emission linewidth. The exciton localization energy in $Al_xGa_{1-x}N$ alloys was observed to increase with x and reach maximum for $x \sim 0.7$, implying that the potential fluctuation caused by alloy disorder is also a maximum at that value of x, consistent with the theoretical calculation result assuming completely random alloys [66,67]. Exciton localization is prominent in wide-gap AlGaN alloys due to their small Bohr radius and a large difference in energy gaps between GaN and AlN. This

large exciton localization may give rise to increased quantum efficiency due to reduction of nonradiative recombination rate under the influence of the carrier localization effect. However, carrier localization will reduce the conductivity of AlGaN alloys, particularly for Al content around 70%. Thus, strong carrier and exciton localization can have an effect on the optical and electrical properties of deep UV optoelectronic devices.

Impurity transitions involving cation vacancies and complexes in $Al_xGa_{1-x}N$ alloys grown on sapphire substrates have been studied between x = 0 and 1. A group of impurity transitions of DAP type with higher emission energies than those of the previously identified $(V_{III})^{3-}$ and $(V_{III}$-complex$)^{2-}$ related transitions was observed. The deep level acceptors involved in these transitions have been identified as $(V_{III}$-complex$)^{1-}$. The energy levels of these deep acceptors in $Al_xGa_{1-x}N$ alloys increase almost linearly with x from 0.55 eV in GaN to 1.25 eV in AlN and are pinned to a common energy level in vacuum. Experimentally measured energy difference between the $(V_{III}$-complex$)^{2-}$ and $(V_{III}$-complex$)^{1-}$ deep level acceptors in AlGaN alloys (0.7 eV) agrees with the calculated value (0.7 eV). AlGaN alloys predominantly exhibiting the bandedge and $(V_{III}$-complex$)^{1-}$ transitions possess improved conductivities over those emit predominantly $(V_{III})^{3-}$ and $(V_{III}$-complex$)^{2-}$ related transitions.

An emission line at 6.02 eV has been observed in Mg-doped AlN epilayers, which was absent in undoped AlN epilayers and is 40 meV below the FX transition in undoped AlN. This emission line is due to the recombination of the exciton bound to neutral Mg acceptor in AlN. This assignment has been confirmed by the time-resolved measurement at 10 K and the temperature dependence of the PL intensities. Measured binding energy of exciton bound to Mg impurity in AlN is 40 meV that is twice as that in GaN, as expected with larger effective masses of electrons and holes in AlN than in GaN. The observed large acceptor-bound exciton binding

energy implies that excitons in AlN are extremely robust entities. The measured PL decay lifetime of the I_1 transition in Mg-doped AlN is 130 ps. The decay lifetime increases with decreasing excitation intensity, which indicates that the PL quantum yield increases with increasing excitation intensity.

In Zn-doped AlN epilayers, Zn related impurity transitions were observed at 5.40 and 4.50 eV in Zn-doped AlN, which are absent in undoped AlN layers. By comparing the PL spectra of Zn-, Mg-doped and undoped AlN epilayers, the energy level of Zn acceptor in AlN was deduced to be about 0.74 eV, which is about 0.23 eV deeper than Mg level in AlN. In contrary to a previous theoretical prediction, our results thus suggest that Zn is not a better candidate than Mg as a p-type dopant in AlN. More theoretical and experimental investigations are required to further understand doping issues in AlN, particularly pertaining p-type doping. Besides searching for suitable acceptor elements, innovative doping methods also need to be developed to bring a breakthrough in this field.

MOCVD grown AlN epilayers have been implanted with Co ions. An emission line at 5.87 eV has been observed, which was absent in as-grown AlN epilayers. This emission line has been attributed to a band-to-impurity transition between electrons bound to nitrogen vacancies and free holes. The experimentally determined nitrogen vacancy energy level is around 260 meV, which is in reasonable agreement with the calculated value of 300 meV. As a consequence of the large activation energy (0.26 eV) as well as high formation energy, V_N in AlN cannot contribute significantly to the n-type conductivity.

At elevated temperatures, two different activation processes have been observed in GaN and AlN epilayers. The first activation process was due to the dissociation of free excitons into free carriers and the second activation process was attributed to the electron population in a

higher lying conduction band, Γ_3, at about 290 meV (300 meV) above the conduction band minimum, Γ_1, of GaN (AlN). At 700 K, a PL emission peak at 0.29 eV above the dominant bandedge transition, which is associated with the Γ_3 satellite valley, was directly observed in GaN. The optically measured value of the Γ_3 satellite valley position in GaN is in good agreement with previously reported value obtained by BEEM measurements.

Photonic crystals (PCs) with feature size down to 75 nm have been fabricated on AlN epilayers. PC formation produced an enhancement factor of about 20 in band edge PL emission intensity over unpatterned AlN epilayer at 208 nm for a/d = 180/90 nm. It was found that the PL enhancement factor increases with decreasing the lattice constant. The emission peak energy was observed to decrease with decreasing lattice constant possibly due to the relief of compressive strain in AlN epilayers upon PC formation.

References

[1]   Nitride News, *Compound Semiconductor,* Vol.3, page 4, 1997.

[2]   Tim Whitaker, *Compound Semiconductors* 7, 50 (2001).

[3]   *Gallium Nitride Semiconductors and Semimetals* **50**, edited by J. I. Pankove and   T. D. Moustakas (Academic Press 1998).

[4]   S. Nakamura and G. Fasol, *The Blue Laser Diode*, (Springer, New York, 1997).

[5]   F. Fichter, Z. Anorg. Chem. **54**, 322 (1907)

[6]   H. P. Muruska, J. I. Pankove, E. A. Miller, and J. E. berkeyheiser, RCA Rev. **32**, 383 (1971).

[7]   H. P. Maruska, and J. J. Tietjen, Appl. Phys. Lett. **15**, 327(1969).

[8]   H. M. Manasevit, E. M. Erdmann and W. I. Simpson, J. Electrochem. Soc., **118**, 1864 (1971).

[9]   H. Amano, N. Sawaki, I. Akasaki, and Y. Toyoda, Appl. Phys. Lett. **48**, 353 (1986).

[10]   H. Amano, M. Kito, K. Hiramatsu, and I. Akasaki, Jpn. J. Appl. Phys. **28**, L2112 (1989).

[11]   S. Nakamura, T. Mukai, M. Senoh, and N. Iwasa, Jpn. J. Appl. Phys. **31**, L139 (1992).

[12]   S. Strite and H. Morkoc, J. Vac. Sci. Technol. B 10(4), 1237 (1992).

[13]   *Properties of Group-III Nitrides*, edited by J. H. Edgar (INSPEC, IEE, London, 1994).

[14]   I. Vurgaftman, J. R. Meyer, *and* L. R. Ram-Mohan, J. Appl. Phys. **89**, 5815 (2001).

[15]   M. Henini and M. Razeghi, *Optoelectronic devices: III Nitrides*, (Elsevier, 2005) and references therein.

[16]   Y. Taniyasu, M. Kasu, and T. Makimoto, Nature **441**, 325 (2006).

[17]   T. Matsutani, M. Kiuchi, K. Shirouzu, A. Yoshioka, R. Shimizu, and S. Takahashi, Solid State Phenom. **107**, 43 (2005).

[18]   V. Mortet, O. Elmazria, M. Nesladek, M. B. Assouar, G. Vanhoyland, J. D'Haen, M. D'Olieslaeger, and P. Alnot, Appl. Phys. Lett. **81**, 1720 (2002).

[19]   A. T. Sowers, J. A. Christman, M. D. Bremser, B. L. Ward, R. F. Davis, and R. J. Nemanich, Appl. Phys. Lett. **71**, 2289 (1997).

[20]   Y. Taniyasu, M. Kasu, and N. Kobayashi, Appl. Phys. Lett. **81**, 1255 (2002).

[21]   M. L. Nakarmi, K. H. Kim, K. Zhu, J. Y. Lin, and H. X. Jiang, Appl. Phys. Lett. **85**, 3769 (2004).

[22]   Y. Taniyasu, M. Kasu, and T. Makimoto, Appl. Phys. Lett. **85**, 4672 (2004).

[23]   T. Ive, O. Brandt, H. Kostial, K. J. Friedland, L. Daweritz, and K. H. Ploog, Appl. Phys. Lett. **86**, 024106 (2005).

[24]   R. J. Molnar and T. D. Moustakas, Bull. Am. Phys. Soc. **38**, 445 (1993).

[25]   T. Tanaka, A. Watanable, H. Amino, Y. Kobayashi, I. Akasaki, S. Yamazaki, and M. Koike, Appl. Phys. Lett. **65**, 593 (1994).

[26]   J. Li, T. N. Oder, M. L. Nakarmi, J. Li, J. Y. Lin, and H. X. Jiang, Appl. Phys. Lett. **80**, 1210 (2002).

[27]   K. B. Nam, M. L. Nakarmi, J. Li, J. Y. Lin, and H. X. Jiang, Appl. Phys. Lett. **83**, 878 (2003).

[28]   http://www.phys.ksu.edu/area/GaNgroup.

[29]   J. Neugebauer and C.G. Van de Walle, Appl. Phys. Lett. **69**, 503 (1996).

[30]   T. Mattila and R.M. Nieminen, Phys. Rev. B **55**, 9571 (1997).

[31]   C. Stampfl and C.G. Van de Walle, Phys. Rev. B **65**, 155212 (2002).

[32]   I. Gorczyca, N.E. Christensen and A. Svane, Phys. Rev. B **66**, 075210 (2002).

[33]   K. B. Nam, M. L. Nakarmi, J. Y. Lin, and H. X. Jiang, Appl. Phys. Lett. **86**, 222108 (2005).

[34]   S. L. Chuang and C. S. Chang, Appl. Phys. Lett. **68**, 1657 (1996).

[35]   G. D. Chen, M. Smith, J. Y. Lin, H. X. Jiang, S.-H. Wei, M. Asif Khan, and C. J. Sun, Appl. Phys. Lett. **68**, 2784 (1996).

[36]   R. Dingle, D. D. Sell, S. E. Stokowski, and M. Ilegems, Phys. Rev. B **4**, 1211 (1971).

[37]   M. Monemar, Phys. Rev. B **10**, 676 (1974).

[38]   J. Li, K. B. Nam, M. L. Nakarmi, J. Y. Lin, H. X. Jiang, P. Carrier, and S. H. Wei, Appl. Phys. Lett. **83**, 5163 (2003).

[39]   M. Goano, E. Bellotti, E. Ghillino, C. Garetto, G. Ghione, and K. F. Brennan, J. Appl. Phys. **88**, 6476 (2000).

[40]   Q. Chen, J. W. Yang, A. Osinsky, S. Gangopadhyay, B. Lim, M. Z. Anwar, M. Asif Khan, D. Kuksenkov, and H. Temkin, Appl. Phys. Lett. **70**, 2277 (1997).

[41]   A. Osinsky, S. Gangopadhyay, B. W. Lim, M. Z. Anwar, M. A. Khan, D. V. Kuksenkov, and H. Temkin, Appl. Phys. Lett. **72**, 742 (1998).

[42]   M. Razeghi, Proc. IEEE, **90**, 1006 (2002).

[43]   H. Miyake, H. Yasukawa, Y. Kida, K. Ohta, Y. Shibata, A. Motogaito, K. Hiramatsu, Y. Ohuchi, K. Tadatomo, Y. Hamamura, and K. Fukui, Phys. Stat. Sol. (a) **200**, 151 (2003).

[44]   Y. Taniyasu, M. Kasu, and T. Makimoto, Appl. Phys. Lett. **84**, 2115 (2004).

[45]   *Semiconductors probed by ultrafast laser spectroscopy*, edited by R.R. Alfano (*Academic Press*, Orlando, 1984).

[46]   A. Lewis, M. Isaacson, A. Harootunian and A. Murray, Ultramicroscopy **13**, 227 (1984).

[47]   http://www.nanonics.co.il/

[48]   M. Ohtsu and Hirokazu Hori, *Near-field nano-optics* (*Kluwer Academic/Plenum Publishers*, New York, 1999)

[49]   http://www.quesant.com

[50]   K. B. Nam J. Li, M. L. Nakarmi, J. Y. Lin, and H. X. Jiang, Appl. Phys. Lett. **81**, 1038 (2002).

[51]   M. C. Kuo, K. C. Chiu, T. H. Shin, Y. J. Lai, C. S. Yang, W. K. Chen, D. S. Chuu, M. C. Lee, W. C. Chou, S. Y. Jeng, Y. T. Shih, and W. H. Lan, Jpn. J. Appl. Phys. **43**, 5145 (2004).

[52]   Y. T. Shih, W. C. Fan, C. S. Yang, M. C. Kuo, and W. C. Chow, J. Appl. Phys. **94**, 3791 (2003).

[53]   K. B. Nam, J. Li, J. Y. Lin, and H. X. Jiang, Appl. Phys. Lett. **85**, 3489 (2004).

[54]   B. K. Meyer, G. Steude, A. Goldner, A. Hofmann, H. Amano, and I. Akasaki, Phys. Stat. Sol. (b) **216**, 187 (1999).

[55]   H. S. Kim, R. A. Mair, J. Li, J. Y. Lin, and H. X. Jiang, Appl. Phys. Lett. **76**, 1252 (2000).

[56]   D. Brunner, H. Angerar, E. Bustarret, F. Freudenberg, R. Hopler, R. Dimitrov, O. Ambacher, and M. Stutzmann, J. Appl. Phys. **82**, 5090 (1997).

[57]   G. Coli, K. K. Bajaj, J. Li, J. Y. Lin, and H. X. Jiang, Appl. Phys. Lett. **78**, 1829 (2001).

[58]   G. Coli, K. K. Bajaj, J. Li, J. Y. Lin, and H. X. Jiang, Appl. Phys. Lett. **80**, 2907 (2002).

[59]   K. P. O'Donnell and X. Chen, Appl. Phys. Lett. **58**, 2924 (1991).

[60]   E. Grilli, M. Guzzi, R. Zamboni, and L. Pavesi, Phys. Rev. B **45**, 1638 (1992).

[61]   W. Bludau, A. Onton, and W. Heinke, J. Appl. Phys. **45**,1846 (1974).

[62]   Y. Li, Y. Lu, H. Chen, M. Wraback, M. G. Brown, M. Schurman, L. Koszi, and R. A. Stall, Appl. Phys. Lett. **70**, 2458 (1997).

[63]   Y. P. Varshni, Physica (Utrecht) **34**, 149 (1967).

[64]   H. X. Jiang, L. Q. Zu, and J. Y. Lin, Phys. Rev. B **42**, 7284 (1990).

[65]   M. S. Lee, and K. K. Bajaj, J. Appl. Phys. **73**, 1788 (1993).

[66]   A. Bell, S. Srinivasan, C. Plumlee, H. Omiya, F. A. Ponce, J. Christen, S. Tanaka, A. Fujioka, and Y. Nakagawa, J. Appl. Phys. **95**, 4670 (2004).

[67]   S. Lankes, H. Stanzl, K. Wolf, M. Giegler, and W. Gebhardt, J. Phys. Condens. Matter **7**, 1287 (1995).

[68]   J. Osaka, Y. Ohno, S. Kishimoto, K. Maezawa, and T. Mizutani, Appl. Phys. Lett. **87**, 222112 (2005).

[69]   T. Ogino and M. Aoki, Jpn. J. Appl. Phys. **19**, 2395 (1980).

[70]   S. J. Rhee, S. Kim, E. E. Reuter, S. G. Bishop, Appl. Phys. Lett. **73**, 2636 (1998).

[71]   P. Perlin, T. Suski, H. Teisseyre, M. Leszczynski, I. Grzegory, J. Jun, S. Porowski, P. Bogustawski, J. Bernholc, J. C. Chervin, A. Polian, and T. D. Moustakas, Phys. Rev. Lett. **75**, 296 (1995).

[72]   B. J. Skrome, J. Jayapalan, R. P. Vaudo, and V. M. Phanse, Appl. Phys. Lett. **74**, 2358 (1999).

[73]   J. Elsner, R. Jones, M. I. Heggie, P. K. Sitch, M. Haugk, Th. Frauenheim, S. Oberg, and P. R. Briddon, Phys. Rev. B **58**, 12571 (1998).

[74]   R. A. Youngman and J. H. Harris, J. Am. Ceram. Soc. **73**, 3238 (1990).

[75]   H. C. Yang, T. Y. Lin, and Y. F. Chen, Phys. Rev. B **62**, 12595 (2000).

[76]   A. V. Fomin, A. E. Nikolaev, I. P. Nikitina, A. S. Zubrilov, M. G. Mynbaeva, N. I. Kuznetsov, A. P. Kovarsky, B. Ja. Ber, and D. V. Tsvetkov, Phys. Stat. Sol. (a) **188**, 433 (2001).

[77]   I. Shai, C. E. M. de Oliviera, Y. Shapira, and J. Salzman, Phys. Rev. B **64**, 205313 (2001).

[78]   M. E. Levinshtein, S. L. Ramyantsev, and M. S. Shur, *Properties of Advanced Semiconductor Materials* (Wiley, New York, 2001), p. 31.

[79]   M. L. Nakarmi, K. H. Kim, M. Khizar, Z. Y. Fan, J. Y. Lin, and H. X. Jiang, Appl. Phys. Lett. **86,** 092108 (2005).

[80]   J. Li, K. B. Nam, M. L. Nakarmi, J. Y. Lin, and H. X. Jiang, Appl. Phys. Lett. **81**, 3365 (2002).

[81]   K. B. Nam, J. Li, M. L. Nakarmi, J. Y. Lin, and H. X. Jiang, Appl. Phys. Lett. **82**, 1694 (2003).

[82]   K. B. Nam, M. L. Nakarmi, J. Li, J. Y. Lin, and H. X. Jiang, Appl. Phys. Lett. **83,** 2787 (2003).

[83]   R. A. Mair, J. Li, S. K. Duan, J. Y. Lin, and H. X. Jiang, Appl. Phys. Lett. **74**, 513 (1999).

[84]   J. R. Haynes, Phys. Rev. Lett. **4,** 361 (1960).

[85]   E. I. Rashba and G. E. Gurgenishvili, Sov. Phys. Solid State **4**, 759 (1962).

[86]   M. L. Nakarmi, N. Nepal, C. Ugolini, T. M. Altahtamouni, J. Y. Lin, and H. X. Jiang, Appl. Phys. Lett. **89,** 152120 (2006).

[87]   M. Smith, G. D. Chen, J. Y. Lin, H. X. Jiang, M. A. Khan, C. J. Sun, Q. Chen, and J. W. Yang , J. Appl. Phys. **79**, 7001 (1996).

[88]   C. Klingshirn and H. Haug, Phys. Rep. **70**, 315 (1981).

[89]   H. X. Jiang, and J. Y. Lin, in *"III-Nitride Semiconductor: Optical Properties I*, edited by M. O. Manasreh and H. X. Jiang, (Taylor & Francis, London, 2002).

[90]   G. D. Chen, M. Smith, J. Y. Lin, H. X. Jiang, M. A. Khan, and C. J. Sun, Appl. Phys. Lett. **67**, 1653 (1995).

[91]   V. Adivarahan, S. Wu, J. P. Zhang, A. Chitnis, M. Shatalov, V. Mandavilli, R. Gaska, and M. Asif Khan. Appl. Phys. Lett. **84**, 4762 (2004).

[92]   S. Nakamura, N. Iwasa, M. Senoh, and T. Mukai, Jpn. J. Appl. Phys. **31**, 1258 (1992).

[93]   M. Monemar, H. P. Gislason, and O Lagerstedt, J. Appl. Phys **51**, 640 (1980).

[94]   P. Bergman, G. Ying, B. Monemar, and P.O. Holtz, J. Appl. Phys. **61**, 4589 (1987).

[95]   F. Mireles and S. E. Ulloa, Phys. Rev. B **58**, 3879 (1998).

[96]   N. Nepal, M. L. Nakarmi, K. B. Nam, J. Y. Lin, and H. X. Jiang, Appl. Phys. Lett. **85,** 2271 (2004).

[97]   M. L. Nakarmi, N. Nepal, C. Ugolini, T. M. Altahtamouni, J. Y. Lin, and H. X. Jiang, Appl. Phys. Lett., Appl. Phys. Lett. **89,** 152120 (2006).

[98]   T. L. Tansley and R. J. Egan, Phys. Rev. B **45**, 10942 (1992).

[99]   V. I. Litvinov and V. K. Dugaev, Phys. Rev. Lett. **86**, 5593 (2001).

[100]   R. M. Frazier, J. Stapleton, G. T. Thaler, C. R. Abernathy, S. J. Pearton, R. Rairigh, J. Kelly, A. F. Hebard, M. L. Nakarmi, K. B. Nam, J. Y. Lin, H. X. Jiang, J. M. Zavada, and R. G. Wilson, J. Appl. Phys. **94**, 1592 (2003).

[101]   D. C. Look, D. C. Reynolds, J. W. Hemsky, J. R. Sizelove, R. L. Jones, and R. J. Molnar, Phys. Rev. Lett. **79**, 2273 (1997).

[102]   J. Neugebauer and C. G. Van de Walle, Phys. Rev. B **50**, 8067 (1994).

[103]   Q. Yang, H. Feick, and E. R. Weber, Appl. Phys. Lett. **82**, 3002 (2003).

[104]   D. W. Jenkins and J. D. Dow, Phys. Rev. B **39**, 3317 (1989).

[105]   W. J. Moore, J. A. Freitas, Jr., S. K. Lee, S. S. Park, and J. Y. Han, Phys. Rev. B **65**, 081201 (2002).

[106]   S. O. Kucheyev, J. S. Williams, C. Jaegadish, G. Li, and S. J. Pearton, J. Appl. Phys. **76**, 3899 (2000).

[107]   T. Mattila and R. M. Nieminen, Phys. Rev. B **54**, 16676 (1996).

[108]   K. B. Nam, J. Li, K. H. Kim, J. Y. Lin, and H. X. Jiang, Appl. Phys. Lett. **78**, 3690 (2001).

[109]   M. Ilegems, R. Dingle, and R. A. Logan, J. Appl. Phys. **43**, 3797 (1972).

[110]   W. Shan, T. J. Schmidt, X. H. Yang, S. J. Hwang, J. J. Song, and B. Goldenberg, Appl. Phys. Lett. **66**, 985 (1995).

[111]   C. I. Harris, B. Monemar, H. Amano, and I. Akasaki, Appl. Phys. Lett. **67**, 840 (1995).

[112] M. Smith, G. D. Chen, J. Y. Lin, H. X. Jiang, M. A. Khan, C. J. Sun, Q. Chen, and J. W. Wang, J. Appl. Phys. **79**, 7001 (1996).

[113] D. C. Reynold, D. C. Look, W. Kim, O. Aktas, A. Botchkarev, A. Salvador, H. Morkoc, and D. N. Talwar, J. Appl. Phys. **80**, 594 (1996).

[114] A. K. Viswanath, J. I. Lee, S. Yu, D. Kim, Y. Choi, and C. H. Hong, J. Appl. Phys. **84**, 3848 (1998).

[115] M. Smith, J. Y. Lin, H. X. Jiang, and A. Khan, Appl. Phys. Lett. **71**, 635 (1997).

[116] K. C. Zeng, J. Y. Lin, H. X. Jiang, and W. Yang, Appl. Phys. Lett. <u>74</u>, 3821, (1999).

[117] E. G. Brazel, M. A. Chin, V. Narayanamurti, D. Kapolnek, E. J. Tarsa, and S. P. DenBaars, Appl. Phys. Lett. **70**, 330 (1997).

[118] S. Bloom, G. Harbeke, E. Meier, and I. B. Ortenburger, Phys. Status. Solidi **66**, 161 (1974).

[119] W. R. L. Lambrecht, B. Segall, J. Rife, W. R. Hunter, and D. K. Wickenden, Phys. Rev. B **51**, 13516 (1995).

[120] J. Kolnik, I. H. Oguzman, K. F. Brennan, R. Wang, P. P. Ruden, and Y. Wang, J. Appl. Phys. **78**, 1033 (1995).

[121] M. Wraback, H. Shen, J. C. Carrano, T. Li, J. C. Campbell, M. J. Schurman, and I. T. Ferguson, Appl. Phys. Lett. **76**, 1155 (2000).

[122] U. V. Bhapkar and M. S. Shur, J. Appl. Phys. **82**, 1649 (1997).

[123] R. Brazis and R. Raguotis, Appl. Phys. Lett. **85**, 609 (2004).

[124] C. Y. Yeh, S. H. Wei, and A. Zunger, Phys. Rev. B **50**, 2715 (1994).

[125] K. B. Nam, J. Li, M. L. Nakarmi, J. Y. Lin, and H. X. Jiang, Appl. Phys. Lett. **84,** 5264 (2004).

[126] W. B. Joyce, R. J. Bachrach, R. W. Dixon, and D. A. Sealer, J. Appl. Phys. **45**, 2229 (1974).

[127] I. Schnitzer, E. Yablonovitch, C. Caneau, T. J. Gmitter, and A. Scherer, Appl. Phys. Lett. **63**, 2174 (1993).

[128] R. Windisch, C. Rooman, S. Meinlschmidt, P. Kiesel, D. Zipperer, G. H. Döhler, B. Dutta, M. Kuijk, G. Borghs, and P. Heremans, Appl. Phys. Lett. **79**, 2315 (2001).

[129] T. Fujii, Y. Gao, R. Sharma, E. L. Hu, S. P. DenBaars, and S. Nakamura, Appl. Phys. Lett. **84**, 855 (2004).

[130] S. X. Jin, J. Li, J. Y. Lin, and H. X. Jiang, Appl. Phys. Lett. **77,** 3236 (2000).

[131] E. Yablonovitch, Phys. Rev. Lett. **58**, 2059 (1987).

[132] M. Boroditsky, R. Vrijen, T. F. Krauss, R. Coccioli, R. Bhat, and E. Yablonovitch, J. Lightwave Technol. **17**, 2096 (1999).

[133] H. Y. Ryu, Y. H. Lee, R. L. Sellin, and D. Bimberg, Appl. Phys. Lett. **79**, 3573 (2001).

[134] A. A. Erchak, D. J. Ripin, S. Fan, P. Rakich, J. D. Joannopoulos, E. P. Ippen, G. S. Petrich, and L. A. Kolodziejski, Appl. Phys. Lett. **78,** 563 (2001).

[135] T. N. Oder, J. Shakya, J. Y. Lin, and H. X. Jiang, Appl. Phys. Lett. **83,** 1231 (2003).

[136] T. N. Oder, K. H. Kim, J. Y. Lin, and H. X. Jiang, Appl. Phys. Lett. **84,** 466 (2004).

[137] J. J. Wierer, M. R. Krames, J. E. Epler, N. F. Gardner, M. G. Craford, J. R. Wendt, J. A. Simmons, and M. M. Sigalas, Appl. Phys. Lett. **84**, 3885 (2004).

[138] J. Shakya, K. H. Kim, J. Y. Lin, and H. X. Jiang, Appl. Phys. Lett. **85,** 142 (2004).

[139] J. Shakya, J. Y. Lin and H. X. Jiang**,** Appl. Phys. Lett. **85**, 2104 (2004).

[140] L. Chen and A. V. Nurmikko, Appl. Phys. Lett. **85**, 3663 (2004).

[141] A. David, C. Meier, R. Sharma, F. S. Diana, S. P. DenBaars, E. Hu, S. Nakamura, C. Weisbuch, and H. Benisty, Appl. Phys. Lett. **87**, 101107 (2005).

[142] D. H. Kim, C. O. Cho, Y. G. Roh, H. Jeon, Y. S. Park, J. Cho, J. S. Im, C. Sone, Y. Park, W. J. Choi and Q. H. Park, Appl. Phys. Lett. **87**, 203508 (2005).

[143] M. Khizar, Z. Y. Fan, K. H. Kim, J. Y. Lin, and H. X. Jiang, Appl. Phys. Lett. **86**, 173504 (2005)

[144] M. Bickermann, B. M. Epelbaum, P. Heimann, Z. G. Herro, and A. Winnacker, Appl. Phys. Lett. **86,** 131904 (2005).

[145] Michel Dudley (Private Communication).

[146] V. N. Astratov, I. S. Culashaw, R. M. Stevenson, D. M. Whittaker, M. S. Skolnick, T. F. Krauss, and R. M. De La Rue, J. Lightwave Technol. **17**, 2050 (1999).

[147]   A. Barra, D. Cassagne, and C. Jouanin, Appl. Phys. Lett. **72**, 627 (1998).

Appendix A Research Work Publications

1. **N. Nepal**, J. Shakya, J. Y. Lin, H. X. Jiang, Z. M. Zavada, and P. Hertog, "Er-doped AlGaN/GaN:Er/AlGaN double heterostructure photonic crystals," [submitted to Appl. Phys. Lett.].

2. M. L. Nakarmi, **N. Nepal**, J. Y. Lin, and H. X. Jiang, "Photoluminescence studies of impurity transitions involving nitrogen vacancies in Mg-doped AlGaN alloys," [submitted to Appl. Phys. Lett.].

3. **N. Nepal**, M. L. Nakarmi, H. U. Jang, J. Y. Lin, and H. X. Jiang," Growth and photoluminescence studies of Zn-doped AlN epilayers," Appl. Phys. Lett. **89**, 192111 (2006).

4. M. L. Nakarmi, **N. Nepal**, C. Ungolini, T. M. Altahtamouni, J. Y. Lin, and H. X. Jiang, "Correlation between electrical and optical properties of Mg doped AlN epilayers," Appl. Phys. Lett. **89**, 152120 (2006).

5. Z. M. Zavada, **N.Nepal**, J. Y. Lin, H. X. Jiang, E. Brown, U. Hommerich, J. Hite, G. T. Thaler, C. R. Abernathy, S. J. Pearton,and R. Gwilliam, "Ultraviolet photoluminescence from Gd-implanted AlN epilayers," Appl. Phys. Lett. **89**, 152107 (2006).

6. C. Ungolini, **N. Nepal,** J. Y. Lin, H. X. Jiang and J. M. Zavada, "Erbium-doped GaN epilayers synthesized by metal-organic chemical vapor deposition," Appl. Phys. Lett. **89**, 151903 (2006).

7. T. M. Altahtamouni, **N. Nepal**, J. Li, M. L. Nakarmi, J. Y. Lin, and H. X. Jiang, "Growth and photoluminescence studies of Al-rich AlN/Al$_x$Ga$_{1-x}$N quantum wells," Appl. Phys. Lett. **89**, 131922 (2006).

8. **N. Nepal**, M. L. Nakarmi, J. Y. Lin, and H. X. Jiang, "Photoluminescence studies of impurity transitions in AlGaN alloys," Appl. Phys. Lett. **89**, 092107 (2006).

9. **N. Nepal**, K. B. Nam, J. Li, M. L. Nakarmi, J. Y. Lin, and H. X. Jiang, "Higher lying conduction band in GaN and AlN probed by photoluminescence spectroscopy," Appl. Phys. Lett. **88**, 261919 (2006).

10. **N. Nepal**, J. Shakya, M. L. Nakarmi, J. Y. Lin, and H. X. Jiang, "Deep ultraviolet photoluminescence studies of AlN photonic crystals," Appl. Phys. Lett. **88**, 133113 (2006).

11. **N. Nepal**, M. L. Nakarmi, J. Y. Lin, and H. X. Jiang, **"**Time-resolved photoluminescence studies of Mg-doped AlN epilayers," Proc. SPIE, 6118, 61180E (2006).

12. **N. Nepal**, J. Li, M. L. Nakarmi, J. Y. Lin, and H. X. Jiang, "Exciton localization in AlGaN Alloys," Appl. Phys. Lett. **88**, 062103 (2006).

13. **N. Nepal**, J. Li, M. L. Nakarmi, J. Y. Lin, and H. X. Jiang, "Temperature and Compositional Dependence of the Energy Bandgap of AlGaN Alloys," Appl. Phys. Lett. **87,** 242104 (2005).

14. M. L. Nakarmi, **N. Nepal**, J. Y. Lin, and H. X. Jiang, "Unintentionally doped n-type $Al_{0.67}Ga_{0.33}N$ epilayers," Appl. Phys. Lett. **86**, 261902 (2005).

15. **N. Nepal**, K. B. Nam, J. Li, J. Y. Lin, and H. X. Jiang," Carrier dynamics in AlN and GaN epilayers at elevated temperatures," SPIE Proceedings, **5725**, 119 (2005).

16. Ei Ei Nyein, U. Hommerich, J. M. Zavada, D. S. Lee, A. J. Steckl, **N. Nepal,** J. Y. Lin, and H. X. Jiang, " Ultravoilet and blue emission properties of Tm doped AlGaN and AlN," Conference on Lasers and Electro-Optics **1,** 2 (2004).

17. **N. Nepal**, M. L. Nakarmi, K. B. Nam, J. Y. Lin, and H. X. Jiang, "Acceptor-bound exciton transition in Mg-doped AlN epilayer," Appl. Phys. Lett. **85**, 2271 (2004).

18. **N. Nepal**, K. B. Nam, M. L. Nakarmi, J. Y. Lin, and H. X. Jiang, J. M. Zavada, and R.G. Wilson, "Optical properties of the nitrogen vacancy in AlN epilayers," Appl. Phys. Lett. **84**, 1090 (2004).

19. J. M. Zavada, S. X. Jin, **N. Nepal**, J. Y. Lin, H. X. Jiang, P. Chow and B. Hertog, "Electroluminescent properties of erbium-doped III-N light emitting diodes," Appl. Phys. Lett. **84**, 1061 (2004).